Surface Evolution on Basaltic Bodies: Tectonic, Geomorphic, and Diagenetic Modification on Io and Mars

Thesis by

Christina H. Seeger

In Partial Fulfillment of the Requirements for

the Degree of

Doctor of Philosophy

CALIFORNIA INSTITUTE OF TECHNOLOGY

Pasadena, California

2025

Defended May 28, 2025

For my family. You said, "Reach for the stars" but I think Mars and Io are pretty close.

Christina H. Seeger
ORCID: 0000-0003-4993-9724

ACKNOWLEDGEMENTS

A thesis is the product of so much more than the pages presented in this work, and I am beyond indebted to everyone in my scientific and personal orbits that contributed to the completion of this work. My two advisors, John Grotzinger and Katherine de Kleer, were an exceptional yin and yang pair to guide me through three very different projects, and I am so grateful for their encouragement to follow my interests with independence while providing enough guidance to ensure I continued to become a better scientist. When I joined the Curiosity rover team in 2016 as John's lab tech, I never expected I would later fold years of mission work into a Ph.D.; thank you, John, for recognizing a spark in me and fanning it for nearly a decade. Being a part of the MSL team has been one of the greatest joys of my career, and I am so grateful to the scientists and engineers whom I have had the honor to work with; I have grown so much through teamwork on ops and scientific discussions with all of you, and I am humbled to be part of such a magnificent team. In the outer Solar System, I would also like to thank my Io collaboration group; you have been such supportive mentors and colleagues and exploring the Junocam data with you as it was released was a huge highlight. I am so grateful Katherine connected us when she realized she had let a geologist into her group; I have learned so much from her about creativity in building a research program, and am so lucky to have had such a strong role model.

Caltech is made a special place by the people, and I am so grateful to the GPS division for the friendship and support I have received along the way. Many thanks to my thesis committee, Mike Lamb and Bethany Ehlmann, for the gentle guidance and fruitful conversations. Jen Shechet, Mark Garcia, Julie Lee, and Claire Fredrickson—you keep this division running and always made sure I had the equipment, candy, and laughs I needed to get through my days. Thanks to the Grotz Group in all its iterations for always being up for happy hour and celebrating my Martian victories from Earth, and especially to Claire Mondro for all of the conversations that improved my paper and myself as a scientist. Thanks also to the de Kleer group for your friendship and tolerance of my rose diagrams for four years. Though he went to MIT, I'd also like to extend a special thanks to Ashwin Narayan for his constant encouragement, curiosity, and willingness to step outside his field; this thesis would

not have been possible without his late-night math and coding support. The number of people who shaped my time in GPS, from the office to the field, is too large to list, but a special thanks to Ted, Freya, Eran, Noam, Josh, Iva, Elizabeth, Simon, Maria[2], Yu Yu, and Emily for all of the laughs and support.

To all my roommates on Catalina Ave—Jackie Dowling, Eric Ewing, Madison Douglas (and David Millard), Amanda Bednarick, and Korbi Thalhammer—thanks for the endless support, grillin' and chillin', and for making Pasadena home. To my Bellingham roommates during my remote G1 year—Meg Wyllie, Mindy Zuckerman, Steven Sobzak, Nox, and Lumos—thank you for carrying me through my delirious days on Mars Time. Thank you also to Olivia Gomez and MeiLu McDermott, whose presence in LA made returning here infinitely more tolerable. I would not have survived the last five years if not for the many adventures outside; thank you to Abby Keebler, Richard Horak, Noel Csomay-Shanklin, and Jocelyn Reahl for exploring and appreciating this incredible state with me. A part of my heart will always live with the National Park Service, and I am so grateful to my partner, Ben Garcia, for providing me with homes in Mount Rainier, Death Valley, Denali, and Lassen to escape to throughout my Ph.D. Backpacking, skiing, canyoneering, and stargazing with you across the western U.S. has kept me sane, and I could not have completed this work without the love, support, and balance you bring to my life.

My family has given me a lifetime of support and opportunity, and I would not be here if not for them. Thank you to my extended family, who have always been eager to hear about what I have been learning about. My Ph.D. was bookended by the losses of my grandfather, John Seeger, in my first year and my grandmother, Irene Meier, in my last year, but carrying their endless support in my heart has been a huge source of encouragement throughout this work. Finally, thank you to my parents for all of the sacrifices you made to give me the experiences that have helped shape me into the scientist I am today. You inspire me to be the best version of myself, and buoyed me up when I felt adrift. I know the geology in these chapters is a little different from the "interesting rocks" you used to show me as a kid, but I assure you it's just as cool.

ABSTRACT

All planets and moons in the Solar System evolve over geologic timescales, though the processes affecting each body vary widely depending on gravity, atmosphere thickness and composition, volcanic activity, and perhaps most importantly, the presence of a hydrologic cycle. This dissertation investigates the surface evolution of two basaltic bodies in our Solar System: one that has barely changed in 3.5 billion years, and one that changes almost daily. Jupiter's moon Io is continually resurfaced by large-scale volcanic eruptions of low-viscosity lava and sulfur dioxide gas, driven by interior heating generated by diurnal tidal stresses. Such tidal stresses have been linked to eruptive activity and tectonic ridge formation on other moons like Titan and Europa; while they strongly influence Io, they are orders of magnitude weaker than the crustal subsidence stresses which control the expression of tectonic features on the surface (kilometers-tall mountains and caldera-like volcanic features called paterae). Chapter 2 investigates whether tidal stresses may have any influence on the formation of mountains and paterae. Though no global trends have been identified, I suggest that local correlations between patera orientations and the large volcanic center of Loki Patera may provide insight into the magma plumbing pathways of this unique volcano. As soon as tectonic mountains are uplifted on Io, they are subject to gravity- and seismicity-driven erosional processes tearing them down. In Chapter 3, I present the first regional geologic map of a trio of mountains named Cocytus Montes and identify a new geologic unit—a blocky deposit composed of kilometer-scale slab-shaped blocks of crust—that are visible thanks to the favorable resolution and near-terminator lighting conditions of new *Junocam* imagery. I explore several new erosional mechanisms for Io that could create these blocks, determining regolith creep-modified cliff collapse to be the most likely. The orders of magnitude higher resolution imagery collected by the Mars Science Laboratory Curiosity rover provides a backdrop for much closer analysis of how sediments moved, deposited, lithified, and were subsequently modified by diagenetic fluids on ancient Mars. Chapter 4 takes advantage of hand-sample scale data to categorize a diverse array of diagenetic fabrics (nodules, pits, color variations) that correlate with the stratigraphy in a region defined by a transition from clay-bearing rocks to sulfate-bearing rocks. I present several hypotheses to explain how the Mg sulfate detected in these nodules and pore-filling cements may have

precipitated at depth, to complement current evaporite-driven models. These hypotheses could be tested in the coming years of Mars exploration by the rover, and will provide insights into the longevity of a groundwater system after surface water ceased to flow on ancient Mars. Overall, this work explores the well-studied terrestrial processes of surface modification, degradation, and diagenesis under distinctly alien conditions throughout the Solar System.

PUBLISHED CONTENT AND CONTRIBUTIONS

Chapter 4 is published in:

Seeger, C. H., & Grotzinger, J. P. (2024). Diagenesis of the Clay-Sulfate Stratigraphic Transition, Mount Sharp Group, Gale Crater, Mars. *Journal of Geophysical Research: Planets*, *129*(12), e2024JE008531. https://doi.org/10.1029/2024JE008531

C.H.S. and J.P.G. conceived this study ; C.H.S. compiled the data, performed the analysis, and wrote the manuscript with help from J.P.G.

TABLE OF CONTENTS

C h a p t e r 1

INTRODUCTION

"Give me Vesuvius' crater for an inkstand! Friends, hold my arms! For in the mere act of penning my thoughts of this [dissertation], they weary me, and make me faint with their outreaching comprehensiveness of sweep, as if to include the whole circle of the sciences, and all the generations of [tidal models], and [orbiters], and [rovers], past, present, and to come, with all the revolving panoramas of empire on [Io and Mars], and throughout the whole universe, not excluding its suburbs."

Moby Dick, Chapter 104: The Fossil Whale

1.1 Our evolving understanding of the Solar System

Humans have long been fascinated by the heavens. Without today's light pollution blocking the fainter objects in the night sky, our ancestors marveled, charted, and sometimes feared the depths of the starfield above. Consistent observations of the sky will quickly reveal to the observer several points of light that do not conform to the motion of the stars: the planets, wanderers across the sky. While Venus, Jupiter, and Saturn can outshine it, the distinctive red hue of Mars makes it easily stand out in the sky.

Our ancestors did not look up at this bright, red object transiting the night sky and wonder if it was a basaltic world with many minerals in common with Earth (e.g., Bibring et al., 2005; Ehlmann and Edwards, 2014; Hazen et al., 2008); if it once had a rich hydrologic cycle, with rivers, lakes, and glaciers (e.g., Baker et al., 1991); if those waters could once have hosted life, in a familiar or alien form (Grotzinger et al., 2014). They did not consider how the smaller diameter led to faster interior cooling than on their home, locking the inner core and outer core together, ceasing magnetic field generation, and subsequently losing the surface water to space or subsurface freezing (Jakosky, 2021). They did not ask how long it took for Mars to dry up.

Instead, they charted the movements of Mars and asked, "how does this relate to *me*?" The Mayan Dresden Codex, one of the oldest surviving books from the Americas (dating to the 11th or 12th century), records not the 687-day Mars year, but rather the 780 day synodic cycle for how Mars appears in the sky to the observers (Bricker et al., 2001; Wilson, 1924). Ancient cultures from China to Australia were fascinated by how planets interacted with each other in the night sky, and the cultural implications of tracking these bodies were far-reaching.

When Galileo trained his telescope on Jupiter January 8, 1610, he recorded the motion of Jupiter's four largest moons (Galilei, 1610). He was not looking at these quickly moving points of light in his 20-power telescope and wondering if any of them might harbor an ice shell over a subsurface ocean that could potentially host life (Reynolds et al., 1983). He did not ponder the volcanic output of the innermost "star," and consider if the particles output by its massive plumes could deliver sulfur to the trailing hemisphere of its ocean-world neighbor (e.g., Becker et al., 2022; Eviatar et al., 1981). Rather, he again asked the age-old question, "how does this relate to *me*?" This time, that question became extremely consequential in progressing our understanding of Solar System dynamics, providing some of the first solid evidence for the Copernican Heliocentric model, with huge repercussions for human self-importance as our egos no longer seemed to keep the heavens dancing in a slow-bound circle around the Earth (Copernicus, 1543).

Though our questions about these bodies have evolved through the centuries, they still retain that fundamental connection to *us*. We explore outwards to understand inwards, and the more we see of the Solar System, the more we want to know. The last 50 years have seen a golden age of space exploration, and our understanding of both Mars and Jupiter's innermost moon Io have evolved tremendously. The 1970s saw the first detailed pictures of the dusty, red, topographically varied Mars with the *Mariner* and *Viking* missions (Arvidson et al, 1989; Masursky, 1973; Soffen, 1976). They also gave us a detailed portrait of the outer solar system, with *Voyager* capturing Io mid-eruption (Strom, 1981). The late nineties and early aughts ushered in a new era: the Mars Exploration Rovers (Spirit and Opportunity) examined sedimentary rocks, reshaped by wind and ancient water (Squyres et al., 2004a; 2004b;

2004c); the launch of the Mars Global Surveyor satellite marked the beginning of continual orbital observations of Mars (e.g., Albee et al., 2001); and the *Galileo* mission captured Io's surface in unprecedented detail, complementing the *Voyager* coverage and providing thermal measurements that have informed a long debate about how Io's magma reaches the surface (Lopes et al., 2007). Today, the Mars Science Laboratory (MSL) Curiosity rover and Mars 2020 Perseverance rover collect new observations daily that shift our understanding of the ancient climatic system on Mars (e.g., Grotzinger et al., 2014; 2015; Mangold et al., 2021), while the *Juno* spacecraft has imaged Io on several flybys, capturing the topography of the north pole for the first time and advancing our understanding of Io's thermal output (Davies et al., 2024; Perry et al., 2025; Seeger et al., 2025).

1.2 Mars and Io as geologic endmembers

Our current understanding of Mars and Io, informed by the aforementioned decades of observation, reflects two end members in geologic activity: one surface that has barely changed over the last 3.5 billion years (Mars), and one that changes daily (Io). Mars therefore contains an Earth-like rock record of deep time that has largely been erased on Earth due to plate tectonics, allowing us to peer back into a time of early Earth and Mars history. Io, on the other hand, is a dynamic and active body dominated by volcanism and tides—much like what Earth was like in the Hadean Eon. Volcanic activity is so prevalent on Io that impact craters are erased rapidly by new flows, leaving us with no record of them. Th extremely fresh surface is a foil to the ancient Martian one, though both offer a picture of the early Earth in their own way.

Earth, then, sits as an intermediate between these two endmember worlds. They provide the perfect backdrop to observe common terrestrial processes—like uplift, erosion, and alteration—but under wildly different gravity, atmospheric pressure, and temperature conditions. Therefore, we can once again look outward to understand ourselves, as our ancestors did. This work capitalizes on the active mission exploration of Mars by the Curiosity rover and Io by the *Juno* spacecraft to do just that.

1.3 Overview of Dissertation Chapters

1.3.1 Push and Pull

Chapter 2 of this work takes the most zoomed out view, examining Io as a complete body. Laplace orbital resonance between Io, Europa, and Ganymede (the innermost Galilean Satellites) pulls Io into an elliptical orbit, where the large but variable gravitational pull on the moon by Jupiter deforms it significantly, creating a tide up to 330 meters in the rocky body (as opposed to Earth's 1-meter tidal bulge in the open sea, or the 18-meter maximum tidal range recorded in the Bay of Fundy, Canada) (Figure 1). The tidal flexing heats the interior, resulting in near-constant volcanic eruptions on the surface in the form of long, thin lava flows and plumes of sulfur-dioxide rich gases that can stretch hundreds of meters above the surface. These eruptions leave behind (and sometime emanate from) depressed caldera-like features called paterae, of which there are over 400 on Io (Radebaugh et al., 2001). The gases blanket the surface in layers of sulfur-dioxide rich frost (with the variations in composition and alteration contributing to the colorful palette on Io's surface) (Carlson et al., 1997; Hapke, 1989; Geissler et la., 1999; Pearl et al., 1979; Spencer et al., 2000). Interlayered crust of basaltic to ultramafic lava flows and thin sulfur-rich deposits create a layered crust under compressional stress at depth due to subsidence, which is accommodated by the faulting that is hypothesized to uplift Io's impressive mountains, isolated tectonic blocks towering an average of 6 km above the surrounding plains but reaching heights of 16 km—nearly twice that of Mount Everest, on a body approximately the size of Earth's moon (McEwen et al., 2004; McKinnon et al., 2001; Schenk & Bulmer 1998; Schenk et al., 2001; Turtle et al., 2001). Paterae may form from magma exploiting the faulted subsurface to pool on the surface, or from hot-spot type volcanism exploiting crustal weaknesses to rise from the mantle or intermediate magma chambers (Davies et al., 2006; Jaeger et al., 2003; Keszthelyi et al., 2004; 2007; Kirchoff & McKinnon, 2009; McKinnon et al., 2001; O'Reilly & Davies, 1981; Spencer et al., 2020).

While the tidal stresses acting on Io contribute to deformation on a global scale, Bart et al. (2004) suggest the manifestation of these stresses on the surface may modify or create

kilometer-scale wrinkled ridge textures visible in the highest resolution Galileo imagery, because the orientations of these features on the surface are orthogonal to the direction of maximum stress they experience during each orbit. Chapter 2 investigates whether tidal stresses could act on features of a much larger scale, influencing the formation of paterae or mountains on the surface; extensional stresses could contribute to paterae opening via rifting orthogonal to maximum stress, and/or compressional stresses could bias mountain uplift to occur orthogonal to maximum stress. The correlations between these surface features are an important component in understanding tidal controls on the eruptive episodes that have been observed to have some periodicity from Earth-based monitoring (de Kleer et al., 2019).

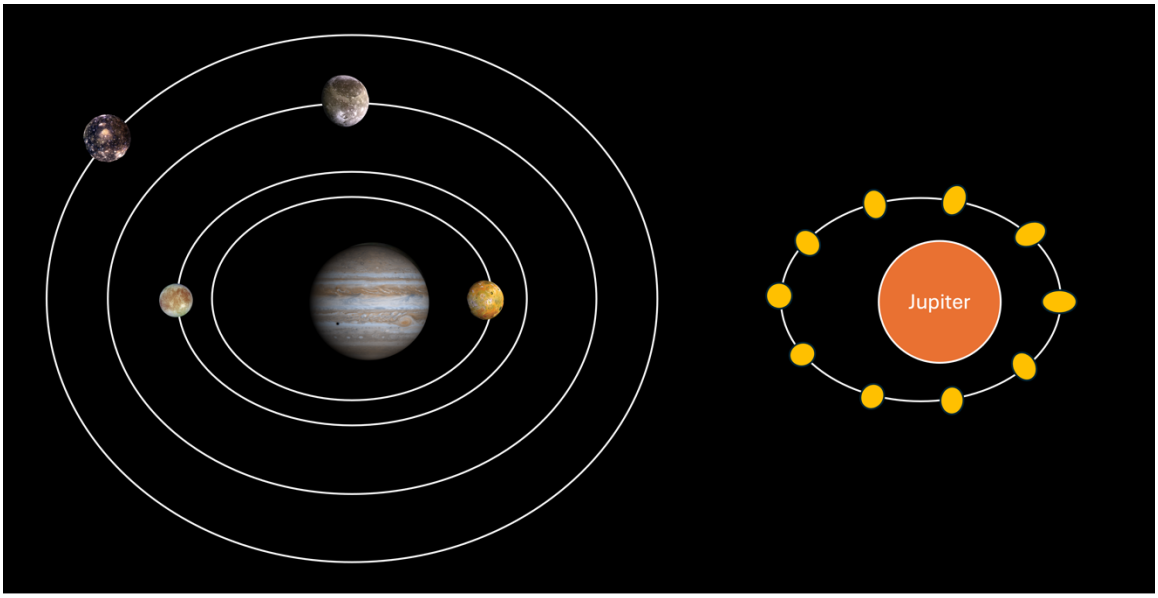

Figure 1. Schematic illustration of Galilean satellite orbital resonance (Io, Europa, Ganymede, and Callisto in increasing distance from Jupiter) creating (exaggerated) elliptical orbits (left) and resulting tidal deformation in Io (right).

1.3.2 Mountains Rise and Mountains Fall

The mountains on Io are dramatic, but require favorable sunset-like lighting conditions to easily discern them. Fortunately, the *Juno* spacecraft high-resolution imagery of Io's north polar region, collected by the *Junocam* instrument, delivered just that. For the first time, imagery has been obtained of a trio of mountains near the north pole, named Cocytus Montes after the three stone giant sentinels encountered by Dante and Virgil as they arrived at the frozen Cocytus, the river of wailing, in the ninth circle of the underworld (Alighieri, 1321/1982). These >5km tall massifs rise above the surrounding plains, with two edifices connected by a one- to three-kilometer high plateau. In Chapter 3, I present the first regional geologic map based on this new imagery and identify updates to the USGS global geologic map of Io (Williams et al., 2011). Previous work on the degradation of mountain structures and patera walls suggests that the main mechanisms for erosion are slumping, mass wasting, and sapping (Moore et al., 2001; Schenk & Bulmer, 1998). Through the new geologic map, I have identified a unique deposit of kilometer-scale, slab-shaped blocks of crust, dominantly distributed across the inter-mountain plateau, and consider the potential mechanisms for their formation and subsequent modification that are based more on terrestrial hillslope processes and regolith generation than has previously been considered for Io. As we get better and better data back from this distant, volcanic moon, we will sharpen our understanding of the large-scale features and their formation, but also will evolve our understanding of how these edifices break down in the absence of a water cycle, and what the near-surface cycling of material may look like on active airless bodies.

1.3.3 Top down or bottom up?

Chapter 4 shifts us to the inner Solar System and allows us to zoom from the orbital perspective on Mars all the way down to the cements filling pore spaces in the sedimentary rocks. While "good" resolutions for Io imagery are on the order of 1 km per pixel, the rovers on the surface of Mars can capture ~150 μm/pixel imagery of the "workspace"—the rocks

directly in front of the rover, accessible by the instruments on the rover's outstretched arm—and surrounding terrain, much more the cell phone photos we take of the rocks beneath our feet and surrounding landscapes while on a hike (Bell et al., 2017; Malin et al., 2017). The Curiosity rover has spent the last ~13 years driving across Gale crater, an impact crater situated at the precise point where Mars' southern highlands meet the northern lowlands in a global topographic crustal dichotomy (e.g., Watters et al., 2007). The rover has traversed ~34 km to date, climbing ~850 meters in elevation as it ascends the layered sedimentary mound, Aeolis Mons (or, informally, Mount Sharp), at the center of Gale crater. Each sol, or Martian day, of this journey is thoroughly documented with images, measurements of elemental abundances, occasional drill core analysis, and, when possible, the closest possible look at the rocks acquired by the Mars Hand Lens Imager (MAHLI) instrument, which can provide an average resolution of 100 microns/pixel for high standoff (25 cm above the rock surface) and 30 microns/ pixel for closer standoff (<5cm above the rock surface) (Edgett et al., 2012).

The suite of observations collected throughout the mission has transformed our understanding of Mars as sedimentary basaltic world with large-scale wind-blown sandstones and a robust groundwater system precipitating hematite spherules that was established through the groundbreaking work of the MER missions (e.g., Calvin et al., 2008; Grotzinger et al., 2005; McLennan et al., 2005). The sediments at Gale crater contain a fluvio-lacustrine deposits originating from the crater rim and flowing into a basin filling with a thick sequence of lacustrine mudstones, demonstrating that longstanding water bodies with neutral pH persisted for a minimum duration of hundreds to tens of thousands of years on early Mars, contributing to the prior OMEGA and CRISM orbital discoveries that Mars was once a habitable world (e.g., Grotzinger et al., 2014; 2015).

About 3.5 billion years ago, Mars experienced a climatic shift; after the core became coupled to the mantle and the magnetic dynamo shut off, atmospheric particles (and surface water) were more easily stripped away by solar wind and lost to space (e.g., Jakosky, 2021); more impactful, however, was the locking up of water in hydrated minerals in the crust, fated to

remain sequestered away from the surface in the absence of plate tectonics-driven recycling (Scheller et al,. 2021). The timing and nature of this environmental transition is poorly constrained, but has major implications for how long Mars could have sustained life, and may even offer insight into the fluctuating conditions we are experiencing on Earth's surface.

Mount Sharp, stretching ~5km above the crater floor, provides a record of the later phases of this transition, with the story written in the sedimentary rock record. Part way up its slopes, there is a distinct transition from clay-bearing strata deposited during the wet years to overlying sulfate-bearing strata, deposited in what was determined from orbit to be the succeeding dry years (Malin and Edgett, 2000; Milliken et al., 2010; Sheppard et al., 2021; Thomson et al., 2011). Observations made on the ground over the ~2 year period where the rover traversed through this clay-sulfate transition region became the basis for Chapter 4. Image and chemical analysis of the sedimentary sequence in this region quickly revealed that diagenetic fabrics, created by groundwater alterations of the rocks after lithification, greatly contributed to—and confounded—the story of Gale crater transitioning from a wet to dry depositional environment. The persistence of diagenetic fabrics like nodules, color variations, and veins disrupting the primary stratigraphy serve as an indicator that groundwater persisted long after the region became dominated by aeolian sandstones—and the appearance of rippled inter-dune lake deposits corroborates this persistent groundwater table (e.g., Caravaca et al., 2025; Gupta et al., 2023; Mondro et al., 2025). The increase in abundance of extremely soluble Mg-sulfate in the rock record moving upsection from the clay-bearing rocks is the clearest indication of aridification throughout this region. However, the formation mechanisms to emplace this Mg-sulfate are debated, and have lasting implications for the persistence of groundwater on Mars as it endured its aridification. Though there is evidence for localized periodic desiccation (Rapin et al., 2023), there is no record of evaporitic or near-surface crusts forming in the widespread, regional sedimentological record. How, then, did these Mg sulfates, which appear to be concentrated in nodules and pore-filling cements, form? Chapter 4 poses three alternative hypotheses for pathways in which groundwater may have remobilized pre-existing sulfates in higher or deeper stratigraphic units and reprecipitated them at depth within pore spaces. The top-down

and bottom-up models presented here have implications for how long the groundwater table may have persisted once surface water ceased to flow on Mars, and provides a tidy framework to test over the coming years of rover exploration of an enigmatic web of boxwork-type raised ridges, potentially created by fracture fill (e.g., Siebach & Grotzinger, 2014).

References

Albee, A. L., Arvidson, R. E., Palluconi, F., & Thorpe, T. (2001). Overview of the Mars Global Surveyor mission. *Journal of Geophysical Research: Planets*, *106*(E10), 23291-23316. https://doi.org/10.1029/2000JE001306

Alighieri, D. (1982). *Inferno* (A. Mandelbaum Trans). Bantam Classics. (Original work published 1321)

Arvidson, R. E., Gooding, J. L., & Moore, H. J. (1989). The Martian surface as imaged, sampled, and analyzed by the Viking landers. *Reviews of Geophysics*, *27*(1), 39-60. https://doi.org/10.1029/RG027i001p00039

Baker, V. R., Strom, R. G., Gulick, V. C., Kargel, J. S., Komatsu, G., & Kale, V. S. (1991). Ancient oceans, ice sheets and the hydrological cycle on Mars. *Nature*, *352*(6336), 589-594. https://doi.org/10.1038/352589a0

Bart, G. D., Turtle, E. P., Jaeger, W. L., Keszthelyi, L. P., & Greenberg, R. (2004). Ridges and tidal stress on Io. *Icarus*, *169*(1), 111-126. https://doi.org/10.1016/j.icarus.2004.01.003

Becker, T. M., Trumbo, S. K., Molyneux, P. M., Retherford, K. D., Hendrix, A. R., Roth, L., ... & McGrath, M. A. (2022). Mid-ultraviolet Hubble observations of Europa and the global surface distribution of SO2. *The Planetary Science Journal*, *3*(6), 129. DOI: 10.3847/PSJ/ac69eb

Bell III, J. F., Godber, A., McNair, S., Caplinger, M. A., Maki, J. N., Lemmon, M. T., et al. (2017). The Mars Science Laboratory Curiosity rover Mastcam instruments: Preflight and in-flight calibration, validation, and data archiving. *Earth and Space Science*, *4*(7), 396–452. https://doi.org/10.1002/2016EA000219

Bibring, J. P., Langevin, Y., Gendrin, A., Gondet, B., Poulet, F., Berthé, M., ... & Omega Team. (2005). Mars surface diversity as revealed by the OMEGA/Mars Express observations. *Science*, *307*(5715), 1576-1581. DOI: 10.1126/science.1108806

Bricker, H. M., Aveni, A. F., & Bricker, V. R. (2001). Ancient Maya documents concerning the movements of Mars. *Proceedings of the National Academy of Sciences*, *98*(4), 2107-2110. https://doi.org/10.1073/pnas.98.4.2107

Calvin, W. M., Shoffner, J. D., Johnson, J. R., Knoll, A. H., Pocock, J. M., Squyres, S. W., ... & Thompson, S. D. (2008). Hematite spherules at Meridiani: Results from MI, Mini-TES, and Pancam. *Journal of Geophysical Research: Planets*, *113*(E12). https://doi.org/10.1029/2007JE003048

Caravaca, G., Gupta, S., Rapin, W., Schieber, J., Le Deit, L., Mangold, N., ... & Vasavada, A. R. (2025, March). Prow & co.: inside the fluvial lenses of Gale's layered sulfate unit. In *56th Lunar and Planetary Science Conference* (p. 1389).

Carlson, R. W., Smythe, W. D., Lopes-Gautier, R. M. C., Davies, A. G., Kamp, L. W., Mosher, J. A., ... & Fanale, F. P. (1997). The distribution of sulfur dioxide and other infrared absorbers on the surface of Io. *Geophysical Research Letters*, *24*(20), 2479-2482. https://doi.org/10.1029/97GL02609

Copernicus, N. (1543). De revolutionibus orbium coelestium (On the Revolutions of the Heavenly Spheres).

Davies, A. G., Perry, J. E., Williams, D. A., & Nelson, D. M. (2024). Io's polar volcanic thermal emission indicative of magma ocean and shallow tidal heating models. *Nature Astronomy*, *8*(1), 94-100. https://doi.org/10.1038/s41550-023-02123-5

Davies, A. G., Wilson, L., Matson, D., Leone, G., Keszthelyi, L., & Jaeger, W. (2006). The heartbeat of the volcano: The discovery of episodic activity at Prometheus on Io. *Icarus*, *184*(2), 460-477. doi:10.1016/j.icarus.2006.05.012

de Kleer, K., Nimmo, F., & Kite, E. (2019). Variability in Io's volcanism on timescales of periodic orbital changes. *Geophysical Research Letters*, *46*(12), 6327-6332. https://doi.org/10.1029/2019GL082691

Edgett, K. S., Yingst, R. A., Ravine, M. A., Caplinger, M. A., Maki, J. N., Ghaemi, F. T., et al. (2012). Curiosity's Mars hand lens imager (MAHLI) investigation. *Space Science Reviews*, *170*(1–4), 259–317. https://doi.org/10.1007/s11214-012-9910-4

Ehlmann, B. L., & Edwards, C. S. (2014). Mineralogy of the Martian surface. *Annual Review of Earth and Planetary Sciences*, *42*(1), 291-315. https://doi.org/10.1146/annurev-earth-060313-055024

Eviatar, A., Siscoe, G. L., Johnson, T. V., & Matson, D. L. (1981). Effects of Io ejecta on Europa. *Icarus*, *47*(1), 75-83. https://doi.org/10.1016/0019-1035(81)90092-0

Galilei, Galileo. (1610). Sidereus nuncius. Apud Thomam Baglionum. https://doi.org/10.5479/sil.95438.39088015628597

Geissler, P. E., McEwen, A. S., Keszthelyi, L., Lopes-Gautier, R., Granahan, J., & Simonelli, D. P. (1999). Global color variations on Io. *Icarus*, *140*(2), 265-282. https://doi.org/10.1006/icar.1999.6128

Grotzinger, J. P., Arvidson, R. E., Bell Iii, J. F., Calvin, W., Clark, B. C., Fike, D. A., ... & Watters, W. A. (2005). Stratigraphy and sedimentology of a dry to wet eolian depositional system, Burns formation, Meridiani Planum, Mars. *Earth and Planetary Science Letters*, *240*(1), 11-72. https://doi.org/10.1016/j.epsl.2005.09.039

Grotzinger, J. P., Gupta, S., Malin, M. C., Rubin, D. M., Schieber, J., Siebach, K., et al. (2015). Deposition, exhumation, and paleoclimate of an ancient lake deposit, Gale crater, Mars. *Science*, *350*(6257), aac7575. https://doi.org/10.1126/science.aac7575

Grotzinger, J. P., Sumner, D. Y., Kah, L. C., Stack, K., Gupta, S., Edgar, L., et al. (2014). A habitable fluvio-lacustrine environment at Yellowknife Bay, Gale crater, Mars. *Science*, *343*(6169), 1242777. https://doi.org/10.1126/science.1242777

Gupta, S., Dietrich, W. E., Lewis, K. W., Kite, E., Mondro, C. A., Schieber, J., ... & Fraeman, A. (2023, March). 'High' but not so dry on Aeolis Mons: Transient lake systems in Hesperian deserts in Gale crater. In *54th Lunar and Planetary Science Conference* (Vol. 54, p. 2707).

Hapke, B. (1989). The surface of Io: A new model. *Icarus*, *79*(1), 56-74. https://doi.org/10.1016/0019-1035(89)90108-5

Hazen, R. M., Papineau, D., Bleeker, W., Downs, R. T., Ferry, J. M., McCoy, T. J., ... & Yang, H. (2008). Mineral evolution. *American Mineralogist*, *93*(11-12), 1693-1720. https://doi.org/10.2138/am.2008.2955

Jaeger, W. L., Turtle, E. P., Keszthelyi, L. P., Radebaugh, J., McEwen, A. S., & Pappalardo, R. T. (2003). Orogenic tectonism on Io. *Journal of Geophysical Research: Planets*, *108*(E8). https://doi.org/10.1029/2002JE001946

Jakosky, B. M. (2021). Atmospheric loss to space and the history of water on Mars. *Annual Review of Earth and Planetary Sciences*, *49*(1), 71-93. https://doi.org/10.1146/annurev-earth-062420-052845

Keszthelyi, L., Jaeger, W., Milazzo, M., Radebaugh, J., Davies, A. G., & Mitchell, K. L. (2007). New estimates for Io eruption temperatures: Implications for the interior. *Icarus*, *192*(2), 491-502. https://doi.org/10.1016/j.icarus.2007.07.008

Keszthelyi, L., Jaeger, W. L., Turtle, E. P., Milazzo, M., & Radebaugh, J. (2004). A post-*Galileo* view of Io's interior. *Icarus*, *169*(1), 271-286. https://doi.org/10.1016/j.icarus.2004.01.005

Kirchoff, M. R., & McKinnon, W. B. (2009). Formation of mountains on Io: Variable volcanism and thermal stresses. *Icarus*, *201*(2), 598-614. https://doi.org/10.1016/j.icarus.2009.02.006

Lopes, R. M., Spencer, J. R., Perry, J., Lopes, R. M., Spencer, J. R., & Alexander, C. (2007). A summary of the Galileo mission and its observations of Io. *Io after Galileo: A new view of Jupiter's volcanic moon*, 35-59. https://doi.org/10.1007/978-3-540-48841-5_3

Malin, M. C., & Edgett, K. S. (2000). Sedimentary rocks of early Mars. *Science*, 290(5498), 1927-1937. DOI: 10.1126/science.290.5498.1927

Malin, M. C., Ravine, M. A., Caplinger, M. A., Tony Ghaemi, F., Schaffner, J. A., Maki, J. N., et al. (2017). The Mars Science Laboratory (MSL) mast cameras and descent imager: Investigation and instrument descriptions. *Earth and Space Science*, *4*(8), 506–539. https://doi.org/10.1002/ 2016EA000252

Mangold, N., Gupta, S., Gasnault, O., Dromart, G., Tarnas, J. D., Sholes, S. F., ... & Williford, K. H. (2021). Perseverance rover reveals an ancient delta-lake system and flood deposits at Jezero crater, Mars. *Science*, *374*(6568), 711-717. DOI: 10.1126/science.abl4051

Masursky, H. (1973). An overview of geological results from Mariner 9. *Journal of Geophysical Research*, *78*(20), 4009-4030. https://doi.org/10.1029/JB078i020p04009

McEwen, A. S., Keszthelyi, L. P., Lopes, R., Schenk, P. M., & Spencer, J. R. (2004). The lithosphere and surface of Io. *Jupiter: The Planet, Satellites and Magnetosphere*, 1, 307-328.

McKinnon, W. B., Schenk, P. M., & Dombard, A. J. (2001). Chaos on Io: A model for formation of mountain blocks by crustal heating, melting, and tilting. *Geology*, *29*(2), 103-106. https://doi.org/10.1130/0091-7613(2001)029<0103:COIAMF>2.0.CO;2

McLennan, S. M., Bell iii, J. F., Calvin, W. M., Christensen, P. R., Clark, B. D., De Souza, P. A., ... & Yen, A. (2005). Provenance and diagenesis of the evaporite-bearing Burns formation, Meridiani Planum, Mars. *Earth and Planetary Science Letters*, *240*(1), 95-121. https://doi.org/10.1016/j.epsl.2005.09.041

Milliken, R. E., Grotzinger, J. P., & Thomson, B. J. (2010). Paleoclimate of Mars as captured by the stratigraphic record in Gale Crater. *Geophysical Research Letters*, *37*(4). https://doi.org/10.1029/2009GL041870

Mondro, C. A., Fedo, C. M., Grotzinger, J. P., Lamb, M. P., Gupta, S., Dietrich, W. E., ... & Vasavada, A. R. (2025). Wave ripples formed in ancient, ice-free lakes in Gale crater, Mars. *Science Advances*, *11*(3), eadr0010. DOI: 10.1126/sciadv.adr0010

Moore, J. M., Sullivan, R. J., Chuang, F. C., Head III, J. W., McEwen, A. S., Milazzo, M. P., ... & Turtle, E. P. (2001). Landform degradation and slope processes on Io: The *Galileo* view. *Journal of Geophysical Research: Planets*, *106*(E12), 33223-33240. https://doi.org/10.1029/2000JE001375

O'Reilly, T. C., & Davies, G. F. (1981). Magma transport of heat on Io: A mechanism allowing a thick lithosphere. *Geophysical Research Letters*, *8*(4), 313-316. https://doi.org/10.1029/GL008i004p00313

Pearl, J., Hanel, R., Kunde, V., Maguire, W., Fox, K., Gupta, S., ... & Raulin, F. (1979). Identification of gaseous SO 2 and new upper limits for other gases on Io. *Nature*, *280*(5725), 755-758. https://doi.org/10.1038/280755a0

Perry, J. E., Davies, A. G., Williams, D. A., & Nelson, D. M. (2025). Hot Spot Detections and Volcanic Changes on Io during the Juno Epoch: Orbits PJ5 to PJ55. *The Planetary Science Journal*, *6*(4), 84. DOI: 10.3847/PSJ/adbae3

Radebaugh, J., Keszthelyi, L. P., McEwen, A. S., Turtle, E. P., Jaeger, W., & Milazzo, M. (2001). Paterae on Io: A new type of volcanic caldera? *Journal of Geophysical Research: Planets*, *106*(E12), 33005-33020. https://doi.org/10.1029/2000JE001406

Rapin, W., Dromart, G., Clark, B. C., Schieber, J., Kite, E. S., Kah, L. C., et al. (2023). Sustained wet–dry cycling on early Mars. *Nature*, *620*(7973), 299–302. https://doi.org/10.1038/s41586-023-06220-3

Reynolds, R. T., Squyres, S. W., Colburn, D. S., & McKay, C. P. (1983). On the habitability of Europa. *Icarus*, *56*(2), 246-254. https://doi.org/10.1016/0019-1035(83)90037-4

Scheller, E. L., Ehlmann, B. L., Hu, R., Adams, D. J., & Yung, Y. L. (2021). Long-term drying of Mars by sequestration of ocean-scale volumes of water in the crust. *Science*, *372*(6537), 56-62. DOI: 10.1126/science.abc7717

Schenk, P. M., & Bulmer, M. H. (1998). Origin of mountains on Io by thrust faulting and large-scale mass movements. *Science*, *279*(5356), 1514-1517. DOI: 10.1126/science.279.5356.1514

Schenk, P., Hargitai, H., Wilson, R., McEwen, A., & Thomas, P. (2001). The mountains of Io: Global and geological perspectives from *Voyager* and *Galileo*. *Journal of Geophysical Research: Planets*, *106*(E12), 33201-33222. https://doi.org/10.1029/2000JE001408

Seeger, C., de Kleer, K., Williams, D., Perry, J., Davies, A., & Nelson, D. M. (2024). Insights Into Surface Evolution on io Based on Junocam PJ57 and PJ58 Flybys. In *Geological Society of America Abstracts* (Vol. 56, p. 405067).

Sheppard, R. Y., Milliken, R. E., Parente, M., & Itoh, Y. (2021). Updated perspectives and hypotheses on the mineralogy of lower Mt. Sharp, Mars, as seen from orbit. *Journal of Geophysical Research: Planets*, 126(2), e2020JE006372. https://doi.org/10.1029/2020JE006372

Siebach, K. L., & Grotzinger, J. P. (2014). Volumetric estimates of ancient water on Mount Sharp based on boxwork deposits, Gale Crater, Mars. *Journal of Geophysical Research: Planets*, *119*(1), 189–198. https://doi.org/10.1002/2013JE004508

Soffen, G. A. (1976). Scientific results of the Viking missions. *Science*, *194*(4271), 1274-1276. DOI: 10.1126/science.194.4271.1274

Spencer, J. R., Jessup, K. L., McGrath, M. A., Ballester, G. E., & Yelle, R. (2000). Discovery of gaseous S2 in Io's Pele plume. *Science*, *288*(5469), 1208-1210. DOI: 10.1126/science.288.5469.1208

Spencer, D. C., Katz, R. F., & Hewitt, I. J. (2020). Magmatic intrusions control Io's crustal thickness. *Journal of Geophysical Research: Planets*, *125*(6), e2020JE006443. https://doi.org/10.1029/2020JE006443

Squyres, S. W., Arvidson, R. E., Bell III, J. F., Bruckner, J., Cabrol, N. A., Calvin, W., ... & Yen, A. (2004a). The Spirit rover's Athena science investigation at Gusev crater, Mars. *Science*, *305*(5685), 794-799. DOI: 10.1126/science.3050794

Squyres, S. W., Arvidson, R. E., Bell Iii, J. F., Bruckner, J., Cabrol, N. A., Calvin, W., ... & Yen, A. (2004b). The Opportunity rover's Athena science investigation at Meridiani Planum, Mars. *Science*, *306*(5702), 1698-1703. DOI: 10.1126/science.1106171

Squyres, S. W., Grotzinger, J. P., Arvidson, R. E., Bell III, J. F., Calvin, W., Christensen, P. R., ... & Soderblom, L. A. (2004c). In situ evidence for an ancient aqueous environment at Meridiani Planum, Mars. *Science*, *306*(5702), 1709-1714. DOI: 10.1126/science.1104559

Strom, R. G., Schneider, N. M., Terrile, R. J., Cook, A. F., & Hansen, C. (1981). Volcanic eruptions on Io. *Journal of Geophysical Research: Space Physics*, *86*(A10), 8593-8620. https://doi.org/10.1029/JA086iA10p08593

Thomson, B. J., Bridges, N. T., Milliken, R., Baldridge, A., Hook, S. J., Crowley, J. K., ... & Weitz, C. M. (2011). Constraints on the origin and evolution of the layered mound in Gale Crater, Mars using Mars Reconnaissance Orbiter data. *Icarus*, 214(2), 413-432. https://doi.org/10.1016/j.icarus.2011.05.002

Turtle, E. P., Jaeger, W. L., Keszthelyi, L. P., McEwen, A. S., Milazzo, M., Moore, J., ... & Schuster, P. (2001). Mountains on Io: High-resolution *Galileo* observations, initial interpretations, and formation models. *Journal of Geophysical Research: Planets*, *106*(E12), 33175-33199. https://doi.org/10.1029/2000JE001354

Watters, T. R., McGovern, P. J., & Irwin Iii, R. P. (2007). Hemispheres apart: The crustal dichotomy on Mars. *Annual Review of Earth and Planetary Sciences*, *35*(1), 621-652. https://doi.org/10.1146/annurev.earth.35.031306.140220

Williams, D. A., Keszthelyi, L. P., Crown, D. A., Yff, J. A., Jaeger, W. L., Schenk, P. M., ... & Becker, T. L. (2011). *Geologic Map of Io*. US Department of the Interior, US Geological Survey.

Willson, R. W. (1924) Astronomical Notes on the Maya Codices (Peabody Museum of American Archaeology and Ethnology, Cambridge, MA).

C h a p t e r 2

A SEARCH FOR INFLUENCES OF TIDAL STRESSES ON SURFACE FEATURE FORMATION ON IO

Christina Seeger[1] & Katherine de Kleer[1]

"So have I seen Passion and Vanity stamping the living magnanimous earth, but the earth did not alter her tides and her seasons for that."

Moby Dick, Chapter 48: The First Lowering

Abstract

Mountains and paterae are distinctive features on the surface of Io whose relationship to each other and formation mechanisms have been the subject of long debate. Though mountain formation likely stems from much deeper in the crust than the ultimate exit of magma onto the surface in the form of depressed paterae, both feature types exhibit distinctive elongate shapes, and in the case of paterae, a characteristic planform aspect ratio of 2:3 (short:long axis). We present the first investigation into whether tidal stresses may play a role in the formation of these features on the surface by modeling the maximum compressive and tensional tidal stress experienced at each mountain and patera location throughout Io's orbit, and comparing it to the orientation of the feature on the surface, hypothesizing that tensional stress in one direction may result in a perpendicularly-oriented patera, and compression could produce perpendicular mountains. While we found no significant perpendicular relationships between features and stresses, mountains are significantly likely to form ~30° or ~60° offset from the orientation of the maximum compressive stress vector at that location. The paterae, in contrast, have a weakly nonuniform offset from stress, but without a dominant preferred orientation. The strongest relationships discovered relate to regional trends in

[1] Division of Geological and Planetary Sciences, California Institute of Technology, Pasadena, CA 91125, USA.

orientation: paterae in the subjovian hemisphere are highly unlikely to be oriented NE-SW, while the antijovian hemisphere is statistically uniform in orientation; we suggest the presence of Loki Patera may influence the formation of proximal paterae due to subsurface magma movement.

1. Introduction

Io is a world of intense volcanism, driven by its eccentric orbit forced by resonance with Europa and Ganymede (Peale et al., 1979). Tidal stresses resulting from this eccentric orbit frictionally heat Io's interior, melting it enough to frequently and powerfully expel lava onto the surface in dramatic volcanic eruptions that occur so frequently they resurface the moon at a rate of ~ 0.1-1 centimeter per year (Carr et al., 1998; Geissler et al., 2004; Johnson et al., 1979). Over geologic time, the flows create layers of basaltic to possibly ultramafic crust, interbedded with sulfur-rich deposits and sulfur dioxide frost, that is estimated to be 13-30 kilometers thick (Jaeger et al, 2003; Kirchoff & McKinnon, 2009; Schenk et al., 2001). This layered crust is compressed continuously under deep crustal subsidence stresses that are accommodated in the lithosphere by intense subsurface faulting, which can give rise to a suite of imposing up-thrust tectonic mountains in the form of stepped plateaus and tilted blocks rising up to 16 kilometers high (McEwen et al., 2004; McKinnon et al., 2001; Schenk & Bulmer 1998; Schenk et al., 2001; Turtle et al., 2001). Unlike on Earth, where long mountain chains form due to plate movements, Io's mountains form as tall, isolated, usually elongate massifs rising abruptly from the smooth plains below like islands (e.g., Schenk et al, 2001; Turtle et al., 2001; Williams et al., 2011).

Eruptions are centered around paterae, which are depressed caldera-like features with steep walls, flat floors, and arcuate margins, and often have lava flows extending outwards from them (Radebaugh et al., 2001). Thermal emission from these volcanic eruptions is easily detectable from both spacecraft and ground-based observing on Earth (Davies et al., 2001; 2010; 2024; de Kleer et al., 2019a; de Pater, et al., 2017; Lopes et al., 2001; McEwen et al., 1998; Perry et al., 2024; Veeder et al., 1994). The formation and eruptive mechanisms for paterae are not entirely understood, but hypothesized models include magma rising from

either the aesthenosphere or a magma ocean to feed isolated magma chambers and crustal intrusions that can eventually exploit the tectonically fractured subsurface to rise to the surface (Davies et al., 2006; Jaeger et al., 2003; Keszthelyi et al., 2004; Spencer et al., 2020). Alternatively, eruptions may be fed by hot-spot type volcanism, where magma ascends through crustal weaknesses in a heat-pipe regime (Keszthelyi et al., 2004; 2007; Kirchoff & McKinnon, 2009; McKinnon et al., 2001; O'Reilly & Davies, 1981). The presence or absence of an interconnected subsurface melt layer is poorly constrained, but has implications for the eruptive patterns at paterae and also the dissipation of tidal stresses throughout Io. The absence of such a layer requires heat dissipation through solid crust, meaning volcanic activity would likely correlate with heating centers. A melt layer, however, allows heat to be redistributed laterally, and volcanoes can form away from regions of increased tidal heating. Recent observations from the *Juno* spacecraft help constrain Io's interior, suggesting that a magma ocean is unlikely (Park et al., 2024) but a thin magma ocean at a depth of ~>250 km is still compatible with observations (Aygün & Čadek, 2025). While it is not yet well understood which of these mechanisms is dominant in forming these surface features, it is possible (even probable) that there many mechanisms driving the formation of these features.

Previous studies have attempted to constrain the relationship between mountains and paterae. On a global scale, mountains and paterae are statistically anticorrelated, concentrated in opposite hemispheres offset 90 degrees from each other with two significant groups of paterae clustered near the subjovian and antijovian points (Hamilton et al., 2013; Kirchoff et al., 2010; Radebaugh et al., 2001; Schenk et al., 2001; Tackley et al., 2001; Veeder et al., 2012). However, there are also many local examples of mountain/paterae associations (e.g., Ahern et al., 2017; Carr et al., 1998; Jaeger et al., 2003; Turtle et al., 2001), with examples suggesting patera formation can occur as mountains are rifted apart (Bunte et al., 2010; Seeger et al., 2025). No previous studies have identified a mechanism for influencing the orientation of mountains and paterae on the surface in a preferential way. An intuitive relationship is that of compressive stresses uplifting mountains perpendicular to the direction of principle stress, and tensile stresses rifting the crust orthogonal to the stresses.

In this study, we consider the time-varying compressional and tensile stresses from tides, which have a precedent for controlling volcanic activity (e.g., de Kleer et al., 2019). These phenomena are not limited to Io: Enceladus' plumes have characteristic timing, and on Earth, certain volcanoes like Mount Etna and Mount Ruapehu show sensitivity to tidal forces near eruption time (Běhounková et al., 2015; Hedman et al., 2013; Hurford et al., 2007; Sottili & Palladino, 2012; Girona et al., 2018). Io's own Loki Patera shows a ~460 day cycle that may be linked to periodic variations in Io's eccentricity caused by forcing from Europa and Ganymede (de Kleer er al., 2019). Tidal influence on Io's surface features has precedent, albeit on a much thinner layer of crust that may be more responsive to outside forcing: Bart et al. (2004) demonstrated small-scale ridges on the kilometer scale had alignment with the tidal stress field, suggesting they formed from tidal flexing. Therefore, by mapping the elongate compressional (mountains) and extensional (paterae) surface features globally and comparing their orientations to the tidal stresses they experience each orbit, this study constrains the influence of tidal stresses on the formation and expression of these features across the surface of Io.

2. Methods

2.1 Feature Mapping

Previous mapping efforts by Williams et al. (2011) outlined the extent of mountains and paterae on the surface of Io, using the USGS global basemap of Io (Williams et al., 2011). We used this geologic map, in concert with the 1 km/pixel global basemap of Io derived from *Voyager* and *Galileo* imagery, and the 15% of the surface that was imaged by *Galileo* at a higher resolution of 500 m/pixel or better. We use the publicly available Williams et al. (2021) database for the mosaiced *Voyager*/*Galileo* imagery as a basemap and geologic map shapefiles, using ESRI ArcGIS Pro™ software. The published geologic map contains 140 mountains, 172 hot spots based on thermal observations, and 432 paterae.

Paterae often contain multiple unit types within a singular feature (both bright and dark patera floor material, for example), so polygons of different unit types within each patera were

merged into a single "patera" polygon using the Dissolve Tool (leaving "multipart features" and "unsplit lines" unchecked); three features severed by the central meridian were also merged, resulting in a total of 430 paterae (Figure 1) Similarly, mountains with multiple components (lineated, mottled, or undivided) were merged together and "Layered Plains" units were excluded based on the Unit field, resulting in a total of 120 mountains in the dataset (Figure 1).

The basemap is often presented using a simple cylindrical map projection, which preserves angles but distorts shapes and areas of features, especially at high latitudes. Care must be taken to ensure the shapes of paterae and mountains are not misinterpreted as elongate due to map projection distortion. Distortions of distances, areas, or angles can introduce considerable error in measurements made in planetary contexts. Kneissl et al. (2011) present a methodology to eliminate measurement distortion and create map-projection-independent crater size-frequency distributions for age dating, which requires that each crater be reprojected into a stereographic map projection centered on the center point of the crater. Terrestrial maps with stereographic projections are most commonly used over polar regions or small continents like Australia, where the map is conformal; though extreme distortions occur at the periphery, in the center, shapes are well preserved, directions are true, and lines drawn through the center point are great circles, meaning length and width measurements are geodesic and unaffected by the map projection. Therefore, in order to accurately measure the length, width, and resulting aspect ratio of each patera and mountain on Io, the map (using the standard GCG Io 2000 geographic coordinate system) was reprojected to a Stereographic (Sphere) projection using the polygon's midpoint latitude and longitude as the center parallel and meridian of the projection. While projected, we then ran the Minimum Bounding Geometry—Rectangle by Width tool to create a rectangle best representing the length and width of the feature, as well as the orientation from North of the long axis.

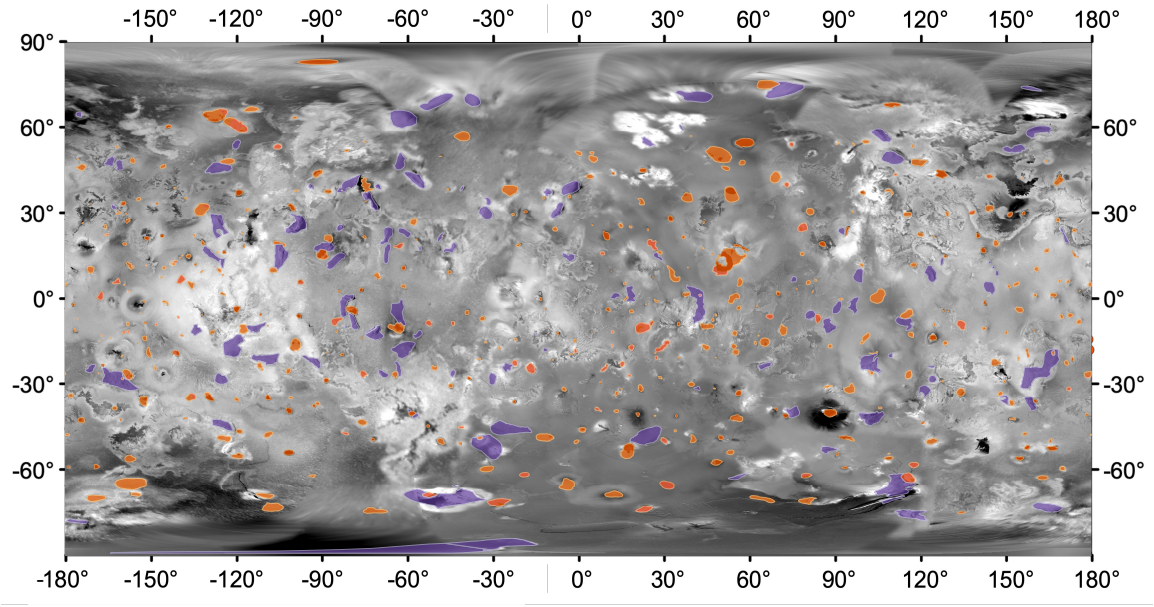

Figure 1. Map of locations of paterae (orange) and mountains (purple) used in this study, derived from USGS geologic units shapefiles. Combined *Voyager/Galileo* basemap and polygons are presented in a simple cylindrical projection centered on the subjovian point (0°W). Longitudes are given in 0-180° format, east positive.

2.2 Tidal Modelling

Io's orbital resonance with Europa and Ganymede produces an eccentric orbit, which results in diurnal tidal stresses in the crust that change in magnitude and orientation throughout its ~42.5 hour orbit around Jupiter (e.g., Peale et al., 1979; Ross & Schubert, 1985; Ross et al., 1990; Segatz et al., 1988). These stresses can be modeled with the open-source 2D numerical program software SatStressGUI, which calculates the compression and tension experienced at each point on the surface throughout a single orbit (Kay & Kattenhorn, 2010; Patthoff et al., 2016). SatStressGUI, and its predecessor SatStress (Wahr et al., 2009) uses a four-layer viscoelastic satellite model consisting of two-part lithosphere (a rigid upper lithosphere (Layer 1 or L1) and ductile lower lithosphere (L2)), ductile asthenosphere (L3), and combined mantle and core (L4), and has been used widely to model tidal stresses on Europa and other moons (e.g., Beuthe, 2015; Groenleer & Kattenhorn, 2008; Jara-Orué &

Vermeersen, 2011; Olgin et al., 2011; Smith-Konter & Pappalardo, 2008). The model was adapted to Io by adjusting the input parameters to match a range of assumptions about Io's interior composition based on ground-based and spacecraft observations. These input parameters include mass of Jupiter, eccentricity of Io's orbit (0.0041, Greenberg, 1982), obliquity (0.002, Baland et al., 2012), semimajor axis (4.21 x 108 m), and the density, thickness, viscosity, Young's Modulus, and Poisson's ratio of each layer (Table 1), modeled after Patthoff & Davies (2017). Because the properties of Io's interior are poorly constrained and the presence of an interconnected melt layer has been debated until recent observations precluded a shallow melt layer (e.g., Aygün & Čadek, 2025; Khurana, et al., 2011; Park et al., 2025), a range of values were tested and stresses were modeled for both the presence and absence of a global magma ocean. To model a case with no ocean layer, we make L2 extremely thick, thus negating the effects of the L3 layer on L1 and L2; this method has been used previously for (possible) ocean worlds (e.g., Rhoden et al., 2015; 2017). The thin liquid layer of L3 decouples the mantle and core from the lithosphere layers such that they have a negligible effect on tidal stresses on the surface (Rhoden et al., 2017 showed the L4 contribution to the magnitude of tidal stresses to be <1%).

Table 1. Range of input parameters tested for tidal model in SatStressGUI. Bold values in parentheses are values used for model case with no magma ocean used to calculate stress orientations for the remainder of results.

Layer	Density (kg/m3) (x1000)	Young's Modulus (Pa)	Poisson's Ratio	Thickness (km)	Viscosity (Pa s)
L1: Upper Lithosphere	2.3 - 3.0 (**3.0**)	1 E9 - 1 E11 (**1 E11**)	0.2 - 0.3 (**0.2**)	5 - 50 (**5**)	1 E19 - 1 E26 (**1 E25**)
L2: Lower Lithosphere	2.5 - 3.2 (**3.2**)	1 E9 - 1 E11 (**1 E10**)	0.2 - 0.3 (**0.2**)	10 - 863 (**863**)	1 E9 - 1 E20 (**1 E14**)
L3: Asthenosphere	3.3 - 3.7 (**3.7**)	**0**	**0.5**	1 - 20 (**10**)	0 - 1 E6 (**1 E2**)
L4: Mantle + Core	4.5 - 6.0 (**5**)	1 E9 - 1 E12 (**1 E12**)	0.2 - 0.3 (**0.2**)	934 - 1806 (**944**)	**1 E4**

Though a range of input parameters were tested, including the presence and absence of a magma ocean, we found that changing parameters changed the amplitude of the resulting maximum compressive and tensile stresses, but changed the timing of peak diurnal stress by less than 30° in mean anomaly. Therefore, for the remainder of the study we focus only on the results from the case with no magma ocean, treating it as representative of the range of possible modeled results. Even if the timing and amplitude of some of these stresses are different for the different cases, the orientation of the *maximum* compressive and tensile stress is not changing significantly, which is the parameter we are using to compare to surface features. Stresses were modeled for every 10 degrees of mean anomaly (Figure 2). The magnitude-weighted average stress orientation was also calculated for each patera and mountain.

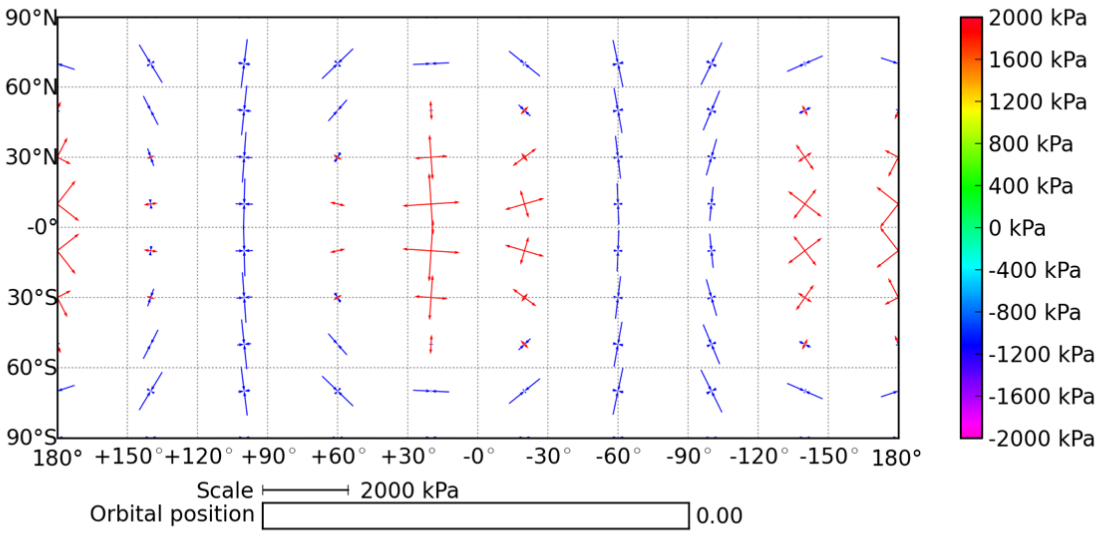

Figure 2. Map view of modeled diurnal tidal stresses calculated with SatStressGUI starting at periapsis and progressing in 30 degree increments until a full orbit is reached throughout animation. Stresses were modeled for three different conditions: no magma ocean (shown here, using bold parameters in Table 1), magma ocean with thin lithosphere, and magma ocean with thick lithosphere. Tension (red arrows) is positive.

From this global tidal stress modeling, we can then extract the tidal stresses modeled at the latitude and longitude location of each mountain and patera in the mapped dataset. The maximum compressional and extensional stress (and its orientation from north) experienced at each of these locations throughout Io's orbit were computed to compare to the orientations of the features.

2.3 Visual and Statistical Analysis

Rose diagrams, or circular histograms, are used across the field of Earth sciences to visualize directional data, from wind directions to fault orientations to paleomagnetic signatures, as well as throughout the solar system to map faults and straight crater rim segments (e.g., Cheng & Klimczak, 2025; Klimsczak et al., 2025). We generated rose diagrams for the measured orientations (East from North) of paterae and mountains produced with the Minimum Bounding Rectangle, as well as the orientations of the modeled maximum tensile (maximum σ_1) and maximum compressional (minimum σ_1) stresses experienced at the location of each feature during Io's orbit. Orientations are all measured 0-180° and are mirrored to better guide the eye. The difference between feature orientation and stress orientation was calculated from 0-180°, and then all differences above 90° were mirrored across the 90° axis to assess whether features were oriented parallel or perpendicular to the maximum tensile or compressional stress experienced; that is, a feature oriented 100° from the stress orientation is equivalent to being oriented 80° from the stress. Differences are plotted on a single quadrant rose diagram.

Rose diagrams are often plotted with the radius of each bin proportional to the frequency of the measurement, which can help our eyes pick out trends in the orientation data, but can be misleading in terms of how significant those trends are. A much more intuitive method is to plot equal-area rose diagrams, where the area of each bin is proportional to the frequency, rather than the radius, which is akin to plotting the square root of the frequency as the radial distance (Sanderson & Peacock, 2020). All rose diagrams are presented with a gray region representing a dataset of equal size with a uniform distribution of orientations for reference. Bin sizes were chosen using the widely adopted function recommended by Scott (1979),

where the bin width in degrees (b) is related to the range (R; 180° in our case) and sample size (N) as $b = R / (2N^{1/3})$, rounding to the nearest common fraction of 180° for ease of plotting. This bin size function is favored because it is based on a normal distribution but avoids "over smoothing" (Sanderson & Peacock, 2020; Scott, 1979). For most of our datasets on order of N=100, we use a bin size of 15°, which is a reasonable value for the given sample sizes of the datasets; a bin size of 20° or 30° is used for the smaller subgroups of data. We create the polar histograms using the polar-projected bar plot function in the Python Matplotlib library (Hunter, 2007).

In order to quantitatively evaluate the distribution of the mapped feature orientations, we applied the Kuiper test for uniformity to determine if orientations or differences between feature and stress orientations have significant preferred orientations (Jammalamadaka & Sengupta, 2001, Kuiper, 1960; Landler et al., 2018). The Kuiper test is useful for directional data, and is based on the cumulative frequency without binning the data, and therefore can show departures from a uniform distribution without binning bias. The Kuiper test p-values were calculated using the Python-based Kuiper function in the astropy package (Price-Whelen et al., 2022). The null hypothesis is that orientations are randomly drawn from a uniform distribution; Kuiper test p-values less than an alpha level of 0.01 indicate there is a preferred orientation with 99% confidence. We chose a strict confidence interval due to testing a large number of subsets of the data. Using this test, we investigate two different hypotheses: Are patera or mountain orientations non-uniform on the surface? And is there a non-uniform relationship between those feature orientations and the orientation of maximum tensile or compressive stress they experience each orbit?

3. Orientation and Distribution of Features

3.1 Patera Shapes

Radebaugh et al. (2001) provide a comprehensive review of patera morphologies on Io and report that seventy percent of the global population of paterae have a planform aspect ratio of <0.8. This is consistent with our measurements, and our further exploration of the distribution of patera ellipticity reveals that paterae have a characteristic elongate shape, with

a preferential aspect ratio of ~2/3. In our global survey of paterae, we found that 134 (31%) of paterae have an aspect ratio between 0.6-0.72 (Figure 3). The orientation of the long axis of the patera diminishes in significance for more circular paterae, so the dataset of "elongate" paterae used for the remainder of analyses is limited to those paterae with an aspect ratio <0.72, so defined because of the sharp shoulder in the patera shape distribution for features with an aspect ratio >0.72 (Figure 3).

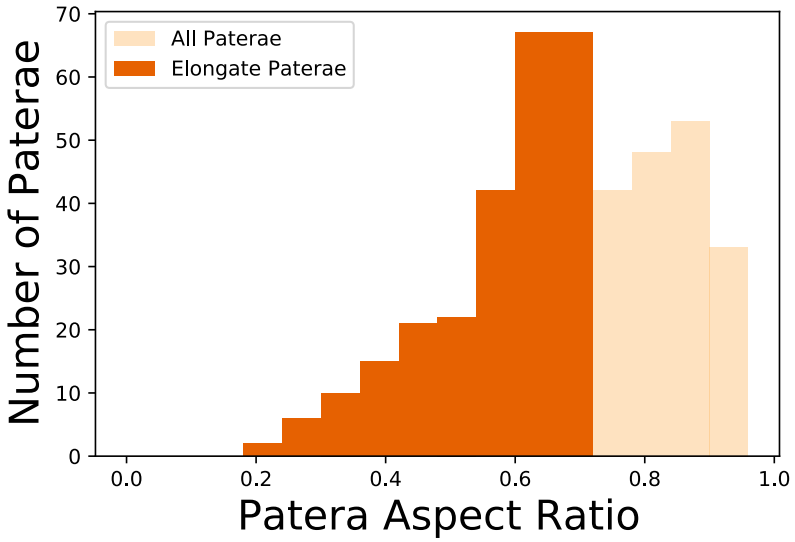

Figure 4. Distribution of patera shapes, both for full dataset of previously mapped paterae (N=430), and for the subset of paterae that are classified as "elongate" using an aspect ratio cutoff of 0.72 (exclusive) based on the peak in the aspect ratio distribution (N=252).

3.2 Patera Orientations

The long axis of each patera, as measured from a minimum bounding rectangle drawn around the feature using a stereographic projection centered on the feature midpoint, is oriented on the surface at some angle 0-180°, measured East from North where North = 0°. Because there is no directionality to the orientation data (an east-west oriented feature could have an orientation of 90° or 270° from north), we use equal-area polar histograms, or rose diagrams, with the orientations mirrored across the center of the circle in order to visualize the data.

Using the Kuiper test for uniformity, we did not find that the elongate paterae (aspect ratio <0.72) significantly deviates from a uniform distribution of orientations (Table 2). To consider any regional trends, we divided the dataset to investigate the orientations of paterae in the entire northern and southern hemispheres, polar regions (latitude > ± 45°), equatorial region (latitude < ± 30°), sub- and antijovian hemispheres, and leading and trailing hemispheres (Figure 4). The Kuiper test did not return any *p*-values below the alpha level of 0.01 for any of these subdivisions except for the subjovian hemisphere, which returned a *p*-value of 0.0005, meaning that those paterae have non-uniform orientations with 99% confidence (Table 2). These subjovian paterae do not have a unimodal preference, but rather are unlikely to be oriented NE/SW.

Table 2. Statistical significance of feature orientations and their relationship to the diurnal stress field, given as returned *p*-values from the Kuiper test of uniformity, subdivided by region. Mountain and patera orientations reflect the distribution of feature orientations where the long axis for features with planform aspect ratios <0.72 is measured east from north. Feature-Stress orientations reflect the absolute value of the difference between mountain or patera orientation and the orientation from north of maximum diurnal stress experienced by that feature each orbit.

Region	Number of Paterae	Patera Orientation	Patera-Stress Orientation	Number of Mountains	Mountain Orientation	Mountain-Stress Orientation
Global	252	0.1092	0.0583	93	0.1935	0.1354
Northern Hemisphere	122	0.9365	0.3541	47	0.0006	0.0068
Southern Hemisphere	130	0.0413	0.3154	46	0.6797	0.9081
North Pole	20	0.8121	0.8556	16	0.1172	0.3225
Equator	153	0.0974	0.111	47	0.3947	0.1907
South Pole	32	0.5927	0.1916	14	0.2378	0.0095
Subjovian Hemisphere	111	0.0005	0.0242	52	0.1312	0.032
Leading Hemisphere	118	0.4883	0.2878	56	0.2445	0.2122
Antijovian Hemisphere	141	0.8918	0.873	41	0.245	0.8811
Trailing Hemisphere	134	0.3831	0.3147	37	0.8423	0.6276

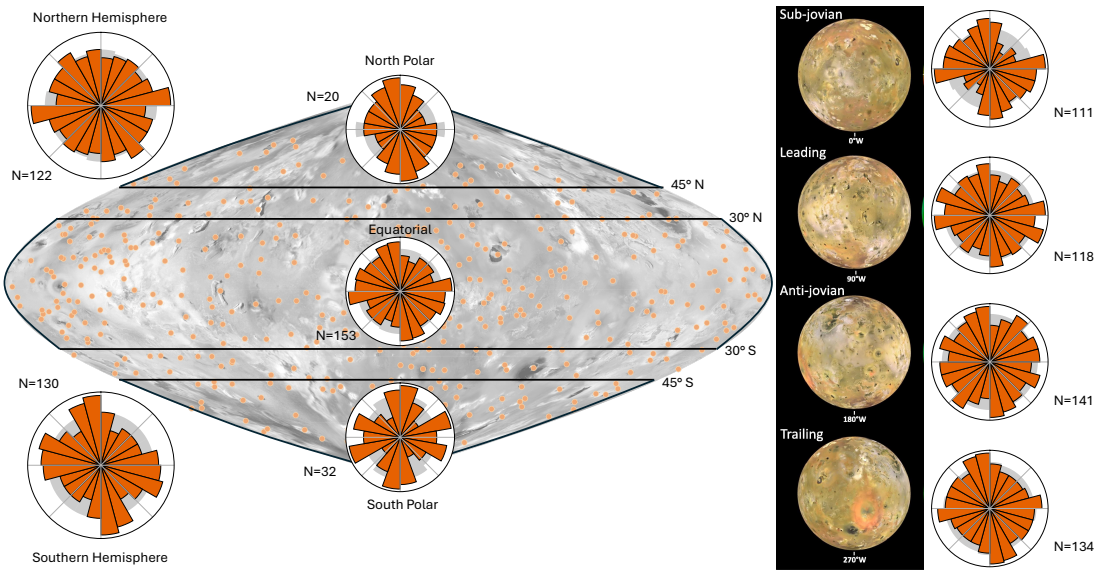

Figure 4. Orientations of long axes of elongate paterae across different regions of Io (those with an aspect ratio <0.72). North is up for all equal-area polar histograms, and orientations are measured from 0-180° and mirrored across the center of the circle The gray shaded region represents a uniform distribution for a dataset of the same size. A sinusoidal projection basemap centered on the subjovian point (0°W), with orange points corresponding to the locations of all paterae, is provided for reference. A larger bin size (20°) was used for the north and south polar rose plots due to smaller sample size, compared to 15° for all other plots.

3.3 Mountain Shapes

Unlike paterae, which have an irregular but often rounded shape, mountains tend to form as large, blocky massifs with a clear long axis. Therefore, the dataset of mountains used for this survey with aspect ratio <0.72 only excludes 27 mountains (or 22.5%) from those originally mapped (whereas 41% of paterae were excluded for being too circular). Though less pronounced than the patera shape distribution, mountains also have a characteristic shape with a large population having aspect ratios falling between 0.4-0.66 (Figure 5).

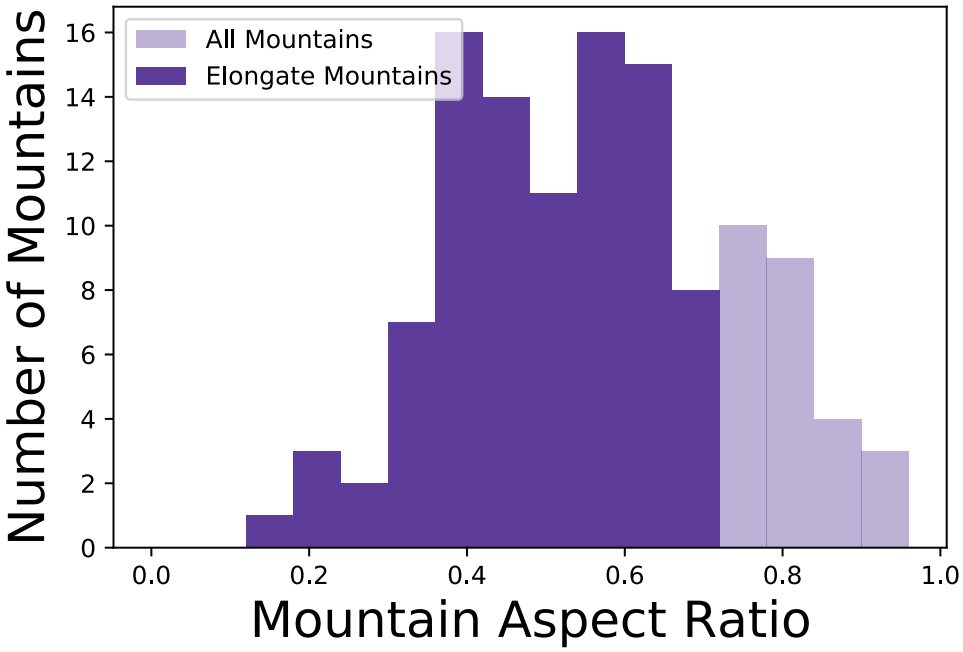

Figure 5. Distribution of mountain shapes, both for full dataset of previously mapped mountains (N=120), and for the subset of mountains that are visually elongate using the same aspect ratio cutoff of 0.72 that was used to classify paterae as "elongate" (N=93).

3.4 Mountain Orientations

We subdivide the dataset of elongate mountains by the same regions that were investigated for paterae: the entire northern and southern hemispheres, polar regions (latitude >45°), equatorial region (latitude <30°), sub- and antijovian hemispheres, and leading and trailing hemispheres (Figure 6). None of these subsets, nor the global dataset of elongate mountains (aspect ratio <0.72), can be shown to be non-uniform with the Kuiper test for uniformity, with the exception of the northern hemisphere, which returns a *p*-value of 0.006, meaning that northern mountains have a preferential orientation with 99% confidence (Table 2). These mountains are much more likely to be oriented N/NW-S/SE, and unlikely to be oriented E-W. Though the rest of the regional subdivisions do not show a significant deviation from uniform, the N/S preferential trend is visible in the subjovian and leading hemispheres as well.

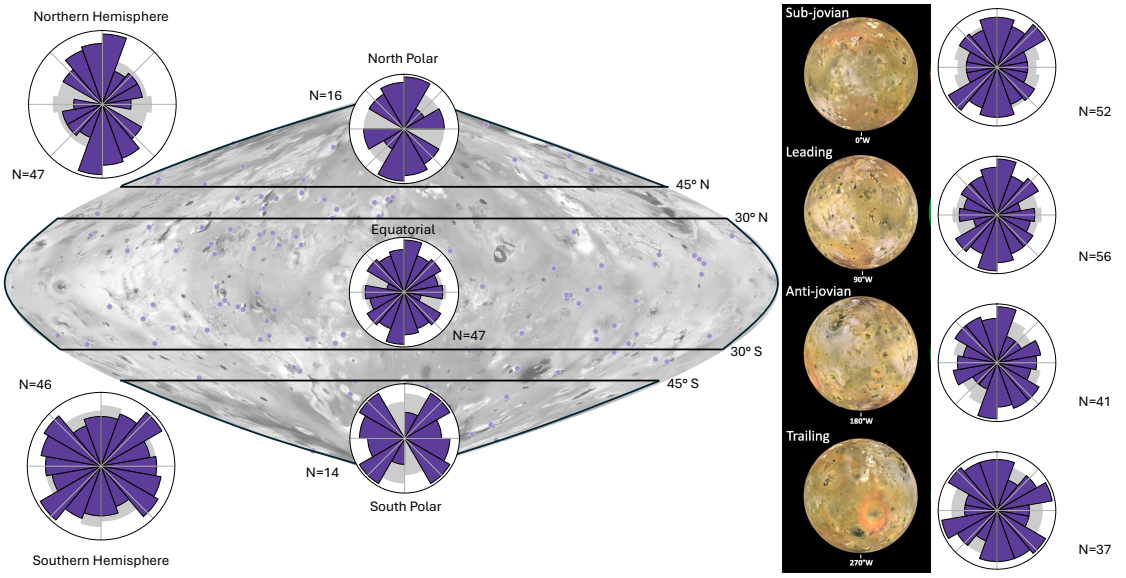

Figure 6. Orientations of long axes of elongate mountains across different regions of Io (those with an aspect ratio <0.72). North is up for all equal-area polar histograms, and orientations are measured from 0-180° and mirrored across the N-S meridian. The gray shaded region represents a uniform distribution for a dataset of the same size. A sinusoidal projection basemap centered on the subjovian point (0°W), with purple points corresponding to the locations of all mountains, is provided for latitudinal reference. For longitudinal reference, the USGS color mosaic has been orthographically re-projected to show the subjovian hemisphere (-90°–0°–90°), leading (-180°–0°), antijovian (90°–180°– -90°) and trailing (0°–180°) hemispheres of Io.

4. Tidal stresses and their relationship with feature orientation

4.1 Modeled stress results

Diurnal stresses were modeled using SatStressGUI, a four-layer viscoelastic model for orbital bodies (Kay & Kattenhorn, 2010; Patthoff et al., 2016; Wahr et al., 2009). The σ_1 and σ_3`stress components were calculated at the latitude and longitude of each patera and mountain midpoint through one orbit of Io around Jupiter, using a range of input parameters. These stress vectors have an amplitude, measured in kPa, and an orientation from north on the surface from 0-180°. We found that changing the thickness and density of each of the four layers in the model affected the amplitude of the stresses experienced, but not the timing

or orientations of them. Therefore, all stresses presented in the following results are based on the input parameters for a case without a magma ocean, as presented in Table 1.

Each point on Io's surface experiences a rotating stress field with tension and compression occurring in different directions at different times throughout the orbit. These timing and amplitude of the peak stress experienced at each feature location varies with the feature's position on the moon (Figure 7).

Because we are most interested in the peak stresses experienced by these features—peak extension for paterae, peak compression for mountains—we calculate the maximum σ_1 value (using the convention where tension is positive) experienced by each patera, and the corresponding orientation on the surface of the stress vector, and the minimum σ_3 value and corresponding orientation experienced by each mountain. The average stress experienced at each feature, weighted by stress magnitude, was also calculated, but did not have any statistically significant relationship to feature orientation. We focus on maximum stress because the magnitude of these tidal stresses is one to two orders of magnitude smaller than the compressive breaking strength of basalt at ambient temperature on Earth (Cardarelli, 2018), so the maximum stress is necessary to come close to influencing fault movement. Of course, uniquely Ionian processes affecting the strength of the crust, such as sulfur dioxide frost interbeds, crystal size, temperature gradients, and lava flow morphology all influence (and possibly reduce) the breaking strength of the crust, bringing it closer to the range of modeled maximum stresses.

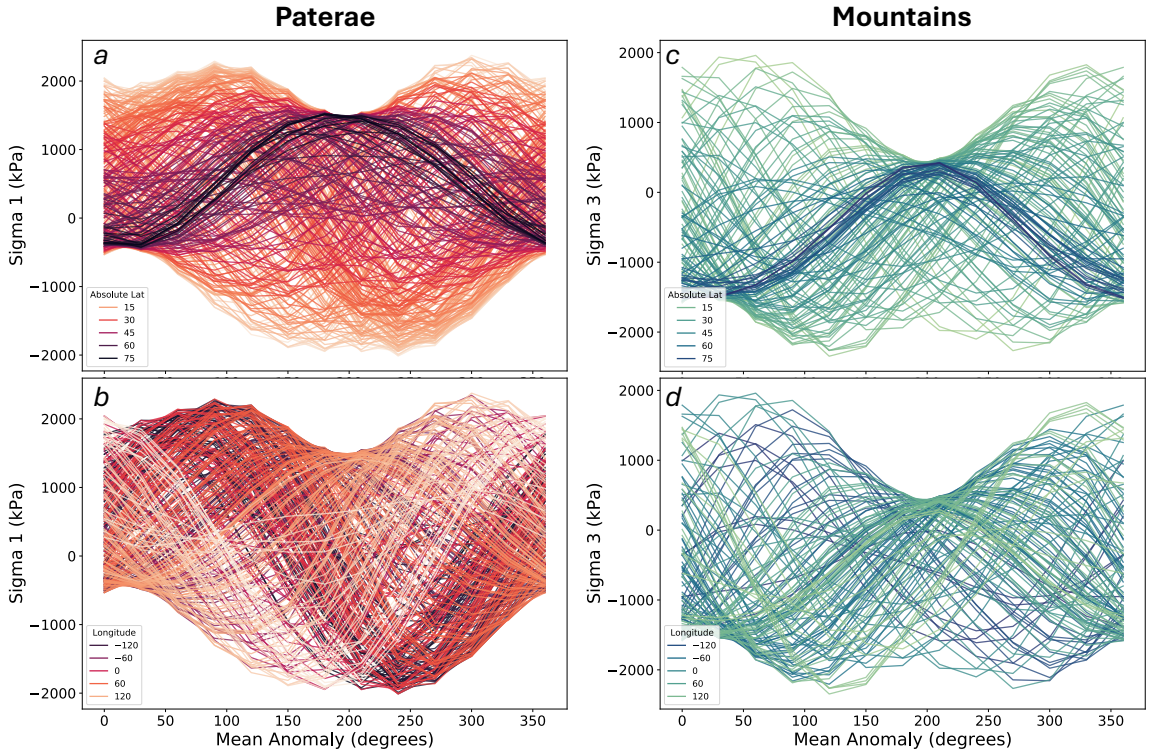

Figure 7. Model outputs from SatStressGUI for diurnal tidal stresses experienced at the location of each feature in the study throughout one orbit of Io around Jupiter (mean anomaly of zero corresponds to periapsis), at 30° increments. Stresses were modeled for σ_1 at all paterae (*a, b*) and σ_3 at all mountains (*c, d*). (*a*) and (*c*) show the change in timing of peak stress for features located near the equator (lighter colors) vs. the poles (darker colors), plotted as absolute value of latitude. (*b*) and (*d*) show the change in timing of peak stress for features at different longitudes around the moon, from the subjovian point at 0° (darker colors) around 360° to the east (lighter colors).

4.2 Correlations between stresses and features

We consider whether tidal stresses may influence the formation of the populations of elongate paterae that have a measurable orientation on the surface. For each location on Io's surface with one of these features, we extract the orientation and magnitude of the modeled maximum compressive and tensile stress experienced during one orbit of Jupiter at that location. The difference between the feature orientation and the maximum stress orientation guides our study: compressive stresses in one direction may produce uplifted mountains

perpendicular to stress, and extension in one direction may result in elongate paterae perpendicular to stress as the crust opens like a fissure. We therefore calculate the difference between each feature orientation and the orientation of the maximum stress it experiences, and mirror these differences across the x-axis to better assess the parallel vs. perpendicular cases (Figure 8). That is, a feature oriented 100° from the orientation of maximum stress is the same as being oriented 80° from said stress vector, as both are 10° from perpendicular.

We present the overall relationships between all elongate (aspect ratio <0.72) paterae and mountains and their corollary maximum stress vectors in Figure 8, but calculated similar distributions for all the regions outlined in Figure 4 and Figure 6. Polar histograms of the difference between the two orientations are displayed in a single quadrant to highlight parallel and perpendicular relationships, but the Kuiper test for uniformity was performed on the differences as measured 0-180° (Table 2).

The differences between paterae and stress direction do not have a non-uniform distribution indicating a preferential orientation (p-value of 0.0583). The patera orientation distribution may be multimodal, which is why the first-order Kuiper test fails to find a significant result in the orientations; visual inspection of the rose plots suggests there may be peaks at ~0° and 90°. The Kuiper test also fails to detect any significant non-uniformity in the regional subsets analyzed in Figure 4. The subjovian hemisphere paterae, which demonstrated a strong preference away from NE/SW orientations, does not demonstrate a significant preferential offset from stress orientation (p-value = 0.0242).

Similarly, the mountain dataset does not exhibit a correlation between feature orientation and stress direction (p-value = 0.1354), though there are larger populations of mountains oriented 0-30° and 60° from peak stress orientation than other angles. The northern hemisphere, which has a significant preferential N-S orientation, also has a significant preferential offset from stress (p-value = 0.0068) with mountains most likely to be within 30° of parallel to stress. The south polar region exhibits a weaker but significant offset as well (p-value = 0.0095), with the most likely offsets being 25°or 60°, but caution should be exercised in interpreting this relationship due to the very small number of features in this region (N=14).

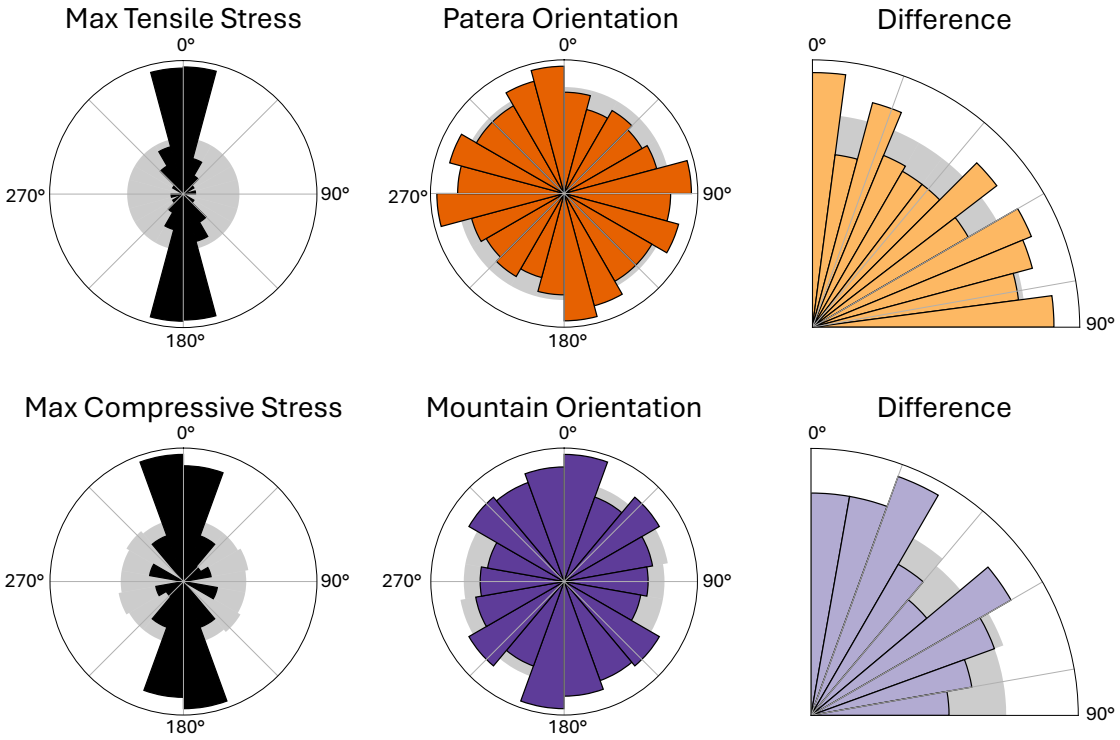

Figure 8. Orientations of elongate paterae (N=242), mountains (N=93), modeled maximum diurnal tidal stresses experienced at each feature location, and the difference between them for each feature. All orientations are measured in degrees east from north, and gray regions represent a uniform distribution for each dataset. Differences greater than 90 are reflected up over the x-axis to better visualize features parallel vs. perpendicular to stresses.

5. Discussion

5.1 Patera Stress Relationships

While the mechanisms surrounding tidal influence on mountain and patera formation are unclear, the spatial relationships between these features and the modeled stress field are important. We did not find any regions where there is a significant preferential orientation of features perpendicular to peak stress with an intuitive relation to the stress field.

Paterae are surface features deeply connected to the movement of magma upward and outward across Io's plains. They are much deeper than volcanic calderas on Earth, with walls that can exceed the Grand Canyon in depth (Radebaugh et al., 2001; White & Schenk, 2015). There are several models for the movement of magma to the surface to express as paterae,

including using faulted crust as a pathway to the surface, or upwelling and melting through sulfur dioxide frost layers (Davies et al., 2006; Jaeger et al., 2003; Keszthelyi et al., 2004; 2007; Kirchoff & McKinnon, 2009; McKinnon et al., 2001; O'Reilly & Davies, 1981; Spencer et al., 2020). In either model, it is not unreasonable to predict that periodic flexing of the crust in diurnal cycles could influence the opening of fissures on the surface, perpendicular to those extensional stresses. Therefore, paterae might be expected to be better indicators of a feature-tidal stress relationship than mountains, which are thought to be generated by deep compressive crustal subsidence stresses, orders of magnitude larger than tides. The global ~uniform distribution of patera orientations and offsets from stress orientations indicates that there is no imprint of tidal stresses on the shape of paterae on the surface. However, it should be noted if these features initiate as narrow rifts, it is possible any initial shape is quickly modified by subsequent eruptive activity, new lava flows, and sapping of crater walls producing scalloped cliffsides (Moore et al., 2002). Though tidal stresses may not control the global population of patera orientations, they could still contribute to initial rifting and regional orientation trends.

For example, the strong preferential orientation of paterae in the subjovian hemisphere is striking, with a scarcity of features forming in a NE-SW orientation (Figure 4). Further subdividing this group of paterae to only include those in both the subjovian and leading hemispheres, thus encompassing one of the two antipodal clusters of paterae on Io (Kirchoff et al., 2011), yields a similar result (significantly nonuniform distribution with very few paterae oriented NE-SW; p-value = 0.0161, N=72). While the differenced distributions do not have a significantly nonuniform distribution according to the Kuiper test, they both show a large population of features oriented parallel and perpendicular to stresses. Though the subjovian hemisphere does contain a lower density of hot spots and lower heat flow, it also includes the massive and active Loki Patera, proposed to be linked to a crustal hot spot of mantle upwelling (Davies et al., 2015; Steinke et al., 2020). It is possible that the volcanic plumbing supporting this eruptive center disrupts the regional magma pathways, preventing proximal paterae from forming with the NE-SW orientation. On a longer timescale, it is possible that crustal formation from Loki-centric lava flows contributes to local

heterogeneities that then manifest in preferential rifting orientations. Ultimately, factors beyond tidal stresses must be preventing paterae from forming or remaining oriented in a NE-SW direction in the subjovian hemisphere.

5.2 Mountain Stress Relationships

Because mountain formation is hypothesized to be driven by crustal subsidence stresses—which are orders of magnitude stronger than the surface tidal stresses—we do not expect tidal stresses to be strongly influential on the mountain uplift (e.g., McEwen et al., 2004; McKinnon et al., 2001; Schenk & Bulmer 1998). Therefore, it is not surprising that the mountains globally do not have a statistical correlation with tidal stresses orientations (Figure 8). However, the preferential N-S orientation of the mountains in the northern hemisphere, as well as their tendency to form parallel to direction of maximum compression, hints that there could be some contribution from stresses to slip along faults, but more but more detailed modeling of the stress components, particularly shear, may be useful to further illuminate this relationship in future work. It is possible cyclical compression could drive incremental motion along mountain-bounding faults with a directional bias.

Perhaps more than paterae, mountains are strongly impacted by erosional processes on Io, with their dramatic scarps being softened by processes of mass wasting and erosion over geologic time on a body constantly being shaken by volcanically-induced seismicity (e.g., Moore et al., 2002; Schenk & Bulmer, 1998; Seeger et al., 2025). These erosional processes could obscure any characteristic shape a mountain has when it is freshly uplifted, softening the features and making them rounder over time. Higher resolution global coverage of Io's mountains would allow us to better distinguish scarp from slump components of individual mountains, providing a better metric to understand the distribution of orientations (Figure 5). Mountain identification is also highly dependent on solar incidence angle. Though there is some variation in incidence angle between the northern and southern hemisphere by *Galileo*, it does not appear dramatic enough to strongly skew the N-S orientation bias of the northern hemisphere mountains compared to the southern hemisphere (Figure 7 in Williams et al., 2011).

6. Conclusions

Io's diverse surface features include towering tectonic mountain massifs and depressed volcanic paterae that are diverse in size, shape, and spatial distribution. Hypothesized mountain formation mechanisms are driven by crustal subsidence stresses, which are orders of magnitude stronger than the tidal stresses that act on Io's surface, while subsurface pathways bringing magma to the surface at eruptive paterae may be more susceptible to the flexing of the crust in different orientations and to different degrees throughout Io's orbit. Because tidal stresses have been shown to affect surface feature formation elsewhere in the solar system, we modeled the tidal stresses acting on Io's surface at the locations of all elongate mountains and paterae (meaning those with an aspect ratio <0.72) to determine if tidal stresses may influence surface feature formation by affecting their shape and map-view orientation. Both compressive and extensional maximum stresses have a preferential north-south orientation. Paterae tend to be more circular in shape than mountain blocks, but those that are elongate do have a characteristic planform aspect ratio of 2:3. Globally, the orientations of both mountains and paterae cannot be shown to be non-uniform according to the Kuiper test of uniformity. Moreover, there is no significant non-uniformity their offset from the direction of maximum tensile stress (for paterae) and compressive stress (for mountains) that they experience during Io's orbit. A significant lack of paterae oriented NE-SW in the subjovian hemisphere, where Loki Patera is located, hints that there may be more complicated stresses influencing the regime, especially if Loki is a site of mantle upwelling. Mountains in the northern hemisphere show a significant trend of N-S alignment. Ultimately, though the distributions of measurements and modeled stresses do not support the hypothesized perpendicular relationships indicative of tidal stress influence on feature formation, this study reveals regional asymmetries in feature orientation and hints at relationships between feature orientation and stress that are likely compounded by crustal heterogeneities at depth influencing both tectonic uplift and magma pathways.

Acknowledgements

We thank thesis committee members Mike Lamb, John Grotzinger, and Bethany Ehlmann for their thorough comments and helpful discission about material properties on Io that helped in framing this work. Funding for this paper was provided by the NASA ROSES Solar System Workings program (through Task Order 80NM0018F0612).

Data Availability Statement

USGS geologic map shapefiles and *Voyager/Galileo* basemap are archived and freely available to the public via the Arizona State University Ronald Greeley Center for Planetary Studies (https://rgcps.asu.edu/gis_data/; Williams et al., 2021). SatStressGUI is a free and open-source program developed at NASA's Jet Propulsion Laboratory and is available for download from GitHub (https://github.com/SatStressGUI). All measured patera and mountain orientations and stress orientations can be found in Supplementary Data Tables S1 and S2.

References

Ahern, A. A., Radebaugh, J., Christiansen, E. H., Harris, R. A., & Tass, E. S. (2017). Lineations and structural mapping of Io's paterae and mountains: Implications for internal stresses. *Icarus*, *297*, 14-32. https://doi.org/10.1016/j.icarus.2017.06.004

Anderson, E. M. (1905). The dynamics of faulting. *Transactions of the Edinburgh Geological Society*, *8*(3), 387-402. https://doi.org/10.1144/transed.8.3.387

Aygün, B., & Čadek, O. (2025). Love numbers for Io with a magma ocean. *Icarus*, 116567. https://doi.org/10.1016/j.icarus.2025.116567

Baas, J. H. (2000). EZ-ROSE: a computer program for equal-area circular histograms and statistical analysis of two-dimensional vectorial data. *Computers & Geosciences*, *26*(2), 153-166. https://doi.org/10.1016/S0098-3004(99)00072-2

Baland, R. M., Yseboodt, M., & Van Hoolst, T. (2012). Obliquity of the Galilean satellites: The influence of a global internal liquid layer. *Icarus*, *220*(2), 435-448. https://doi.org/10.1016/j.icarus.2012.05.020

Bart, G. D., Turtle, E. P., Jaeger, W. L., Keszthelyi, L. P., & Greenberg, R. (2004). Ridges and tidal stress on Io. *Icarus*, *169*(1), 111-126. https://doi.org/10.1016/j.icarus.2004.01.003

Běhounková, M., Tobie, G., Čadek, O., Choblet, G., Porco, C., & Nimmo, F. (2015). Timing of water plume eruptions on Enceladus explained by interior viscosity structure. *Nature Geoscience*, *8*(8), 601-604. https://doi.org/10.1038/ngeo2475

Beuthe, M. (2015). Tides on Europa: The membrane paradigm. *Icarus*, *248*, 109-134. https://doi.org/10.1016/j.icarus.2014.10.027

Bunte, M. K., Williams, D. A., Greeley, R., & Jaeger, W. L. (2010). Geologic mapping of the Hi'iaka and Shamshu regions of Io. *Icarus*, *207*(2), 868-886. doi:10.1016/j.icarus.2009.12.006

Cardarelli, F. (2018). Rocks and Minerals. *Materials Handbook: A Concise Desktop Reference*, 883-1012. https://doi.org/10.1007/978-3-319-38925-7

Carr, M. H., McEwen, A. S., Howard, K. A., Chuang, F. C., Thomas, P., Schuster, P., ... & *Galileo* Imaging Team. (1998). Mountains and calderas on Io: Possible implications for lithosphere structure and magma generation. *Icarus*, 135(1), 146-165. Reclassified geologic units based on JunoCam imagery. https://doi.org/10.1006/icar.1998.5979

Cheng, H. C. J., & Klimczak, C. (2025). Tectonic patterns on Vesta and Ceres revealed by polygonal impact craters. *Icarus*, *433*, 116528. https://doi.org/10.1016/j.icarus.2025.116528

Davies, A. G., Keszthelyi, L. P., & Harris, A. J. (2010). The thermal signature of volcanic eruptions on Io and Earth. *Journal of Volcanology and Geothermal Research*, *194*(4), 75-99. https://doi.org/10.1016/j.jvolgeores.2010.04.009

Davies, A. G., Keszthelyi, L. P., Williams, D. A., Phillips, C. B., McEwen, A. S., Lopes, R. M., ... & Carlson, R. W. (2001). Thermal signature, eruption style, and eruption evolution at Pele and Pillan on Io. *Journal of Geophysical Research: Planets*, *106*(E12), 33079-33103. https://doi.org/10.1029/2000JE001357

Davies, A. G., Perry, J. E., Williams, D. A., Veeder, G. J., & Nelson, D. M. (2024). New global map of Io's volcanic thermal emission and discovery of hemispherical dichotomies. *The Planetary Science Journal*, *5*(5), 121. https://doi.org/10.3847/PSJ/ad4346

Davies, A. G., Veeder, G. J., Matson, D. L., & Johnson, T. V. (2015). Map of Io's volcanic heat flow. *Icarus*, *262*, 67-78. https://doi.org/10.1016/j.icarus.2015.08.003

Davies, A. G., Wilson, L., Matson, D., Leone, G., Keszthelyi, L., & Jaeger, W. (2006). The heartbeat of the volcano: The discovery of episodic activity at Prometheus on Io. *Icarus*, *184*(2), 460-477. doi:10.1016/j.icarus.2006.05.012

de Kleer, K., Nimmo, F., & Kite, E. (2019). Variability in Io's volcanism on timescales of periodic orbital changes. *Geophysical Research Letters*, *46*(12), 6327-6332. https://doi.org/10.1029/2019GL082691

Geissler, P., McEwen, A., Phillips, C., Keszthelyi, L., & Spencer, J. (2004). Surface changes on Io during the *Galileo* mission. *Icarus*, *169*(1), 29-64. https://doi.org/10.1016/j.icarus.2003.09.024

Girona, T., Huber, C., & Caudron, C. (2018). Sensitivity to lunar cycles prior to the 2007 eruption of Ruapehu volcano. *Scientific Reports*, *8*(1), 1476. https://doi.org/10.1038/s41598-018-19307-z

Greenberg, R. (1982). Orbital evolution of the Galilean satellites. *Satellites of Jupiter*, 65-92.

Groenleer, J. M., & Kattenhorn, S. A. (2008). Cycloid crack sequences on Europa: Relationship to stress history and constraints on growth mechanics based on cusp angles. *Icarus*, *193*(1), 158-181. https://doi.org/10.1016/j.icarus.2007.08.032

Hamilton, C. W., Beggan, C. D., Still, S., Beuthe, M., Lopes, R. M., Williams, D. A., ... & Wright, W. (2013). Spatial distribution of volcanoes on Io: Implications for tidal heating and magma ascent. *Earth and Planetary Science Letters*, *361*, 272-286. https://doi.org/10.1016/j.epsl.2012.10.032

Hedman, M. M., Gosmeyer, C. M., Nicholson, P. D., Sotin, C., Brown, R. H., Clark, R. N., ... & Showalter, M. R. (2013). An observed correlation between plume activity and tidal stresses on Enceladus. *Nature*, *500*(7461), 182-184. https://doi.org/10.1038/nature12371

Hunter, J. D. (2007). Matplotlib: A 2D graphics environment. *Computing in Science & Engineering*, *9*(03), 90-95. DOI: 10.1109/MCSE.2007.55

Hurford, T. A., Helfenstein, P., Hoppa, G. V., Greenberg, R., & Bills, B. G. (2007). Eruptions arising from tidally controlled periodic openings of rifts on Enceladus. *Nature*, *447*(7142), 292-294. https://doi.org/10.1038/nature05821

Jaeger, W. L., Turtle, E. P., Keszthelyi, L. P., Radebaugh, J., McEwen, A. S., & Pappalardo, R. T. (2003). Orogenic tectonism on Io. *Journal of Geophysical Research: Planets*, *108*(E8). https://doi.org/10.1029/2002JE001946

Jammalamadaka, S. R., & Sengupta, A. (2001). *Topics in circular statistics* (Vol. 5). World Scientific.

Jara-Orué, H. M., & Vermeersen, B. L. (2011). Effects of low-viscous layers and a non-zero obliquity on surface stresses induced by diurnal tides and non-synchronous rotation: The case of Europa. *Icarus*, *215*(1), 417-438. https://doi.org/10.1016/j.icarus.2011.05.034

Johnson, T. V., Cooke, I. I., Sagan, C., & Soderblom, L. A. (1979). Volcanic resurfacing rates and implications for volatiles on Io. *Nature (London);(United Kingdom)*, *280*(5725). https://doi.org/10.1038/280746a0

Keszthelyi, L., Jaeger, W., Milazzo, M., Radebaugh, J., Davies, A. G., & Mitchell, K. L. (2007). New estimates for Io eruption temperatures: Implications for the interior. *Icarus*, *192*(2), 491-502. https://doi.org/10.1016/j.icarus.2007.07.008

Keszthelyi, L., Jaeger, W. L., Turtle, E. P., Milazzo, M., & Radebaugh, J. (2004). A post-*Galileo* view of Io's interior. *Icarus*, *169*(1), 271-286. https://doi.org/10.1016/j.icarus.2004.01.005

Khurana, K. K., Jia, X., Kivelson, M. G., Nimmo, F., Schubert, G., & Russell, C. T. (2011). Evidence of a global magma ocean in Io's interior. *Science*, *332*(6034), 1186-1189. DOI: 10.1126/science.1201425

Kirchoff, M. R., & McKinnon, W. B. (2009). Formation of mountains on Io: Variable volcanism and thermal stresses. *Icarus*, *201*(2), 598-614. https://doi.org/10.1016/j.icarus.2009.02.006

Kirchoff, M. R., McKinnon, W. B., & Schenk, P. M. (2011). Global distribution of volcanic centers and mountains on Io: Control by asthenospheric heating and implications for mountain formation. *Earth and Planetary Science Letters*, *301*(1-2), 22-30. https://doi.org/10.1016/j.epsl.2010.11.018

Klimczak, C., Crane, K. T., & Byrne, P. K. (2025). Mercury has multiple, superposed global tectonic patterns. *Earth and Planetary Science Letters*, *658*, 119331. https://doi.org/10.1016/j.epsl.2025.119331

Kneissl, T., van Gasselt, S., & Neukum, G. (2011). Map-projection-independent crater size-frequency determination in GIS environments—New software tool for

ArcGIS. *Planetary and Space Science*, *59*(11-12), 1243-1254. https://doi.org/10.1016/j.pss.2010.03.015

Kuiper, N. H. (1960, January). Tests concerning random points on a circle. In *Nederlandse Akademie van Wetenschappen Proceedings Series A*, 63(1), 38-47.

Lainey, V., Duriez, L., & Vienne, A. (2006). Synthetic representation of the Galilean satellites orbital motions from L1 ephemerides. *Astronomy & Astrophysics*, **456**, 783–788. https://doi.org/10.1051/0004-6361:20064941

Landler, L., Ruxton, G. D., & Malkemper, E. P. (2018). Circular data in biology: advice for effectively implementing statistical procedures. *Behavioral Ecology and Sociobiology*, *72*, 1-10. https://doi.org/10.1007/s00265-018-2538-y

Lopes, R. M., Kamp, L. W., Douté, S., Smythe, W. D., Carlson, R. W., McEwen, A. S., ... & Soderblom, L. A. (2001). Io in the near infrared: Near-Infrared Mapping Spectrometer (NIMS) results from the *Galileo* flybys in 1999 and 2000. *Journal of Geophysical Research: Planets*, *106*(E12), 33053-33078. https://doi.org/10.1029/2000JE001463

McEwen, A. S., Keszthelyi, L., Geissler, P., Simonelli, D. P., Carr, M. H., Johnson, T. V., ... & Schubert, G. (1998). Active volcanism on Io as seen by *Galileo* SSI. *Icarus*, *135*(1), 181-219. https://doi.org/10.1006/icar.1998.5972

McEwen, A. S., Keszthelyi, L. P., Lopes, R., Schenk, P. M., & Spencer, J. R. (2004). The lithosphere and surface of Io. *Jupiter: The Planet, Satellites and Magnetosphere*, 1, 307-328.

McKinnon, W. B., Schenk, P. M., & Dombard, A. J. (2001). Chaos on Io: A model for formation of mountain blocks by crustal heating, melting, and tilting. *Geology*, *29*(2), 103-106. https://doi.org/10.1130/0091-7613(2001)029<0103:COIAMF>2.0.CO;2

Moore, J. M., Sullivan, R. J., Chuang, F. C., Head III, J. W., McEwen, A. S., Milazzo, M. P., ... & Turtle, E. P. (2001). Landform degradation and slope processes on Io: The *Galileo* view. *Journal of Geophysical Research: Planets*, *106*(E12), 33223-33240. https://doi.org/10.1029/2000JE001375

Olgin, J. G., Smith-Konter, B. R., & Pappalardo, R. T. (2011). Limits of Enceladus's ice shell thickness from tidally driven tiger stripe shear failure. *Geophysical Research Letters*, *38*(2), L02201. https://doi.org/10.1029/2010GL044950

O'Reilly, T. C., & Davies, G. F. (1981). Magma transport of heat on Io: A mechanism allowing a thick lithosphere. *Geophysical Research Letters*, *8*(4), 313-316. https://doi.org/10.1029/GL008i004p00313

Park, R. S., Jacobson, R. A., Gomez Casajus, L., Nimmo, F., Ermakov, A. I., Keane, J. T., ... & Bolton, S. J. (2025). Io's tidal response precludes a shallow magma ocean. *Nature*, *638*(8049), 69-73. https://doi.org/10.1038/s41586-024-08442-5

Patthoff, D. A., & Davies, A. G. (2017). Tidal Stresses and Volcanism on Io. In *48th Annual Lunar and Planetary Science Conference* (No. 1964, p. 1748).

Peale, S. J., Cassen, P., & Reynolds, R. T. (1979). Melting of Io by tidal dissipation. *Science*, *203*(4383), 892-894. DOI: 10.1126/science.203.4383.892

Perry, J. E., Davies, A. G., Williams, D. A., & Nelson, D. M. (2025). Hot Spot Detections and Volcanic Changes on Io during the Juno Epoch: Orbits PJ5 to PJ55. *The Planetary Science Journal*, *6*(4), 84. https://doi.org/10.3847/PSJ/adbae3

Price-Whelan, Adrian M., Pey Lian Lim, Nicholas Earl, Nathaniel Starkman, Larry Bradley, David L. Shupe, Aarya A. Patil et al. "The Astropy Project: sustaining and growing a community-oriented open-source project and the latest major release (v5. 0) of the core package." *The Astrophysical Journal* 935, no. 2 (2022): 167. DOI: 10.3847/1538-4357/ac7c74

Radebaugh, J., Keszthelyi, L. P., McEwen, A. S., Turtle, E. P., Jaeger, W., & Milazzo, M. (2001). Paterae on Io: A new type of volcanic caldera? *Journal of Geophysical Research: Planets*, *106*(E12), 33005-33020. https://doi.org/10.1029/2000JE001406

Rhoden, A. R., Henning, W., Hurford, T. A., Patthoff, D. A., & Tajeddine, R. (2017). The implications of tides on the Mimas ocean hypothesis. *Journal of Geophysical Research: Planets*, *122*(2), 400-410. https://doi.org/10.1002/2016JE005097

Rhoden, A. R., Hurford, T. A., Roth, L., & Retherford, K. (2015). Linking Europa's plume activity to tides, tectonics, and liquid water. *Icarus*, *253*, 169-178. https://doi.org/10.1016/j.icarus.2015.02.023

Ross, M. N., & Schubert, G. (1985). Tidally forced viscous heating in a partially molten Io. *Icarus*, *64*(3), 391-400. https://doi.org/10.1016/0019-1035(85)90063-6

Ross, M. N., Schubert, G., Spohn, T., & Gaskell, R. W. (1990). Internal structure of Io and the global distribution of its topography. *Icarus*, *85*(2), 309-325. https://doi.org/10.1016/0019-1035(90)90119-T

Sanderson, D. J., & Peacock, D. C. (2020). Making rose diagrams fit-for-purpose. *Earth-Science Reviews*, *201*, 103055. https://doi.org/10.1016/j.earscirev.2019.103055

Schenk, P. M., & Bulmer, M. H. (1998). Origin of mountains on Io by thrust faulting and large-scale mass movements. *Science*, *279*(5356), 1514-1517. DOI: 10.1126/science.279.5356.1514

Schenk, P., Hargitai, H., Wilson, R., McEwen, A., & Thomas, P. (2001). The mountains of Io: Global and geological perspectives from *Voyager* and *Galileo*. *Journal of Geophysical Research: Planets*, *106*(E12), 33201-33222. https://doi.org/10.1029/2000JE001408

Scott, D. W. (1979). On optimal and data-based histograms. *Biometrika*, *66*(3), 605-610. https://doi.org/10.1093/biomet/66.3.605

Seeger, C., de Kleer, K., Williams, D., Perry, J., Davies, A., & Nelson, D. M. (2024). Insights Into Surface Evolution on io Based on Junocam PJ57 and PJ58 Flybys. In *Geological Society of America Abstracts* (Vol. 56, p. 405067).

Segatz, M., Spohn, T., Ross, M. N., & Schubert, G. (1988). Tidal dissipation, surface heat flow, and figure of viscoelastic models of Io. *Icarus*, *75*(2), 187-206. https://doi.org/10.1016/0019-1035(88)90001-2

Smith-Konter, B., & Pappalardo, R. T. (2008). Tidally driven stress accumulation and shear failure of Enceladus's tiger stripes. *Icarus*, *198*(2), 435-451. https://doi.org/10.1016/j.icarus.2008.07.005

Sottili, G., & Palladino, D. M. (2012). Tidal modulation of eruptive activity at open-vent volcanoes: evidence from Stromboli, Italy. *Terra Nova*, *24*(3), 233-237. https://doi.org/10.1111/j.1365-3121.2012.01059.x

Spencer, D. C., Katz, R. F., & Hewitt, I. J. (2020). Magmatic intrusions control Io's crustal thickness. *Journal of Geophysical Research: Planets*, *125*(6), e2020JE006443. https://doi.org/10.1029/2020JE006443

Steinke, T., van Sliedregt, D., Vilella, K., Van der Wal, W., & Vermeersen, B. (2020). Can a combination of convective and magmatic heat transport in the mantle explain Io's volcanic pattern? *Journal of Geophysical Research: Planets*, *125*(12), e2020JE006521. https://doi.org/10.1029/2020JE006521

Tackley, P. J., Schubert, G., Glatzmaier, G. A., Schenk, P., Ratcliff, J. T., & Matas, J. P. (2001). Three-dimensional simulations of mantle convection in Io. *Icarus*, *149*(1), 79-93. https://doi.org/10.1006/icar.2000.6536

Turtle, E. P., Jaeger, W. L., Keszthelyi, L. P., McEwen, A. S., Milazzo, M., Moore, J., ... & Schuster, P. (2001). Mountains on Io: High-resolution *Galileo* observations, initial

interpretations, and formation models. *Journal of Geophysical Research: Planets*, *106*(E12), 33175-33199. https://doi.org/10.1029/2000JE001354

Veeder, G. J., Davies, A. G., Matson, D. L., Johnson, T. V., Williams, D. A., & Radebaugh, J. (2012). Io: Volcanic thermal sources and global heat flow. *Icarus*, *219*(2), 701-722. https://doi.org/10.1016/j.icarus.2012.04.004

Veeder, G. J., Matson, D. L., Johnson, T. V., Blaney, D. L., & Goguen, J. D. (1994). Io's heat flow from infrared radiometry: 1983–1993. *Journal of Geophysical Research: Planets*, *99*(E8), 17095-17162. https://doi.org/10.1029/94JE00637

Wahr, J., Selvans, Z. A., Mullen, M. E., Barr, A. C., Collins, G. C., Selvans, M. M., & Pappalardo, R. T. (2009). Modeling stresses on satellites due to nonsynchronous rotation and orbital eccentricity using gravitational potential theory. *Icarus*, *200*(1), 188-206. https://doi.org/10.1016/j.icarus.2008.11.002

White, O. L., & Schenk, P. M. (2015). Topographic mapping of paterae and layered plains on Io using photoclinometry. *Journal of Geophysical Research: Planets*, *120*(1), 51-61. https://doi.org/10.1002/2014JE004672

Williams, D. A., Keszthelyi, L. P., Crown, D. A., Yff, J. A., Jaeger, W. L., Schenk, P. M., ... & Becker, T. L. (2011). *Geologic Map of Io*. US Department of the Interior, US Geological Survey.

Williams, D. A., Keszthelyi, L. P., Crown, D. A., Yff, J. A., Jaeger, W. L., Schenk, P. M., ... & Becker, T. L. (2011). Volcanism on Io: New insights from global geologic mapping. *Icarus*, *214*(1), 91-112. https://doi.org/10.1016/j.icarus.2011.05.007

Williams, D. A., Nelson, D. M., & Milazzo, M. P. (2021). The Io GIS Database 1.0: a proto-Io planetary spatial data infrastructure. *The Planetary Science Journal*, *2*(4), 148. https://doi.org/10.3847/PSJ/ac097f.

Supplementary Data for Chapter 2

This section contains all data used in evaluating surface feature shape, orientation, and relationship to diurnal tidal stresses. Table S1 (p. 47-55) contains data for elongate paterae (planform aspect ratios of <0.72). Table S2 (p. 56-59) contains data for all mountains, though the elongate population with aspect ratios of <0.72 was isolated for analysis in Chapter 2. In both tables, Latitude and Longitude (0-180, East positive) correspond to the midpoint of each patera or mountain polygon. Width and Length refer to the geodesic length (in km) of the long and short axis of a minimum bounding rectangle encasing each feature. Orientation is the orientation in degrees of the long axis of that rectangle measured clockwise from north. The absolute value of the difference between the stress orientation and feature orientation is given in both the original 0-180 measurement and as 0-90, where all values >90 are reflected back up over the x-axis as in Figure 8. For Mountains, Unit corresponds to geologic units in USGS geologic map (Williams et al., 2011); Ml = Mountain, lineated; Mm = Mountain, mottled; Mu = Mountain, undivided. Note that Object_ID refers to unique identifier in ArcPro map based on drawing order; table is sorted in order of increasing latitude so some Object_ID values are slightly out of chronological order.

Table S1. Measurements and modeled stress orientations for paterae.

Object_ID	Latitude	Longitude	Width	Length	Feature_ Orientation	Aspect_ ratio	Sigma1 _max_kPa	Stress_ orientation	Orientation_ Diff_ 0-180	Orientation_ Diff_ 0-90
1	-74.743737	134.397056	15.203	24.377	63.13	0.6236	1316.47	138.18	75.05	75.05
3	-73.583586	23.195217	37.752	68.047	27.50	0.5548	1243.12	48.34	20.84	20.84
4	-72.940382	-107.21956	65.476	91.963	6.55	0.7120	1416.46	179.77	173.22	6.78
7	-69.967242	64.655206	40.398	112.165	123.79	0.3602	1400.60	7.45	116.34	63.66
9	-68.80469	-109.73564	45.241	75.672	118.09	0.5979	1414.74	2.16	115.93	64.07
10	-68.381175	-155.18873	34.312	48.860	111.47	0.7022	1161.62	36.25	75.22	75.22
13	-65.111437	31.166622	59.248	92.836	157.40	0.6382	1172.47	29.55	127.85	52.15
14	-64.995269	-3.82907	66.190	120.972	12.91	0.5472	847.82	75.26	62.35	62.35
19	-62.676303	115.755281	63.226	113.026	161.16	0.5594	1361.21	169.74	8.58	8.58
24	-59.451267	-32.033322	59.894	83.396	80.08	0.7182	1123.23	153.79	73.71	73.71
22	-59.308225	169.87493	28.950	45.794	177.50	0.6322	766.31	136.03	41.47	41.47
21	-59.021649	93.49632	20.900	31.188	61.93	0.6701	1415.71	172.60	110.67	69.33
25	-58.642768	-169.09763	31.437	47.854	177.33	0.6569	821.99	41.36	135.97	44.03
29	-55.645046	108.933042	35.416	55.682	71.58	0.6360	1405.12	176.18	104.60	75.40
33	-54.258907	90.920482	13.857	34.159	16.51	0.4057	1417.68	175.09	158.58	21.42
31	-54.112972	108.966933	11.141	18.040	68.99	0.6176	1412.96	176.21	107.22	72.78
38	-53.251426	17.407847	84.913	168.851	12.26	0.5029	904.99	27.91	15.65	15.65
36	-52.246727	166.270166	48.250	71.697	77.30	0.6730	844.14	149.84	72.54	72.54
37	-51.899788	157.469691	33.175	50.438	30.54	0.6577	1024.18	155.64	125.10	54.90
39	-50.507046	-41.545175	14.961	32.706	175.63	0.4574	1341.41	167.28	8.35	8.35
40	-49.900522	-0.716172	30.746	45.233	25.17	0.6797	627.15	145.67	120.50	59.50
42	-49.767408	-48.17529	45.685	69.385	172.53	0.6584	1406.20	169.77	2.76	2.76
43	-49.7469	124.00889	56.533	88.495	67.56	0.6388	1433.28	172.82	105.26	74.74
41	-49.547661	165.670785	20.552	45.153	8.28	0.4552	900.82	150.54	142.26	37.74
45	-49.474448	30.156603	40.260	68.844	132.46	0.5848	1187.28	15.05	117.41	62.59
50	-49.019143	40.27841	43.315	91.513	1.91	0.4733	1340.83	8.59	6.68	6.68
49	-48.698798	-124.18151	64.972	102.549	113.85	0.6336	1464.42	178.07	64.22	64.22
47	-48.629039	94.248556	41.851	123.539	108.14	0.3388	1415.34	177.98	69.84	69.84

Object_ID	Latitude	Longitude	Width	Length	Feature_ Orientation	Aspect_ ratio	Sigma1 _max_kPa	Stress_ orientation	Orientation_ Diff_ 0-180	Orientation_ Diff_ 0-90
52	-48.370182	-11.805123	82.821	132.059	97.65	0.6271	886.63	150.78	53.13	53.13
53	-47.415529	-179.41282	22.878	40.068	84.65	0.5710	662.22	147.77	63.12	63.12
56	-47.334919	-108.78107	51.700	81.265	42.93	0.6362	1468.91	172.64	129.71	50.29
55	-46.943796	-81.752782	27.821	60.038	110.00	0.4634	1421.86	179.89	69.89	69.89
60	-44.81662	-41.070507	24.971	46.760	91.67	0.5340	1450.34	170.56	78.89	78.89
62	-43.327185	120.934763	21.634	33.007	58.64	0.6554	1532.48	179.31	120.67	59.33
64	-42.155958	-160.45636	12.286	23.815	158.97	0.5159	1139.68	16.01	142.96	37.04
65	-41.877142	152.372451	23.512	53.731	99.69	0.4376	1335.75	164.44	64.75	64.75
69	-41.68556	55.658001	70.481	102.657	106.38	0.6866	1551.23	178.18	71.80	71.80
67	-41.638313	-137.85812	14.260	34.091	65.67	0.4183	1502.88	3.50	62.17	62.17
70	-40.824666	34.432841	18.132	28.311	170.66	0.6405	1421.59	7.27	163.39	16.61
68	-40.779198	26.916964	10.819	16.856	77.68	0.6419	1302.32	11.47	66.21	66.21
73	-40.276802	20.889857	28.499	43.895	156.82	0.6492	1201.42	14.38	142.44	37.56
78	-38.990585	-101.48841	48.589	68.353	157.61	0.7109	1459.46	172.08	14.47	14.47
79	-38.517664	6.838945	31.743	65.906	119.70	0.4816	996.27	10.92	108.78	71.22
77	-38.397493	69.365775	18.801	34.343	129.61	0.5474	1527.49	171.03	41.42	41.42
80	-38.006371	105.874225	19.065	32.892	92.40	0.5796	1497.71	2.86	89.54	89.54
85	-36.185893	152.051821	42.029	62.227	170.64	0.6754	1495.98	168.17	2.47	2.47
86	-35.600388	160.312432	26.939	47.478	145.59	0.5674	1377.80	162.66	17.07	17.07
87	-35.049847	-119.8033	31.232	51.319	122.20	0.6086	1635.38	175.09	52.89	52.89
88	-34.411817	-100.91371	21.581	33.875	80.09	0.6371	1463.45	172.42	92.33	87.67
93	-34.106272	-129.59841	58.404	115.876	150.58	0.5040	1686.86	176.30	25.72	25.72
95	-33.005988	13.397893	28.763	58.980	4.59	0.4877	1276.46	9.52	4.93	4.93
97	-31.334034	15.154402	10.286	16.389	87.45	0.6276	1354.42	7.12	80.33	80.33
99	-31.237223	47.825827	11.811	22.060	96.26	0.5354	1734.51	178.32	82.06	82.06
103	-31.097981	21.895502	44.443	76.919	158.64	0.5778	1475.58	9.24	149.40	30.60
102	-30.548656	87.606684	24.682	79.239	77.27	0.3115	1413.80	175.15	97.88	82.12
112	-27.586688	-38.383889	26.756	42.259	123.99	0.6331	1854.80	175.39	51.40	51.40

Object_ID	Latitude	Longitude	Width	Length	Feature_ Orientation	Aspect_ ratio	Sigma1 _max_kPa	Stress_ orientation	Orientation_ Diff_ 0-180	Orientation_ Diff_ 0-90
113	-27.40153	28.783739	24.626	43.332	104.29	0.5683	1679.14	5.38	98.91	81.09
114	-26.616174	17.962972	19.461	34.541	72.54	0.5634	1535.86	9.43	63.11	63.11
120	-26.390791	115.877293	64.712	96.936	10.56	0.6676	1737.40	2.38	8.18	8.18
122	-26.237395	-158.09372	74.284	126.174	147.42	0.5887	1616.39	4.46	142.96	37.04
121	-25.533518	102.709966	42.206	63.603	111.40	0.6636	1525.56	0.80	110.60	69.40
128	-24.204656	-16.666418	81.341	117.099	157.70	0.6946	1657.91	163.10	5.40	5.40
126	-24.113395	9.242514	38.763	95.610	42.79	0.4054	1492.85	177.50	134.71	45.29
124	-24.03618	-148.46072	19.296	49.736	168.81	0.3880	1806.04	2.72	166.09	13.91
129	-23.394752	-111.67098	53.551	92.086	157.70	0.5815	1649.81	174.47	16.77	16.77
135	-20.91544	-34.882224	13.668	40.424	91.58	0.3381	1978.83	175.87	84.29	84.29
139	-20.847258	173.368011	28.682	47.993	178.87	0.5976	1608.37	160.86	18.01	18.01
138	-20.684769	154.383613	17.595	40.889	177.10	0.4303	1876.46	170.98	6.12	6.12
140	-20.416133	27.384084	26.535	38.887	4.85	0.6824	1829.96	2.51	2.34	2.34
136	-20.366992	48.228111	8.847	15.062	145.73	0.5874	1931.34	175.68	29.95	29.95
137	-20.358723	35.282361	14.271	21.155	87.03	0.6746	1910.94	178.97	91.94	88.06
141	-19.875877	-160.10602	12.364	29.021	39.35	0.4261	1741.29	6.81	32.54	32.54
142	-19.354329	-82.839184	22.397	39.796	98.60	0.5628	1466.40	0.29	98.31	81.69
143	-19.138054	-2.570692	15.643	27.779	91.53	0.5631	1618.49	159.50	67.97	67.97
147	-18.744617	166.673126	34.870	53.134	175.48	0.6563	1734.38	163.04	12.44	12.44
148	-18.727629	-141.11149	53.275	76.263	108.70	0.6986	1968.34	179.72	71.02	71.02
146	-18.725256	103.816402	21.633	90.097	77.55	0.2401	1575.80	2.34	75.21	75.21
151	-18.687874	157.607356	25.788	93.287	170.86	0.2764	1871.16	170.93	0.07	0.07
153	-18.636734	-150.77126	47.216	112.238	164.01	0.4207	1893.93	0.87	163.14	16.86
150	-18.050878	-0.984925	30.230	47.614	177.84	0.6349	1637.46	155.24	22.60	22.60
154	-17.007716	-27.65534	18.847	33.376	148.28	0.5647	1985.34	173.36	25.08	25.08
152	-16.954711	-170.83566	3.865	6.230	106.26	0.6204	1675.95	177.11	70.85	70.85
157	-16.709487	44.761726	52.256	82.669	111.03	0.6321	1995.34	178.30	67.27	67.27
164	-16.456522	29.669598	58.132	182.800	49.29	0.3180	1933.85	0.11	49.18	49.18

Object_ID	Latitude	Longitude	Width	Length	Feature_ Orientation	Aspect_ ratio	Sigma1 _max_kPa	Stress_ orientation	Orientation_ Diff_ 0-180	Orientation_ Diff_ 0-90
160	-15.212564	-154.5489	5.729	8.820	22.04	0.6495	1906.66	179.96	157.92	22.08
162	-15.182156	62.073829	23.320	34.327	176.00	0.6794	1820.26	174.27	1.73	1.73
161	-14.975802	-32.533089	18.662	26.073	81.66	0.7158	2073.91	175.34	93.68	86.32
165	-14.584694	-167.93493	9.502	14.307	173.91	0.6642	1749.74	4.90	169.01	10.99
166	-14.428669	-1.168678	25.178	39.382	1.18	0.6393	1712.06	153.18	152.00	28.00
168	-13.961422	-21.9784	21.701	38.303	116.52	0.5666	1960.18	171.76	55.24	55.24
177	-13.505202	100.713398	54.772	153.536	42.82	0.3567	1531.73	0.96	41.86	41.86
171	-13.468745	-76.008433	14.162	21.422	175.99	0.6611	1599.00	1.52	174.47	5.53
170	-13.423188	-164.29844	6.743	14.637	13.67	0.4607	1808.74	6.40	7.27	7.27
176	-12.645568	-139.10587	19.593	34.493	96.13	0.5680	2063.58	178.79	82.66	82.66
175	-12.602892	63.22684	12.352	18.453	153.02	0.6694	1811.30	174.63	21.61	21.61
181	-11.548457	150.16401	28.196	39.609	38.13	0.7119	2090.71	176.59	138.46	41.54
186	-11.401202	-128.47856	32.057	57.699	58.51	0.5556	2011.27	176.11	117.60	62.40
185	-11.384235	-158.79322	30.734	88.488	83.15	0.3473	1911.96	3.97	79.18	79.18
188	-10.746304	-176.5578	17.278	42.851	160.65	0.4032	1763.74	144.91	15.74	15.74
196	-9.931846	22.433017	114.788	164.129	81.07	0.6994	1946.39	2.21	78.86	78.86
198	-9.883783	-63.566391	121.078	178.819	102.22	0.6771	1898.43	1.82	100.40	79.60
193	-9.366767	45.145176	61.851	146.331	91.04	0.4227	2077.85	176.93	85.89	85.89
203	-8.844525	134.422005	81.141	115.430	134.08	0.7029	2172.41	179.52	45.44	45.44
195	-8.817794	124.913989	22.529	34.851	162.53	0.6464	2074.66	0.98	161.55	18.45
197	-8.61489	35.189833	27.837	41.033	177.35	0.6784	2087.56	179.39	2.04	2.04
200	-8.54142	-158.01532	27.676	43.513	176.25	0.6360	1957.73	2.65	173.60	6.40
201	-8.347468	-43.975222	34.812	52.527	178.48	0.6627	2185.62	179.79	1.31	1.31
202	-8.253287	25.740339	35.547	59.942	29.72	0.5930	2003.17	179.46	149.74	30.26
199	-8.183727	-151.94615	15.274	30.575	110.17	0.4996	2034.73	1.22	108.95	71.05
208	-7.557891	-85.023217	77.183	128.745	48.14	0.5995	1445.99	0.39	47.75	47.75
207	-7.076856	47.205154	26.499	40.420	8.93	0.6556	2087.28	178.42	169.49	10.51
206	-6.701352	-175.77599	10.646	16.982	149.81	0.6269	1808.09	131.13	18.68	18.68

Object_ID	Latitude	Longitude	Width	Length	Feature_ Orientation	Aspect_ ratio	Sigma1 _max_kPa	Stress_ orientation	Orientation_ Diff_ 0-180	Orientation_ Diff_ 0-90
211	-6.599004	84.069302	64.448	98.109	172.76	0.6569	1431.06	178.44	5.68	5.68
212	-5.950212	169.564074	32.766	51.118	163.21	0.6410	1885.31	169.61	6.40	6.40
214	-5.944004	67.196645	54.926	79.442	90.21	0.6914	1754.37	177.54	87.33	87.33
217	-5.344217	48.17721	18.172	27.613	163.43	0.6581	2090.27	178.54	15.11	15.11
213	-5.312821	-132.03455	6.757	15.671	130.94	0.4312	2093.41	178.99	48.05	48.05
224	-5.165203	115.357576	83.997	148.688	54.76	0.5649	1892.96	0.68	54.08	54.08
219	-4.83283	-153.69094	4.457	9.238	53.31	0.4825	2036.82	179.75	126.44	53.56
220	-4.08711	129.894305	8.710	13.959	34.72	0.6239	2167.04	0.46	34.26	34.26
223	-3.837592	128.148987	9.902	24.834	130.89	0.3987	2141.01	0.17	130.72	49.28
228	-3.617658	-79.433182	76.246	138.018	111.09	0.5524	1541.50	0.19	110.90	69.10
227	-3.58507	154.765114	58.513	91.418	96.97	0.6401	2103.47	178.57	81.60	81.60
226	-3.477165	10.468605	36.860	55.802	112.57	0.6606	1862.54	173.38	60.81	60.81
230	-2.923509	56.312564	37.679	53.603	57.31	0.7029	1989.66	178.72	121.41	58.59
232	-1.65382	23.699168	10.231	14.724	83.91	0.6949	2023.12	0.04	83.87	83.87
236	-1.084843	142.639829	24.113	50.085	158.07	0.4814	2221.48	0.04	158.03	21.97
234	-0.970305	-144.76638	30.331	74.029	121.96	0.4097	2128.85	0.15	121.81	58.19
235	-0.658169	-152.40606	16.864	28.465	142.61	0.5924	2065.00	0.31	142.30	37.70
237	-0.471627	27.324652	22.478	56.100	118.99	0.4007	2060.91	179.89	60.90	60.90
238	0.121995	92.058595	24.552	42.091	69.84	0.5833	1421.41	0.01	69.83	69.83
240	0.371024	16.833039	23.753	56.994	44.84	0.4168	1935.49	179.62	134.78	45.22
243	0.549762	54.478272	83.047	146.243	55.85	0.5679	2023.54	179.96	124.11	55.89
253	1.058495	105.157518	126.649	186.266	50.31	0.6799	1644.52	179.98	129.67	50.33
247	1.212977	-167.61846	63.387	92.814	35.47	0.6829	1885.97	179.52	144.05	35.95
244	1.600511	166.749774	44.186	72.952	97.61	0.6057	1944.08	2.29	95.32	84.68
245	1.832712	37.936068	42.813	85.373	87.00	0.5015	2134.19	0.15	86.85	86.85
246	1.978403	-124.63983	23.119	61.901	114.63	0.3735	2008.32	0.86	113.77	66.23
252	2.835756	82.289044	7.072	28.773	29.17	0.2458	1452.55	0.46	28.71	28.71
249	2.893571	-83.974313	15.739	29.384	87.43	0.5356	1463.63	179.86	92.43	87.57

Object_ID	Latitude	Longitude	Width	Length	Feature_ Orientation	Aspect_ ratio	Sigma1 _max_kPa	Stress_ orientation	Orientation_ Diff_ 0-180	Orientation_ Diff_ 0-90
251	3.015183	175.955355	7.074	18.221	38.84	0.3882	1845.51	14.11	24.73	24.73
254	3.696224	76.656434	12.289	20.748	160.58	0.5923	1543.63	1.11	159.47	20.53
256	4.652292	-61.322491	36.022	62.868	108.29	0.5730	1975.93	179.19	70.90	70.90
258	4.680722	151.102614	29.866	42.702	153.95	0.6994	2151.13	1.95	152.00	28.00
263	5.203063	-135.88034	61.710	96.342	148.54	0.6405	2115.57	1.60	146.94	33.06
262	5.446028	153.677764	39.409	76.330	65.84	0.5163	2112.30	3.02	62.82	62.82
270	6.094475	56.689436	58.396	95.801	7.38	0.6096	1973.70	2.10	5.28	5.28
269	6.236254	-161.88235	55.561	87.953	56.05	0.6317	1929.87	178.52	122.47	57.53
265	6.383795	171.924343	22.280	47.900	58.70	0.4651	1861.14	13.00	45.70	45.70
273	7.004097	-139.38648	72.090	101.506	29.41	0.7102	2113.26	0.92	28.49	28.49
272	7.828128	-146.18414	17.077	26.177	21.69	0.6524	2084.09	0.00	21.69	21.69
271	7.927481	26.146022	5.740	8.121	153.30	0.7068	2011.96	0.41	152.89	27.11
275	8.300384	-70.466006	56.666	80.794	133.66	0.7014	1742.58	178.88	45.22	45.22
286	8.519766	33.307326	90.908	216.581	137.04	0.4197	2075.97	179.38	42.34	42.34
274	8.636329	-124.65566	15.652	22.695	69.06	0.6897	1984.02	2.99	66.07	66.07
277	9.763515	-132.19584	13.818	33.026	36.04	0.4184	2064.39	2.29	33.75	33.75
276	10.013759	11.531932	4.549	6.596	170.05	0.6897	1812.02	174.31	4.26	4.26
279	10.328321	-126.0068	35.639	59.184	132.79	0.6022	1992.26	2.99	129.80	50.20
280	10.338639	-107.02506	51.340	83.574	90.37	0.6143	1610.40	4.14	86.23	86.23
283	10.749842	160.779815	41.364	59.631	5.82	0.6937	1958.23	7.14	1.32	1.32
281	11.274179	38.43006	8.721	14.121	135.22	0.6176	2068.87	2.20	133.02	46.98
287	11.450354	-156.15625	15.971	36.490	174.36	0.4377	1945.89	178.86	4.50	4.50
292	11.963681	-157.43709	48.304	94.811	144.40	0.5095	1921.77	177.57	33.17	33.17
288	12.003816	-151.66345	12.134	20.227	142.00	0.5999	1991.19	178.97	36.97	36.97
289	12.064465	99.446345	30.416	45.794	133.96	0.6642	1511.73	178.97	45.01	45.01
291	12.203126	117.670594	45.502	72.611	89.96	0.6267	1914.48	178.12	88.16	88.16
293	12.92369	-141.76477	51.029	75.125	65.01	0.6793	2044.57	2.74	62.27	62.27
307	13.359827	52.503465	229.922	394.687	47.12	0.5825	1985.82	2.70	44.42	44.42

Object_ID	Latitude	Longitude	Width	Length	Feature_ Orientation	Aspect_ ratio	Sigma1 _max_kPa	Stress_ orientation	Orientation_ Diff_ 0-180	Orientation_ Diff_ 0-90
296	15.499571	-138.85606	8.434	13.626	64.85	0.6190	2021.67	1.97	62.88	62.88
302	15.742698	174.076786	23.144	91.639	137.90	0.2526	1718.33	21.62	116.28	63.72
298	15.938764	47.115552	10.110	25.710	86.91	0.3932	2006.19	2.65	84.26	84.26
300	16.219274	8.471334	34.479	50.461	89.08	0.6833	1685.40	0.95	88.13	88.13
303	16.57747	28.5814	34.050	55.595	127.01	0.6125	1926.55	178.57	51.56	51.56
301	16.586071	-126.57747	13.531	20.552	75.51	0.6584	1940.95	4.11	71.40	71.40
309	18.047922	43.703304	15.126	23.461	84.15	0.6447	1981.67	3.66	80.49	80.49
311	18.365584	57.176189	33.483	168.591	112.31	0.1986	1870.92	3.70	108.61	71.39
310	18.677452	-117.33386	15.244	35.557	179.02	0.4287	1779.10	7.11	171.91	8.09
313	18.820112	-62.861922	52.822	111.100	64.07	0.4754	1838.62	176.62	112.55	67.45
312	19.10482	-21.041948	26.072	49.461	62.52	0.5271	1844.40	10.57	51.95	51.95
319	19.378427	25.943426	86.199	142.731	130.77	0.6039	1837.86	175.81	45.04	45.04
315	19.500466	85.689766	50.350	74.559	113.97	0.6753	1421.26	2.46	111.51	68.49
316	19.722372	-104.97841	43.372	137.487	105.00	0.3155	1551.58	5.62	99.38	80.62
317	19.918923	-131.76603	34.341	54.984	134.45	0.6246	1938.41	4.26	130.19	49.81
320	21.050718	-56.872694	12.130	22.636	91.45	0.5359	1909.33	179.31	87.86	87.86
322	21.525918	-151.34806	37.126	55.349	106.60	0.6708	1819.88	178.76	72.16	72.16
326	21.946762	-75.014095	28.216	40.538	126.57	0.6960	1583.99	177.80	51.23	51.23
321	21.961302	124.892442	4.829	11.466	75.67	0.4212	1924.09	178.24	102.57	77.43
323	22.21666	-47.552047	4.683	10.569	7.00	0.4430	1975.06	0.07	6.93	6.93
325	22.319569	123.905681	7.201	11.801	99.08	0.6102	1903.47	179.93	80.85	80.85
335	22.412685	9.849419	58.243	108.924	164.20	0.5347	1548.31	4.02	160.18	19.82
332	22.451714	140.247339	36.557	53.101	177.10	0.6884	1978.79	3.13	173.97	6.03
329	22.51947	-134.70738	21.300	32.013	48.63	0.6654	1904.23	2.44	46.19	46.19
330	22.735408	-166.18794	14.247	20.581	105.09	0.6922	1580.85	179.03	73.94	73.94
331	22.827267	-165.17024	17.628	30.115	81.41	0.5853	1593.45	171.92	90.51	89.49
333	22.836992	120.019459	43.429	66.549	93.32	0.6526	1849.31	177.86	84.54	84.54
334	23.359223	-117.9063	9.372	17.712	143.28	0.5291	1744.45	8.00	135.28	44.72

Object_ID	Latitude	Longitude	Width	Length	Feature_ Orientation	Aspect_ ratio	Sigma1 _max_kPa	Stress_ orientation	Orientation_ Diff_ 0-180	Orientation_ Diff_ 0-90
338	24.081519	94.20619	24.302	110.939	19.08	0.2191	1431.01	1.09	17.99	17.99
336	24.261326	174.045279	32.854	47.872	107.20	0.6863	1514.85	19.69	87.51	87.51
337	24.634572	24.386414	14.999	31.270	174.07	0.4797	1696.05	173.71	0.36	0.36
340	25.550208	18.312777	21.382	30.309	108.28	0.7055	1578.38	170.83	62.55	62.55
342	25.644295	-165.96613	25.762	55.476	17.08	0.4644	1506.00	170.81	153.73	26.27
343	26.009139	14.908114	36.542	56.428	149.20	0.6476	1516.91	172.00	22.80	22.80
341	26.180663	4.931492	9.024	13.526	120.80	0.6672	1406.83	7.60	113.20	66.80
345	26.883626	-173.92481	11.554	17.226	31.69	0.6707	1387.11	9.89	21.80	21.80
346	27.247561	43.987244	15.804	25.549	172.95	0.6186	1819.86	1.39	171.56	8.44
348	27.695996	-158.0551	36.970	57.692	49.19	0.6408	1568.14	175.79	126.60	53.40
355	29.848889	151.468392	40.899	58.813	36.62	0.6954	1694.98	10.78	25.84	25.84
354	29.934908	115.53112	43.126	77.535	84.48	0.5562	1691.77	177.37	92.89	87.11
357	30.097543	129.400599	29.451	54.609	164.88	0.5393	1814.67	0.90	163.98	16.02
356	30.253369	156.24281	28.422	40.449	20.49	0.7027	1611.52	12.76	7.73	7.73
361	30.431224	-161.2887	38.141	54.686	76.62	0.6975	1442.42	171.59	94.97	85.03
360	30.533007	138.12566	38.892	59.076	74.13	0.6583	1802.52	4.72	69.41	69.41
359	30.801193	-18.483808	25.158	35.797	78.10	0.7028	1498.75	15.22	62.88	62.88
363	31.406234	-115.47056	11.094	37.526	151.76	0.2956	1635.32	7.91	143.85	36.15
362	31.514431	-116.47648	11.334	26.306	166.58	0.4308	1646.09	7.20	159.38	20.62
367	31.64246	-132.13042	109.780	162.986	37.31	0.6736	1727.00	1.73	35.58	35.58
366	32.441987	-100.50066	44.585	90.244	141.83	0.4940	1462.24	7.65	134.18	45.82
369	33.68678	-147.78497	18.483	27.135	1.32	0.6812	1564.84	174.21	172.89	7.11
368	33.760436	-171.03799	5.532	8.867	88.71	0.6239	1186.86	171.53	82.82	82.82
372	34.358012	22.208298	47.575	75.676	169.42	0.6287	1399.93	170.91	1.49	1.49
371	34.442925	-74.591108	9.309	16.986	82.81	0.5480	1516.71	177.05	94.24	85.76
373	35.267732	-154.25904	28.884	43.115	39.83	0.6699	1425.59	171.00	131.17	48.83
376	36.171939	-3.03294	25.190	35.985	2.23	0.7000	1097.85	20.65	18.42	18.42
386	36.820049	53.631142	118.629	178.753	157.10	0.6637	1637.33	3.16	153.94	26.06

Object_ID	Latitude	Longitude	Width	Length	Feature_ Orientation	Aspect_ ratio	Sigma1 _max_kPa	Stress_ orientation	Orientation_ Diff_ 0-180	Orientation_ Diff_ 0-90
382	37.95934	-87.788829	40.665	62.778	97.10	0.6478	1413.47	0.40	96.70	83.30
383	38.052181	109.170318	40.239	80.343	122.32	0.5008	1530.94	179.46	57.14	57.14
381	38.242742	-98.969296	14.441	42.796	70.20	0.3374	1444.60	5.66	64.54	64.54
379	38.350227	-82.947604	6.392	13.015	84.55	0.4912	1432.36	179.30	94.75	85.25
390	40.066546	-74.475677	90.971	159.948	159.14	0.5688	1480.99	0.74	158.40	21.60
391	41.746112	168.547938	63.319	115.192	28.03	0.5497	1051.53	23.36	4.67	4.67
396	42.876459	69.111649	82.240	127.548	11.89	0.6448	1503.75	5.29	6.60	6.60
398	44.324487	-91.452299	58.386	101.864	42.74	0.5732	1414.98	2.57	40.17	40.17
400	46.141729	51.741319	42.476	69.388	127.60	0.6122	1483.65	178.34	50.74	50.74
401	46.7722	-145.62975	36.413	54.491	46.82	0.6682	1298.21	169.18	122.36	57.64
405	48.171784	119.367336	74.684	113.730	101.32	0.6567	1469.53	3.39	97.93	82.07
407	48.503664	-122.99814	63.919	104.129	84.27	0.6138	1464.06	179.47	95.20	84.80
408	48.769761	-156.32652	36.598	60.672	165.13	0.6032	1077.81	161.70	3.43	3.43
406	49.279151	-175.51041	9.596	15.651	111.23	0.6131	648.35	151.81	40.58	40.58
410	49.404816	5.207684	58.479	81.826	146.78	0.7147	677.18	148.79	2.01	2.01
409	50.304101	-48.288109	6.516	20.694	84.44	0.3149	1390.79	10.05	74.39	74.39
414	50.89067	49.410521	136.148	210.569	147.61	0.6466	1410.07	176.18	28.57	28.57
412	51.224858	0.656582	35.824	61.180	137.89	0.5856	561.04	38.86	99.03	80.97
413	52.291656	-81.257137	22.374	32.186	67.50	0.6952	1414.02	5.70	61.80	61.80
415	53.613342	-161.93267	16.107	23.697	9.94	0.6797	917.81	152.73	142.79	37.21
416	53.861734	117.335833	15.990	29.095	171.29	0.5496	1410.20	6.17	165.12	14.88
419	54.478667	74.838025	24.801	45.283	174.70	0.5477	1437.22	6.61	168.09	11.91
418	54.581355	96.556782	10.462	31.027	161.89	0.3372	1413.94	4.08	157.81	22.19
420	54.905659	91.136584	8.723	35.665	29.45	0.2446	1417.60	5.10	24.35	24.35
426	60.75976	-143.81911	28.740	40.018	19.63	0.7182	1204.64	159.76	140.13	39.87
427	61.318583	-120.14868	87.032	185.538	141.75	0.4691	1387.86	177.90	36.15	36.15
428	63.872507	-99.510074	16.778	25.102	39.80	0.6684	1423.69	1.83	37.97	37.97
432	75.512547	66.217645	61.529	98.214	8.10	0.6265	1409.09	173.84	165.74	14.26

Table S2. Measurements and modeled stress orientations for mountains.

Object_ID	Latitude	Longitude	Unit	Width	Length	Feature_ Orientation	Aspect_ ratio	Sigma3 _min_kPa	Stress_ orientation	Orientation_ Diff_ 0-180	Orientation_ Diff_ 0-90
1	-87.277917	-97.210466	Mu	57.823	161.505	65.81	0.3580	-1425.89	175.71	109.90	70.10
2	-85.982101	-30.533408	Ml	69.669	114.227	35.96	0.6099	-1412.47	109.07	73.11	73.11
5	-77.825779	-175.92711	Mu	37.033	59.134	119.67	0.6262	-1287.05	74.11	45.56	45.56
27	-75.560833	116.831098	Ml	93.905	132.223	125.85	0.7102	-1379.75	148.88	23.03	23.03
50	-73.067008	164.576647	Ml	76.648	116.568	134.00	0.6575	-1165.26	100.78	33.22	33.22
54	-70.218736	110.224887	Ml	27.843	120.526	43.48	0.2310	-1383.11	162.36	118.88	61.12
57	-69.781926	-46.77633	Ml	215.121	317.352	85.79	0.6779	-1279.55	146.52	60.73	60.73
59	-66.336279	116.152828	Mm	24.612	30.797	164.79	0.7992	-1357.29	163.36	1.43	1.43
60	-65.440412	-43.181596	Mu	15.092	25.811	127.82	0.5847	-1235.47	154.89	27.07	27.07
61	-65.064174	110.822707	Ml	152.832	269.885	16.72	0.5663	-1376.82	168.43	151.71	28.29
62	-62.386325	56.112817	Ml	38.766	117.459	56.47	0.3300	-1368.73	5.59	50.88	50.88
66	-52.887191	88.088819	Ml	78.996	114.516	106.82	0.6898	-1418.72	172.18	65.36	65.36
74	-50.975658	-31.862596	Ml	180.000	287.506	138.97	0.6261	-1211.35	161.51	22.54	22.54
77	-48.049827	23.870083	Mu	162.800	272.187	45.06	0.5981	-1092.68	18.08	26.98	26.98
80	-45.945236	-23.643547	Ml	154.856	325.767	108.44	0.4754	-1175.99	160.01	51.57	51.57
82	-43.826882	-124.76946	Mm	86.254	196.530	115.44	0.4389	-1527.9	178.67	63.23	63.23
87	-41.794307	102.926623	Ml	150.260	217.165	83.32	0.6919	-1457.35	1.03	82.29	82.29
84	-40.872934	-57.105046	Mu	34.228	61.057	46.83	0.5606	-1582.85	177.68	130.85	49.15
92	-39.588578	75.053626	Ml	113.979	121.866	70.94	0.9353	-1480.06	174.33	103.39	76.61
88	-39.054128	-59.245974	Mu	23.576	30.129	52.38	0.7825	-1606.4	179.33	126.95	53.05
96	-36.37745	158.783621	Ml	76.067	165.435	159.40	0.4598	-1379.66	164.27	4.87	4.87
98	-35.123479	149.917307	Mu	73.747	113.420	173.08	0.6502	-1555.74	167.53	5.55	5.55
106	-32.18964	121.28307	Mu	111.821	138.945	25.84	0.8048	-1715.04	2.16	23.68	23.68
105	-31.043197	41.803524	Mu	44.897	65.417	115.55	0.6863	-1722.37	0.15	115.40	64.60
113	-28.218323	-160.56631	Ml	178.841	419.458	108.09	0.4264	-1526.11	7.69	100.40	79.60
110	-28.061475	-125.20142	Mu	109.832	137.705	113.43	0.7976	-1769.5	176.52	63.09	63.09
108	-27.837429	124.30211	Mu	74.556	80.778	16.74	0.9230	-1816.34	0.09	16.65	16.65
112	-27.827152	-30.079933	Mu	75.358	137.642	1.78	0.5475	-1769.53	170.93	169.15	10.85
115	-26.15179	-68.651171	Mu	61.414	118.338	120.15	0.5190	-1669.01	1.94	118.21	61.79
111	-25.950282	105.690512	Mu	10.700	28.792	63.04	0.3716	-1574.31	2.2	60.84	60.84
114	-25.91865	-44.074109	Mu	50.263	84.164	8.97	0.5972	-1914.31	177.25	168.28	11.72

Object_ID	Latitude	Longitude	Unit	Width	Length	Feature_ Orientation	Aspect_ ratio	Sigma3 _min_kPa	Stress_ orientation	Orientation_ Diff_ 0-180	Orientation_ Diff_ 0-90
134	-24.602588	161.993174	Ml	232.375	559.815	50.88	0.4151	-1665.37	164.86	113.98	66.02
126	-24.317444	-63.040011	Mu	48.307	178.915	166.59	0.2700	-1780.87	1.46	165.13	14.87
119	-24.18946	-170.90172	Mu	67.932	116.064	38.73	0.5853	-1493.42	177.86	139.13	40.87
123	-23.670873	-24.874322	Mu	97.987	114.948	49.90	0.8524	-1803.44	169.36	119.46	60.54
118	-23.642895	123.835318	Mu	27.393	73.010	88.22	0.3752	-1878.99	0.35	87.87	87.87
125	-23.173613	65.708666	Ml	59.983	159.750	68.96	0.3755	-1695.5	172.88	103.92	76.08
129	-21.927414	102.695685	Ml	200.788	210.712	169.86	0.9529	-1538.48	3.17	166.69	13.31
128	-21.206764	-93.149674	Mu	82.729	228.927	128.11	0.3614	-1416.09	176.89	48.78	48.78
130	-21.028127	-109.76347	Ml	124.007	292.145	86.13	0.4245	-1632.83	173.98	87.85	87.85
131	-19.598405	109.732172	Mu	45.327	58.702	61.14	0.7721	-1690.47	2.32	58.82	58.82
135	-17.599956	-11.565914	Mu	37.909	48.613	96.66	0.7798	-1742.3	163.89	67.23	67.23
136	-17.37471	-60.919309	Mu	163.054	260.743	59.48	0.6253	-1898.52	2.06	57.42	57.42
137	-16.680064	-120.7051	Mu	206.188	280.423	21.30	0.7353	-1860.44	175.56	154.26	25.74
145	-12.297048	-71.059327	Mm	142.146	191.617	53.53	0.7418	-1715.73	1.54	51.99	51.99
141	-12.293985	-56.26449	Mu	62.232	106.454	52.08	0.5846	-2027.71	1.38	50.70	50.70
139	-11.997776	-14.7906	Mu	22.205	42.538	152.56	0.5220	-1881	167.51	14.95	14.95
143	-10.812529	-73.311124	Mm	17.055	112.262	58.75	0.1519	-1664.61	1.87	56.88	56.88
146	-10.671398	-134.35864	Mu	110.319	114.180	55.70	0.9662	-2067.81	178.78	123.08	56.92
149	-10.034371	-112.79976	Mu	95.388	213.162	80.81	0.4475	-1743.31	176.39	95.58	84.42
144	-9.52939	-81.590312	Mu	25.695	33.876	85.93	0.7585	-1493.58	0.99	84.94	84.94
153	-8.983535	87.874369	Ml	138.412	164.117	152.76	0.8434	-1407.51	178.41	25.65	25.65
152	-7.778459	114.661354	Ml	138.884	199.483	129.23	0.6962	-1869.88	1.08	128.15	51.85
155	-7.685305	-79.093804	Ml	69.509	199.181	159.27	0.3490	-1544.21	0.43	158.84	21.16
150	-7.113739	81.806797	Mm	14.149	23.376	72.88	0.6053	-1456.68	178.65	105.77	74.23
156	-5.363601	83.185547	Ml	2.499	6.606	36.51	0.3783	-1442.43	178.81	142.30	37.70
157	-5.324012	81.291998	Ml	91.067	120.706	62.82	0.7545	-1461.42	179.02	116.20	63.80
160	-4.700823	-63.371225	Ml	156.973	294.456	174.98	0.5331	-1926.02	0.78	174.20	5.80
159	-2.849875	90.901766	Ml	86.924	167.273	32.00	0.5197	-1412.22	179.68	147.68	32.32
162	-1.87784	96.278951	Ml	126.892	198.264	5.60	0.6400	-1467.44	0.1	5.50	5.50
163	-1.871644	-82.045847	Ml	126.306	286.006	21.10	0.4416	-1488.33	179.97	158.87	21.13
170	-1.215364	41.780744	Ml	176.558	444.143	169.65	0.3975	-2138	179.6	9.95	9.95

Object_ID	Latitude	Longitude	Unit	Width	Length	Feature_ Orientation	Aspect_ ratio	Sigma3 _min_kPa	Stress_ orientation	Orientation_ Diff_ 0-180	Orientation_ Diff_ 0-90
166	1.293893	12.897031	Mu	66.938	109.159	64.91	0.6132	-1893.21	179.25	114.34	65.66
169	2.05134	18.491594	Mu	107.111	178.653	179.20	0.5995	-1958.02	179.31	0.11	0.11
171	4.06007	144.303844	Mu	112.856	166.598	158.06	0.6774	-2210.7	0.96	157.10	22.90
172	6.937492	75.658564	Mm	59.316	70.730	28.42	0.8386	-1563.48	2.01	26.41	26.41
176	8.418486	98.127024	Mm	110.388	159.672	3.01	0.6913	-1488.41	179.09	176.08	3.92
178	9.079844	123.780575	Ml	118.813	190.443	151.29	0.6239	-2054.74	179.01	27.72	27.72
175	9.326025	146.840481	Mu	36.550	64.793	162.33	0.5641	-2154.42	2.9	159.43	20.57
177	11.26787	145.606425	Mu	26.096	30.138	176.47	0.8659	-2142.66	2.83	173.64	6.36
179	13.063242	144.310864	Mu	25.260	31.811	131.78	0.7941	-2125.14	2.52	129.26	50.74
181	13.346676	127.548699	Mu	33.887	88.218	12.38	0.3841	-2071.44	179.88	167.50	12.50
182	13.70007	-85.232255	Mu	89.712	247.719	48.07	0.3622	-1439.13	179.15	131.08	48.92
189	14.792054	-104.19375	Ml	152.784	293.962	4.16	0.5197	-1548.66	4.63	0.47	0.47
183	14.829658	-3.543404	Mu	85.524	140.387	97.09	0.6092	-1712.54	20.15	76.94	76.94
184	15.13985	28.141935	Mu	54.278	120.648	122.57	0.4499	-1946.31	178.25	55.68	55.68
188	15.31172	-127.65724	Mu	98.019	311.297	129.04	0.3149	-1964.7	3.32	125.72	54.28
190	16.143775	-67.235588	Ml	62.777	220.438	8.75	0.2848	-1778.43	177.25	168.50	11.50
191	17.53993	-44.893626	Mu	84.226	165.940	52.50	0.5076	-2066.06	1.39	51.11	51.11
187	17.920998	-55.526618	Mu	27.244	43.622	3.84	0.6245	-1972.84	178.06	174.22	5.78
192	18.6057	-89.202318	Ml	106.013	216.328	90.66	0.4901	-1413.17	1.92	88.74	88.74
197	21.893857	-48.31506	Mu	41.641	120.137	35.48	0.3466	-1975.99	179.6	144.12	35.88
202	22.226491	-67.104496	Ml	100.048	210.085	15.37	0.4762	-1728.81	176.46	161.09	18.91
201	22.384759	170.454432	Mu	39.630	202.058	155.74	0.1961	-1607.8	19.49	136.25	43.75
195	22.532651	-152.1196	Mu	15.420	19.441	68.90	0.7931	-1788.26	177.91	109.01	70.99
199	23.59903	-61.033652	Mu	65.956	141.405	123.56	0.4664	-1817	176.97	53.41	53.41
200	24.117644	92.638653	Mu	67.317	82.349	9.37	0.8175	-1421.95	0.45	8.92	8.92
203	25.306045	-83.646579	Mu	60.433	81.289	56.02	0.7434	-1448.63	179.2	123.18	56.82
207	25.980398	-98.78906	Ml	193.167	231.853	16.60	0.8331	-1453.19	4.2	12.40	12.40
208	26.381293	-126.4554	Mu	150.841	280.768	160.82	0.5372	-1803.46	5.77	155.05	24.95
210	30.374911	-32.389148	Mu	110.313	152.764	142.21	0.7221	-1714.79	9.7	132.51	47.49
212	31.095898	-7.146403	Mu	84.470	198.268	30.30	0.4260	-1319.21	21.68	8.62	8.62
211	32.505871	-163.00354	Mu	40.879	69.748	150.50	0.5861	-1352.2	169.42	18.92	18.92

Object_ID	Latitude	Longitude	Unit	Width	Length	Feature_ Orientation	Aspect_ ratio	Sigma3 _min_kPa	Stress_ orientation	Orientation_ Diff_ 0-180	Orientation_ Diff_ 0-90
215	34.345837	-73.072534	Ml	86.630	232.612	156.63	0.3724	-1536.03	178	21.37	21.37
213	34.556872	-31.593972	Mu	51.931	92.677	168.36	0.5603	-1594.58	11	157.36	22.64
216	37.57308	-10.797783	Mu	71.475	80.350	151.03	0.8896	-1158.21	20.48	130.55	49.45
218	39.002247	-40.802468	Mu	20.268	62.372	15.36	0.3250	-1572.23	6.05	9.31	9.31
222	39.145137	-2.829072	Mu	114.522	197.543	56.83	0.5797	-991.197	25.64	31.19	31.19
220	39.636815	-93.931092	Mu	36.130	72.866	162.99	0.4958	-1422.02	5	157.99	22.01
219	39.674745	-70.235895	Mu	45.582	70.427	156.13	0.6472	-1518.85	179.72	23.59	23.59
224	40.474614	-80.454714	Mu	101.496	273.820	57.53	0.3707	-1442.45	0.91	56.62	56.62
225	42.596013	-57.041199	Mu	98.172	240.664	146.63	0.4079	-1548.43	2.27	144.36	35.64
228	46.407312	-126.32459	Ml	121.814	217.072	77.93	0.5612	-1483.11	0.18	77.75	77.75
230	47.225103	-160.9805	Mu	51.778	117.188	174.70	0.4418	-1006.8	160.17	14.53	14.53
233	48.380564	-62.220793	Mu	75.386	192.898	13.17	0.3908	-1460.75	1.98	11.19	11.19
232	48.725058	-164.35781	Ml	70.862	118.424	9.22	0.5984	-909.11	156.63	147.41	32.59
234	49.579721	110.447471	Mu	126.669	166.827	132.08	0.7593	-1442.16	0.34	131.74	48.26
235	52.859776	152.949143	Mu	87.135	148.540	75.86	0.5866	-1105.39	23.29	52.57	52.57
237	54.455927	-119.9176	Mu	45.396	108.130	11.33	0.4198	-1421.74	178.22	166.89	13.11
238	55.117864	24.42664	Mu	54.220	122.612	139.03	0.4422	-1046.66	155.66	16.63	16.63
239	57.766158	106.522028	Ml	72.568	168.942	148.26	0.4295	-1402.4	7.18	141.08	38.92
240	59.170781	161.524448	Mu	105.203	161.017	64.92	0.6534	-919.506	35.71	29.21	29.21
241	60.389262	36.097892	Mu	12.314	66.095	162.88	0.1863	-1210.64	159.6	3.28	3.28
244	63.240548	-61.4958	Mu	131.523	205.638	176.95	0.6396	-1349.52	12.82	164.13	15.87
242	64.942543	-175.161	Mu	28.457	58.942	1.21	0.4828	-896.104	119.41	118.20	61.80
246	69.497049	-49.680481	Mu	71.465	210.255	36.52	0.3399	-1292.24	30.58	5.94	5.94
245	69.958937	-37.12435	Mu	60.114	144.221	172.54	0.4168	-1215.62	43.02	129.52	50.48
247	71.422318	40.517687	Mu	111.594	153.613	163.18	0.7265	-1306.34	154.26	8.92	8.92
249	74.124424	72.209129	Mu	97.214	197.559	17.09	0.4921	-1416.35	173.92	156.83	23.17
248	74.141548	158.9575	Mu	30.723	76.613	125.47	0.4010	-1210.96	66.61	58.86	58.86

C h a p t e r 3

MOUNTAIN DEGRADATION MECHANISMS ON IO REVEALED BY GEOLOGIC MAPPING OF THE COCYCTUS MONTES REGION FROM JUNOCAM IMAGERY

C. H. Seeger[1], K. de Kleer[1], D. A. Williams[2], J. E. Perry[3], A. G. Davies[4], and D. M. Nelson[2]

"There's something ever egotistical in mountain-tops and towers, and all other grand and lofty things; look here,—three peaks as proud as Lucifer…This round gold is but the image of the rounder globe, which, like a magician's glass, to each and every man in turn but mirrors back his own mysterious self."

Moby Dick, Chapter 99: The Doubloon

Abstract

Periodic high-resolution documentation of Io is essential to understanding its surface evolution, from volcanic eruptions to tectonic motion to large scale mass wasting. *Juno* flybys of Io in 2023 and 2024 obtained imagery of the surface with the JunoCam imager at spatial resolutions comparable with those from the *Galileo* spacecraft (1996-2001). Areas of Io's north polar region were imaged for the first time, revealing high mountains in low phase angle observations. We are unable to identify detailed changes on mountain features due to the limited overlap and complementary nature of the high-resolution coverage between the *Galileo* and *Juno* datasets. However, the improved lighting conditions in the

[1]Division of Geological and Planetary Sciences, California Institute of Technology, Pasadena, CA 91125, USA.
[2]School of Earth and Space Exploration, Arizona State University, Tempe, AZ 85287, USA.
[3]Lunar and Planetary Laboratory, University of Arizona, 1541 East University Boulevard, Tucson, AZ 85721, USA.
[4]Jet Propulsion Laboratory, California Institute of Technology, 4800 Oak Grove Drive, Pasadena, CA 91109, USA.

JunoCam imagery allow us to refine our understanding of previously mapped features, including an extension of the rifting relationships previously proposed at Shamshu Patera. Cocytus Montes, a trio of mountains newly identified in the north polar region, exhibit several different geologic units grading from sharp features to eroded hummocks along their slopes. We present a geologic map of this region, and examine the interplay between the mountain units and the underlying layered plains which connect them on a raised plateau. Unique blocky deposits strewn across the plateau between these units have sparse analogs elsewhere on Io, and prompt questions about the erosional mechanisms acting on Io that may have emplaced them. We propose several formation mechanisms and conclude that some may be possible, but regolith creep-modified cliff collapse may be the most likely.

Plain Language Summary

Jupiter's innermost large moon Io is the most volcanically active body in the solar system, with a surface that is continually modified by eruptions (lava flows and gaseous plumes) and tectonics (fault motion and erosion via events like landslides). The Juno spacecraft made close approaches to Io in 2023 and 2024, obtaining images of the surface at high resolution and low sun angle--conditions which produce the long shadows necessary to see Io's topography. Though the new images do not overlap with the high-resolution images obtained 20 years prior by the Galileo spacecraft, they do capture parts of the north pole region in detail for the first time. We closely examined the northern region to create a geologic map, highlighting the different volcanic, mountain, and plains units visible here. We present several possible formation mechanisms for a newly defined geologic unit (a blocky deposit made of kilometer-scale chunks of crustal material), favoring a cliff-collapse mechanism above the others. We also identify several localities where sharper, less eroded mountain types gradually transition into slumped and eroded mountain types, capturing intermediate stages of erosion not typically visible on Io, with implications for the overall pace and process of erosion on a very active surface.

1. Introduction

Io is a world of constant, widespread volcanic activity (e.g., Davies, 2007). Io's volcanism is driven by an eccentric orbit forced by resonance with Europa and Ganymede (Peale et al., 1979). The resulting tidal stresses melt the interior enough to produce frequent and often voluminous volcanic eruptions, resurfacing the moon at a rate of ~ 0.1-1 cm year^{-1} (Carr et al., 1998; Geissler et al., 2004; Johnson et al., 1979). Basaltic to possibly ultramafic lavas, interlayered with sulfur-rich deposits and sulfur dioxide frost, are compressed continuously driving deep crustal subsidence stresses from crustal recycling (e.g., McEwen et al., 2004; McKinnon et al., 2001; Schenk & Bulmer 1998). These subsidence stresses may be relieved by intense faulting in all directions in the subsurface, uplifting large blocks of crust up to 16 kilometers high into towering mountains (Schenk et al., 2001). Io's crust is estimated to be 13-30 kilometers thick in order to support such large structures (Jaeger et al, 2003; Kirchoff & McKinnon, 2009; Schenk et al., 2001). Ionian mountains, while tectonic, differ from terrestrial mountains in that they are not long mountain ranges formed by plate movements, but rather form in tall, isolated massifs, usually elongate in nature, formed by subsidence stresses (Williams et al., 2011).

Io's extrusive volcanism (see summary in Davies, 2007 and Lopes et al., 2023) manifests as the emplacement of lava flows, both within paterae (caldera-like structures that are ubiquitous on Io) and on the extra-paterae plains, and as lava lakes in at least a few of the paterae. Gases exsolving from magma as it ascends, and released as a result of thermal interaction between lava flows and frozen sulfurous compounds on the surface, drive plume activity. The thermal emission from Io's volcanoes is so great that it is easily detectable from spacecraft and from telescopes on Earth (e.g., Davies et al., 2001; 2010; 2024; de Kleer et al., 2019; de Pater, et al., 2017; Lopes et al., 2001; McEwen et al., 1998; Perry et al., 2024; Veeder et al., 1994). The mechanisms for Io's volcanic eruptions are not entirely understood, but hypothesized models include magma, originating in the asthenosphere or from a magma ocean, feeding localized shallow magma chambers (Davies et al., 2006) and other crustal intrusions (Spencer et al., 2020). The magma then may exploit the tectonically fractured

subsurface to rise along fault conduits (Jaeger et al., 2003; Keszthelyi et al., 2004). Alternatively, hot spot-type magma ascension through crustal weaknesses in a heat-pipe regime (e.g., Kirchoff & McKinnon, 2009; McKinnon et al., 2001; O'Reilly & Davies, 1981) may feed volcanic eruptions. Analysis of *Galileo* and *Juno* data flyby show Io does not have a global magma ocean (Park et al., 2024), suggesting that a preponderance of magma originates in the asthenosphere.

Volcanic and tectonic forces work in tandem to both construct and destroy the iconic surface features distributed across Io's surface. Mountains, plateaus, and patera-bounding scarps all exhibit some form of degradation, likely triggered by a combination of gravity, volatile cycling, and volcanically-induced seismicity. These processes have previously been explored using imagery from the *Voyager* and *Galileo* spacecrafts, with *Galileo* providing high resolution (10s to 100s of meters/pixel) coverage of select regions (Keszthelyi et al., 2001; Turtle et al., 2004). Moore et al. (2001) detail the possible erosion mechanisms acting on scarps categorized in high-resolution *Galileo* imagery as belonging to four distinct classes: unmodified, alcoved, terraced, and containing basal debris cones. Scarp formation and modification or retreat could be attributed to liquid SO_2 sapping, plastic deformation and glacial flow of interstitial volatiles, sublimation-degradation, or disaggregation from chemical decomposition of solid S_2O (McCauley et al., 1979; Moore et al., 2001). However, the simplest and perhaps most universal mechanism is dry mass-wasting in the form of block release and brittle slope failure (Moore et al., 2001). Brittle failure on a much larger scale—10s of kilometers across—also likely modified the 10.5 km tall Euboea Montes, where large plates can be seen breaking with downslope movement in addition to more hummocky debris lobes (Schenk & Bulmer, 1998).

Previous studies have cataloged changes visible on Io's dynamic surface captured in the 17 years between the *Voyager* (1979) and *Galileo* (1995-2003) explorations of Io, and even over the course of each mission (Geissler et al., 1999, 2004; Keszthelyi et al., 2001; McEwen & Soderblom, 1983; McEwen et al., 1998; Turtle et al., 2004). In the intervening years, Earth-based telescopes and the *New Horizons* spacecraft (which performed an Io flyby in 2007)

have provided additional evidence of active volcanism and, therefore, inferred surface modification (e.g., de Kleer et al., 2019a; de Pater et al., 2017; Rathburn et al., 2014). Now, 20 years after the *Galileo* mission concluded, the Juno spacecraft has obtained new high resolution images of Io with JunoCam, a "push-broom" visual-light imager, on two close flybys: PJ57 on December 30, 2023 and PJ58 on February 3, 2024. These images have a best resolution of 1.8 km/pixel (Ravine et al., 2024) and capture the north polar region of Io in unprecedented detail—including several mountains that were previously unidentifiable. The coverage of this new dataset is largely complementary to the highest resolution regions captured by *Galileo*, though there is some overlap in the PJ58 Jupitershine images; for example, the closely studied Hi'iaka Montes region appears along the limb in the Jupitershine image.

In this study, we use the higher resolution and favorable solar incidence angle (long shadows near the terminator are essential in distinguishing Io's topography) in the JunoCam dataset to provide a new perspective on previously mapped units, sharpening our understanding of mountains and paterae. We present several updates to the global database of surface features identifiable with this new perspective, and use the new imagery to expand on the sequence of rift events previously proposed for the Shamshu region. Finally, we present a regional geologic map of the northern mountains. These edifices, while morphologically consistent with their lower-latitude counterparts, exhibit a range of degradational styles and capture surface evolution in progress. We explore five possible formation mechanisms for a unique blocky deposit associate with these mountains, allowing us to expand on the possible erosional mechanisms modifying Io's surface features.

2 Methods

2.1 Global Relationships

All mapping and feature/imagery analysis was based on previous mapping efforts; namely, the USGS Geologic Map of Io based on mosaiced global imagery from the *Galileo* and *Voyager* spacecraft flybys (Williams et al., 2011). This map contains shapefiles denoting the

geologic units mappable at the global 1 km/pixel resolution, including paterae, mountains, and plains (subdivided into several morphotypes). Using ESRI ArcGIS Pro™ software, a new mosaicked basemap of Io using imagery from the PJ57 and PJ58 JunoCam flybys was projected into the same simple cylindrical coordinate plane for direct comparison between the new and old data. Variable lighting conditions between the new JunoCam images taken at different times of day from *Galileo* and *Voyager* images, along with differences in resolution of the coverage, give us new perspective on the surface features—namely, mountains and paterae—that have been previously mapped. A low incidence angle is often required to distinguish topographic relief in Io's mountains (e.g., Schenk et al., 2001; Turtle et al., 2001; Jaeger et al., 2003).

A systematic, side-by-side comparison was performed for all identifiable mountains visible in JunoCam imagery between the new and prior basemap. The focus of this mapping comparison was to identify surface features that may have changed (e.g., mass wasting deposits, changes in shape to paterae, newly uplifted scarps, etc.), or to note features that remained the same throughout the 20-year time gap in the imagery. Because the JunoCam PJ57 imagery has a maximum resolution of 1.84 km/pixel, detectable changes were limited to large-scale changes to overall feature shape; textural evolution of individual slopes, while likely over this time interval, is beyond the limitation of this dataset. However, the new perspectives on several previously-mapped surface features with updated resolution and lighting conditions allowed us to suggest several updates to the database of previously mapped features, where a mapped patera now clearly stands up in positive relief, or the shape of a mountain is better defined (Figure 1).

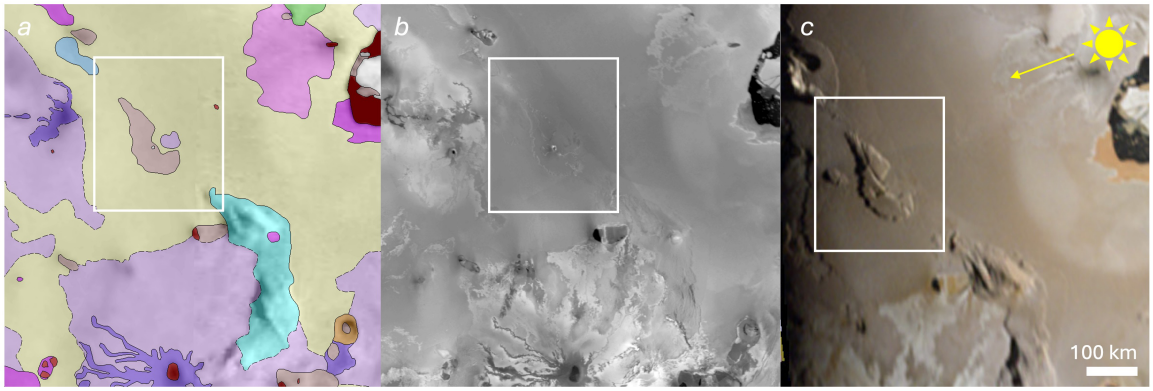

Figure 1. Near-terminator illumination conditions provide new perspective on a feature adjacent to Loki Patera that was originally mapped as a patera in (a) the USGS Geologic Map of Io (Williams et al., 2011) using (b) high sun angle imagery from *Galileo* and *Voyager*, but is evident as a topographic high and should be reclassified as a mountain based on (c) JunoCam PJ57 coverage of this same area. Images are centered at 6° N, 36° E; north is up .

2.1 Northern Regional Map

The JunoCam imagery provides new images of the previously unresolved north pole region of Io, from 55˚ latitude northward. Previous features were inferred from *Galileo* and *Voyager* coverage, but new polar mountains and paterae can now be mapped for the first time (Williams et al., 2024). Using ArcGIS Pro™ and a basemap with an orthographic projection centered at 60N 330W to minimize distortion, we created a regional map at 1:500,000 scale of the new mountainous region of interest for this study, using geologic units and symbology consistent with those presented in Williams et al. (2011) as well as previous local geologic mapping efforts of a comparable scale (Bunte et al., 2008, 2010; Leone et al., 2009; Williams et al., 2002, 2004, 2005, 2007). Units are defined and classified based on morphology, albedo, and color, and depositional, erosional, and evolutionary sequence is inferred based on superposition and cross-cutting relationships between units.

One of the most distinguishing features in the northern region is the large scattered blocks of rock distributed across the layered plains between the northwestern and northeastern mountains. Using the orthographic projection centered among these mountains, ArcPro was

used to measure the size of the blocks (as best as they can be distinguished from shadow, at just a few pixels wide) and distance from the top of the nearest peak (as best as could be distinguished, as the mountain summit falls along the terminator). The USGS's Integrated Software for Imagers and Spectrometers (ISIS; Rodriguez, 2024) qview program was used with the EDR dataset to measure block height (as well as scarp heights) using processed individual .cub frames derived from a JunoCam processing pipeline (Perry et al., 2024, following Perry et al., 2022). The Red filter observation was favored due to its higher signal-to-noise than the Green and Blue bands. Measurements were made using the red filter individual framelet (JNCE_2023364_57C00022_V01_RED_0013) to calculate the size of each shadow thrown from the blocks. These measurements were combined with solar incidence angle to calculate block height using Equation 1, with a 1 pixel error on line length measurements.

Shadow Geometry Equation *(1)*

Height = Shadow Length * tan (180 – Sun Azimuth in degrees)

3 Results

3.1 Insights from Junocam Imagery

3.1.1 Search for Temporal Changes in Io's Surface

Direct side-by-side comparisons of the same geographical regions covered by *Voyager*, *Galileo*, and new JunoCam imagery taken under different solar incidence angle conditions illuminate changes and consistencies in Io's topography over the approximately 45-year time interval spanned by these datasets. Io is a dynamic body with frequent volcanic eruptions and evidence of erosional processes such as mass wasting and scarp retreat via sapping (e.g., Moore et al., 2001). Therefore, identifying surface changes such as large-scale mountain shape alteration due to mass wasting would place constraints on the erosion rates degrading

Io's tall topography. In all surveyed mountains (due to JunoCam imagery covering ~50% of the global *Galileo*/*Voyager* coverage), there were no discernable changes in shape and no identifiable debris fans or changes in scarp sharpness from the twenty-year-old dataset to today's. Even mountains proximal to active, erupting paterae remained unchanged in appearance at the JunoCam pixel scale of 1.8 km. We also do not see any evidence of tectonic motion indicative of reactivation (extension) along compression fault lines. That is not to say surface modification did not occur—it is extremely likely that many steep mountain slopes have new landslides, textural changes, and debris fans—but any such evidence would require data with a higher spatial resolution.

A few regions exhibit putative changes at the limit of image resolution. These are presented in Supplementary Figure 1. Future higher resolution imagery of these regions could confirm the extent of alteration and place constraints on rates of erosional processes.

3.1.2 Feature Reclassification

JunoCam imagery provides new perspectives on several previously-mapped and classified mountains and paterae due to improved resolution and solar incidence angle. We provide a catalog of locations where the new view on published USGS geologic units (Williams et al., 2011) calls for a reclassification of features (Table 1; Supplementary Figure 2). Dominantly, we suggest updates to mountain extent and mapped paterae that are now discernable as positive relief mountain features. While there are 10 features that were identified for reclassification based on a global survey, these updates could be significant in future studies that survey the number and location of tectonic and volcanic features, as well as their shapes and relationships to each other.

Table 1. Reclassified geologic units based on JunoCam imagery. Object ID corresponds to published Geologic Units in USGS Geologic ArcGIS map file (Williams et al., 2011). Longitudes are given in 0-180° format, East positive. Corresponding images are given in Supplementary Figure 2.

Object ID	Latitude	Longitude	Name	Previous Classification	New Classification	Rationale
879	8.52	33.31		Patera floor, undivided	Mountain	Better lighting shows positive relief
941	15.13	27.85		Bright plains	Layered Plains	Better lighting shows previously unmapped layered plains unit
1415	57.50	106.60	Nile Montes	Mountain, lineated	Mountain, lineated	New perspective on shape
1365	50.20	110.80	Nile Montes	Flows, dark; Flows, undivided	Mountain, lineated	Flows reinterpreted as slumping mountain material
1420	59.20	164.00		Flows, undivided	Layered Plains	Flows reinterpreted as lower layered plain component of pleateau mountain
1345	47.00	162.00		Flows, bright	Mountain, undivided	Better lighting highlights scarps, better defining mountain
1380	53.61	161.93		Patera floor, undivided	Mountain, undivided	Better lighting shows positive relief
213	46.85	10.36		Flows, undivided; Red-brown plains	Patera floor, dark; Patera floor, undivided	New imagery reveals unmapped patera
695	-8.0949	114.5406	Pillan Mons	Patera floor, undivided	Layered Plains	Better lighting shows positive relief
438	-26.271	16.18887		Red-brown plains; Bright plains	Layered Plains	Layered plains continue to edge of patera; uplift potentially post-dates lava flow

3.1.3 A More Detailed Look at the Shamshu Region

Previous studies have examined closely the region surrounding Shamshu Mons (Bunte et al., 2010). West Shamshu Mons and Shamshu Patera are covered in 340–345 m/pixel detail in one *Galileo* SSI observation obtained during the orbit I27 flyby (I27ISSHMSHU01; PIA02555), along with small corners of what Bunte et al. (2010) have informally classified as North and South Shamshu Montes, which are otherwise barely discernable in the low-resolution *Galileo* coverage (Figure 2). The JunoCam PJ58 flyby coverage of this same region in 1.01 km/pixel detail using Jupitershine illumination provides a new, complete view of these two mountains in unprecedented detail. The overall structure of South Shamshu Mons is a lineated mountain with mottled material to the west, and an adjacent connected lobe to the east. This adjacent lobe lacks discernable features in the JunoCam imagery, but has two scarps illuminated in the *Galileo* imagery that led to its previous classification as its own independent undivided mountain. The Shamshu region is located ~370 km east of the distinctive Hi'iaka Montes region (measured From Hi'iaka Patera to Shamshu Patera), where

two large, L-shaped mountains are interpreted to have been rifted apart by translational and extensional tectonics (Bunte et al., 2010; Jaeger et al., 2003). Based on the available *Galileo* data at the time, Bunte et al. (2010) propose a similar regime for the Shamshu region.

The updated view of North and South Shamshu Montes provided by JunoCam allows us to develop this model. Both North and South Shamshu Montes are large edifices (over 150 km across) with multiple morphologies expressed, but distinct parallel ridges at the ends closest to Shamshu Patera. The similarities between these ridges support the interpretation that these edifices could have once been joined, formed by an earlier compressive uplift episode, with the new larger view of the extent of the ridges leading us to suggest a slight modification to the Bunte et al. (2010) reconstruction (Figure 3). A NE/SW oriented right lateral strike-slip fault with an accommodating extensional rift where Shamshu Patera opens could easily restore North and South Shamshu Montes to one morphologically consistent edifice. A perpendicular extensional rift at the location of Shamshu Patera would provide accommodation space for lava buildup from successive eruptions, with the darkest, freshest lava concentrated at the NE end of the patera, adjacent to the eroding scarp of North Shamshu Mons, where the rift would be opening. Though Shamshu Patera cuts into the flank of North Shamshu Mons, the lack of debris on the patera floor in the *Galileo* imagery suggests that later-stage volcanic resurfacing could have obscured fallen debris from mountain degradation (Bunte et al., 2010; Turtle et al., 2001). JunoCam imagery similarly does not contain any resolvable debris cones or major scarp retreat, indicating this to be a stable process over the twenty-year gap between datasets—unsurprising for such a short interval in geologic time. West Shamshu Mons could also have been part of a singular mountain complex; though it is not morphologically consistent with the parallel ridges of North and South Shamshu Montes, it does have demonstrate some similarities in orientation to the eastern lobe of South Shamshu Mons, indicating that they both could have been formed by similar uplift regimes. However, West Shamshu Mons sits 80 km west of Shamshu Patera, and there is no resolvable evidence for long-term rifting transporting it westward; older lava flows associated with this rifting could have degraded beyond recognition at the current

resolution, or West Shamshu Mons formed independently from the North-South Shamshu complex.

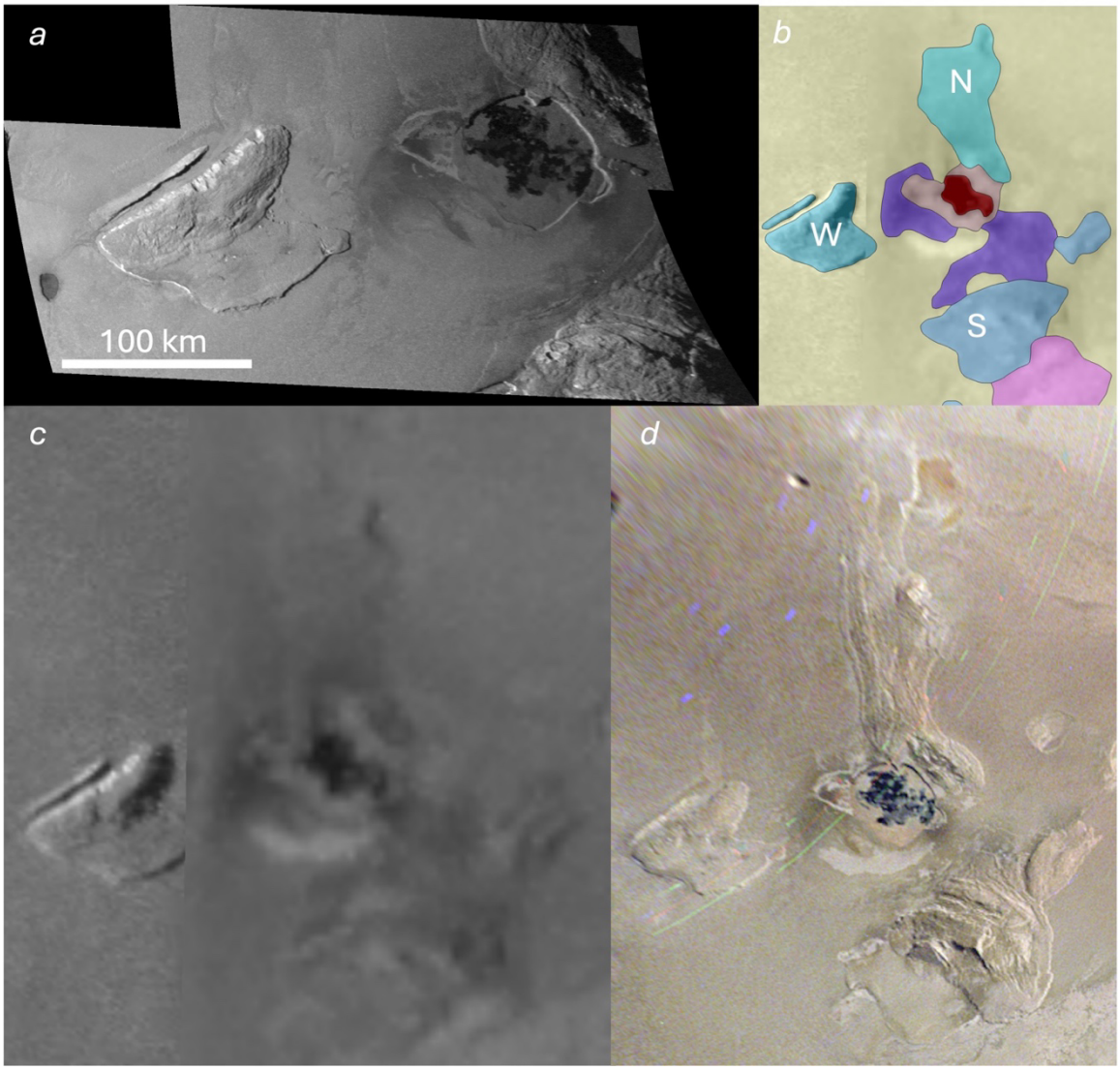

Figure 2. Image coverage and interpretations of Shamshu region of Io, including Shamshu Montes and Shamshu Patera. (a) *Galileo* high resolution image (I27ISSHMSHU01, 340-345 m/pixel), with image centered at 11° S, 68° W; (b) global geologic map of the three mountain units and Shamshu Patera (Williams et al., 2011); (c) *Galileo* low resolution coverage (frames 5 and 6 in global USGS map, corresponding to observation/image numbers C9ISSRFMON01/ 0401785378 and C10ISIOTOPO02/ 0413659700); (d) JunoCam PJ58 Jupitershine image (JNCE_2024034_58C00024_V01) capturing the mountains north and south of Shamshu Patera for the first time in their entirety.

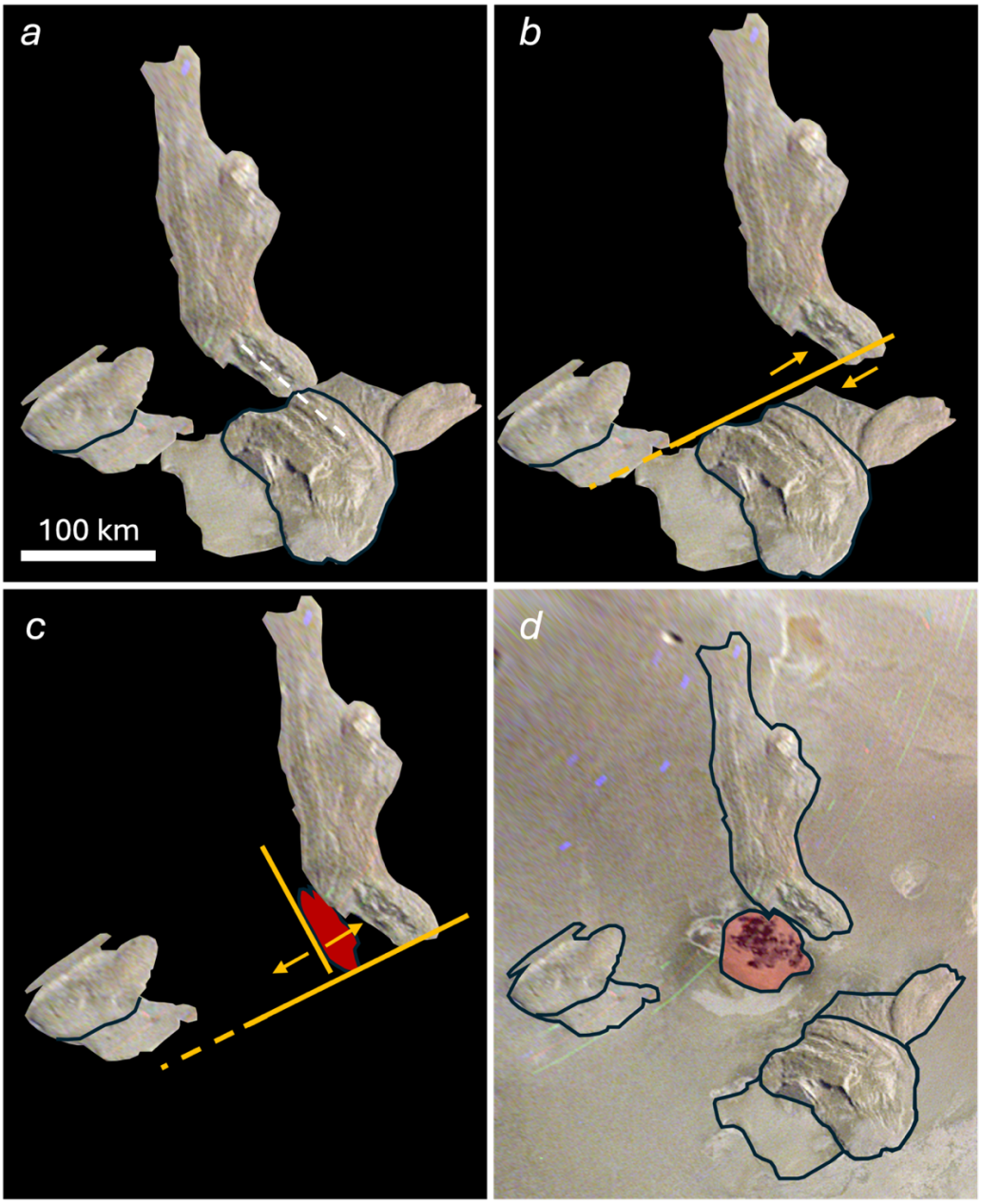

Figure 3. Reconstruction of possible tectonic history in Shamshu region, modified after Bunte et al. (2010) Figure 12. (a) North and South Shamshu Montes are initially one related edifice with aligned linear ridges (dashed white line) while the morphologically similar layered plains on West and South Shamshu Montes are continuous; (b) Right lateral rifting initiates, separating North and South Shamshu Mons; (c) initiation of the Shamshu Patera formation via a rift to accommodate the strike-slip motion of the primary fault while continued extension further separates the mountains; (d) current configuration, with Shamshu Patera siting between the three mountain units.

3.2 Geologic Map of Cocytus Montes

JunoCam coverage during PJ57 provided novel views of Io's northern polar region, including several mountains imaged at 1.84 km/pixel. The low solar incidence angle—approximately 10 degrees, adjacent to the terminator—highlights the topography in sharp relief. We use this new imagery to map five broad geologic units, following conventions employed in the previous suite of regional geologic maps produced from *Galileo* data (Bunte et al., 2008, 2010; Leone et al., 2009; Williams et al., 2002, 2004, 2005, 2007): mountain materials (including plateaus), plains materials, volcanic materials (including paterae and lava flows), bright diffuse deposits, and a newly-defined unit of blocky material. Symbology for units, structural features, and contacts follows the symbology presented in the USGS global geologic map of Io, and we refer the reader Williams et al. (2011) for detailed unit descriptions and interpretations. Here, we highlight the relevant units as summarized in Table 2, along with their interpreted relationships to each other as derived from the regional geologic map (Figure 4).

The northern mountains express the same morphologies as their more equatorial counterparts, with a mix of lineated and mottled units (Williams et al., 2024; Ravine et al., 2024). The area of focus for this regional geologic map is defined by a three-mountain system, Cocytus Montes, with three tall (several km) peaks connected by a system of apron-like layered plains, some of which are uplifted as 1-3 km tall plateaus. The morphology of lineated mountains adjacent to plateau-like layered plains is similar to mountains like West Shamshu Mons, Gish Bar Mons, and several others. However, a new geologic unit of blocky material—composed of kilometer-scale blocks scattered across the layered plains adjacent to the northwestern mountain—has been identified as a unique deposit type not previously recognized on Io. We explore possible formation mechanisms for these blocks in Section 4.1. In addition, scarps along plateau margins, and the blocky region in particular, are closely associated with halo-shaped white diffuse deposits interpreted to be SO_2 sapping at retreating scarps (Moore et al., 2001).

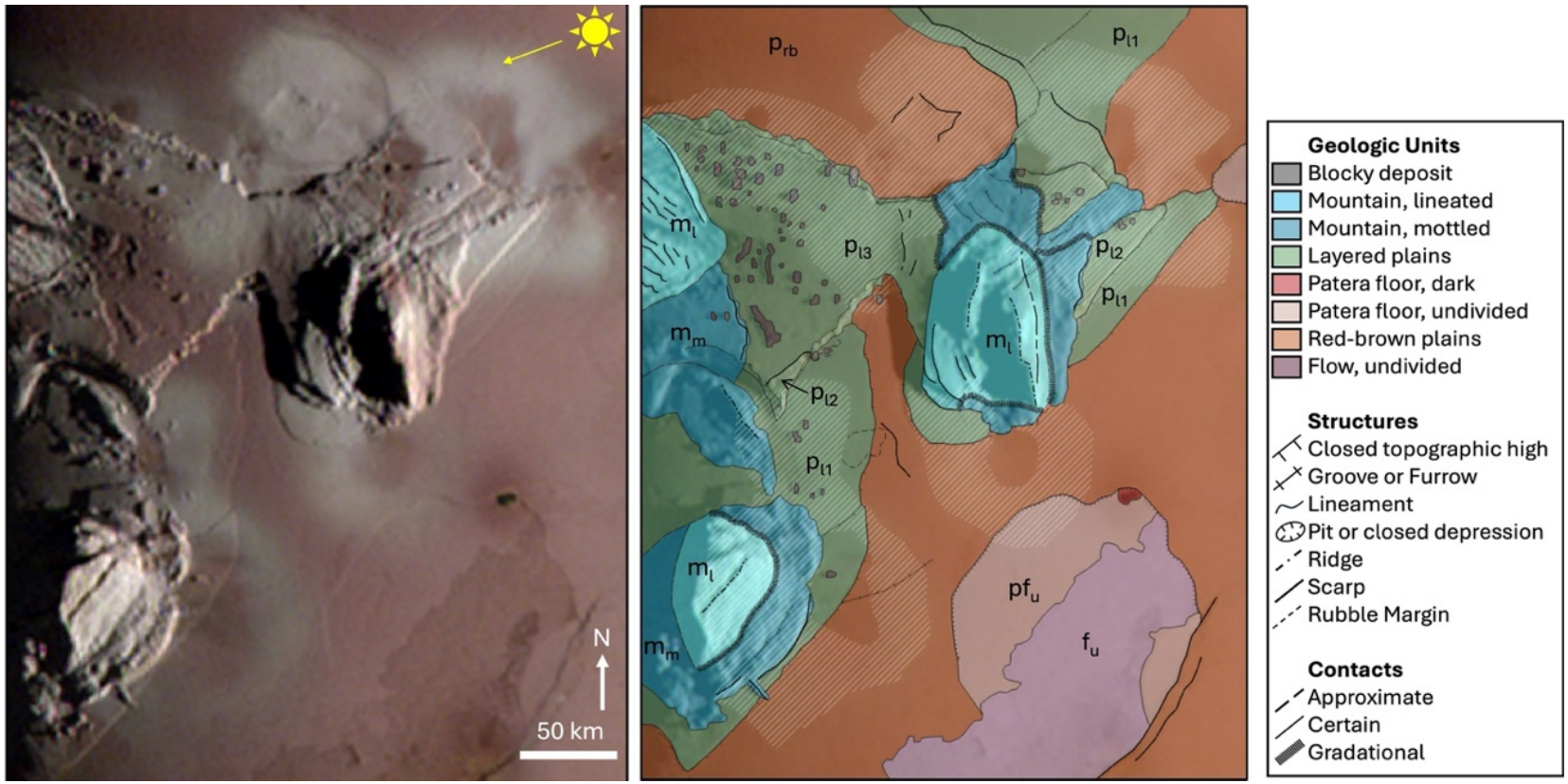

Figure 4. Regional geologic map of Cocytus Montes (composed of West, East, and South Cocytus Mons) using orthographic projection centered on 60N 330W (left). Geologic units (right) are consistent with global geologic units presented in Williams et al. (2011), with an additional blocky deposit unit newly identified and defined here. The reader is referred to full unit descriptions in Table 2 for unit abbreviations shown on map. Map covers 52.3-66.6° N, 11.2-39.2° W.

Table 2. Geologic units identified in northern regional geologic map.

Material Units	Description	Interpretation
Lineated mountain material (ml)	Contains the sharpest scarps, deep shadows cast by prominent ridges, and relatively smooth and sheer faces. Can contain many blocks of uplifted, subparallel plate-type material, and sometimes exhibit lineations on the steep, sheer faces.	Uplifted crustal blocks exhibiting minimial degradation or erosion by downslope slumping or mass wasting. Parallel lineations on the northwestern mountain face may indicate some slumping, although they are not quite parallel to the scarp boundary at the lineated mountain/layered plains contact; similar lineated textures observed on other mountains generally form perpendicular to the slope.
Mottled mountain material (mm)	Characterized by domical mounds of material with few scarps and ill-defined lineations. This unit does contain isolated grooves or furrows, and lobes of material extend out upon underlying plains material.	Material displaced by gravity in a downslope direction, by mechanisms such as mass wasting with or without rotational sliding.
Red-brown plains material (prb)	The interstitial material blanketing the surface between the topographically distinct tectonic and volcanic features.	While Io's surface boasts three colorful plains units on a global scale (yellow, white, and red-brown; Williams et al., 2011), the only morphology present in this mapping area is red-brown, interpreted to be the product of alteration of surficial frosty sulfur compounds by radiation exposure (Johnson, 1997; Geissler et al., 1999).
Layered plains material (pl)	Isolated regions of relatively smooth plains material that are separated from the underlying plains (and each other) by distinct bounding scarps. Several layers are defined (pl1-3), creating large, apron-like plateaus surrounding and even connecting the northeast and northwest mountains.	Silicate crust mantled by sulfur-rich materials exposed on local topographic highs with boundaries defined by degradational processes.
Blocky deposit	Isolated ~2-10 kilometer-wide massifs identifiable by slight albedo/color differences from the underlying plains and measurable shadows. Largest population sits atop a plateau, though several blocks are measured directly adjacent to plateau-bounding scarps.	Blocks of silicate crust originating from mountains or layered plains and deposited by erosional mechanisms across and adjacent to layered plains units.
Diffuse deposit	White material that occurs in characteristic circular to irregular patches, most often along scarp edges, that lightly mantles all underlying units including red-brown plains, layered plains, and mottled and lineated mountainsides.	Volcanic deposits consisting of dust and condensed sulfur dioxide gas (Carlson et al., 1997).
Dark patera floor material (pfd)	Dark material that is uniformly black in color at the image resolution, round in shape and filling topographic depressions, and is aligned at the edge of the curved patera-bounding scarp separating this feature from the red-brown plains.	Warm, recently-emplaced silicate flows or crusted lava lakes (Lopes et al., 2001; Davies et al., 2001; Radebaugh et al., 2001, 2004).
Undivided patera floor material (pfu)	Neither bright nor dark in color or albedo, and is only separated from the plains by the patera-bounding scarp. Mapped unit is overlain by undivided flow.	Crusted and cooled lava flow or lava lake, older than dark patera floor material.
Undivided flows (fu)	Intermediate relative albedo and limited texture at the map resolution. Bounded on the east by scarps, and continues to the south potentially beyond the patera walls.	Lava flows of indetermninate composition, though likely mafic flows originating from patera but mantled by sulfur-rich materials.

3.2.1 Mountain units: gradational contacts linking mountain morphologies

The mapped mountain units are subdivided into lineated mountains, mottled mountains, and layered plains, with several tall (3-5 km lower limit, based on shadow measurements) isolated peaks extending above the surrounding plains, separated by well-defined bounding scarps. While gradational contacts have been identified between mountain units and layered plains elsewhere on Io, this mapped region contains gradational contacts between lineated mountains and mottled mountain material as well. Lineated mountains are interpreted to be the most pristine mountain type, formed tectonically by faulting, uplift, and the subsequent collapse of tall edifices (Schenk and Bulmer, 1998; Turtle et al., 2001, 2004). Mottled mountains are interpreted to be the degraded counterparts of lineated mountains that have undergone mass-wasting processes (Turtle et al., 2001). Previous coarser scale studies (e.g. Crown et al., 1992; Williams et al., 2011), characterize the mountains as being one of these two mountain types. However, we determine two of the three mountains in our study area to capture an intermediary stage of degradation: the uppermost flanks of the mountain retain the sharp scarps of lineated mountains, but there are several areas where hummocky material related to slope failure appears to extend downslope onto the layered plains and bright plains below.

3.2.2 Layered plains: identification of blocky deposits

While some of the lowest-lying plateau-like layered plains units (p_{l1}) do not stand tall above the surrounding plains, the unit that extends between the lineated mountains (p_{l3}) is characterized by tall, sharp bounding scarps, possibly scalloped in places, with some adjacent large blocks and smaller scale rubble piles. Cliff tops are mapped as closed topographic highs, while geologic unit boundaries include the furthest extent of rubble extending below the scarp top. The western portion of this plateau also contains the majority of the scattered blocks (see Section 3.2.3 Blocky Deposits). Shadow measurements from the eastern portion indicate a gently sloping (~3% grade) surface, from 2.93 +/- 0.23 km down to 1.57 +/- 0.29 km over a span of 50 km. A subtle furrowed texture including some mapped lineations across this surface could be a potential expression of downslope creeping processes akin to

terrestrial soil ripples or lunar "elephant hide" texture, though on the kilometer scale rather than centimeter to decameter scale on Earth or the Moon (Anderson & Anderson, 2010; Highland & Bobrowsky, 2008; Lindsay, 1976; Melosh, 2010). While illumination conditions do not permit equal quality measurements of the western portion of this unit, a minimum height estimate of 3.32 +/- 0.3 km indicates that this portion slopes eastward to meet the layered plains of the northeast mountain.

Layered plains have been interpreted to be the result of tectonic activity and/or downslope slumping and mass wasting, possibly from adjacent mountains, with scarps modified by slumping or SO_2 sapping, among other processes (e.g., Moore et al., 2001; Turtle et al., 2001). In the case of similar morphologies to the mapped mountains, such as West Shamshu Mons, the analogous plateau portion of the mountain may have formed from large-scale gravitational sliding of a detached upper layer, composed of lava flows, that was not cohesive with the full tilted crustal block during uplift (Bunte et al., 2010), as opposed to a large-scale mass-wasting formation (*sensu* Schenk and Bulmer, 1998). Our mapped layered plains' relationship to the blocky deposits adjacent to scarp edges may also indicate a large-scale rotational cliff failure erosional mechanism, as explored in Section 4.1.

3.2.3 Blocky Deposits: a key to erosional processes

There are 58 blocks identifiable in the study region, and 41 of these are distributed across the two layered plains unit (p_{l3}) adjacent to the northwest mountain (Figure 4). The remaining smaller populations of blocks are distributed across layered plains adjacent to the other two mountains, and several blocks are identified at the lower boundary of the layered plains, at the base of the scarp. Blocks are considered measurable if they are greater than two pixels across, there is a distinct color or albedo difference to differentiate them from the surrounding plains, and they cast a measurable shadow; JunoCam imagery covers these blocks very close to the terminator, providing the necessary illumination conditions to see these unique features. It should be noted that there are likely blocks smaller than is resolvable, and the angularity and distribution of the blocks may be affected by the pixel scale. Block heights

measured from shadow lengths (Equation 1) indicate that these blocks are wider than they are tall by a ratio of ~6.5:1 on average. That is, they are shaped more like thick slabs than cubes, with diameters of several kilometers. These block dimensions may have implications for formation of this unit, as explored in Section 4. Their distribution across the plateau is irregular, and there are no correlations between block size and distance from the adjacent mountain summit (inferred to be along the terminator), though the largest blocks, which are elongate features somewhat parallel to the adjacent scarp boundaries, are closer to said respective scarps (Figure 5).

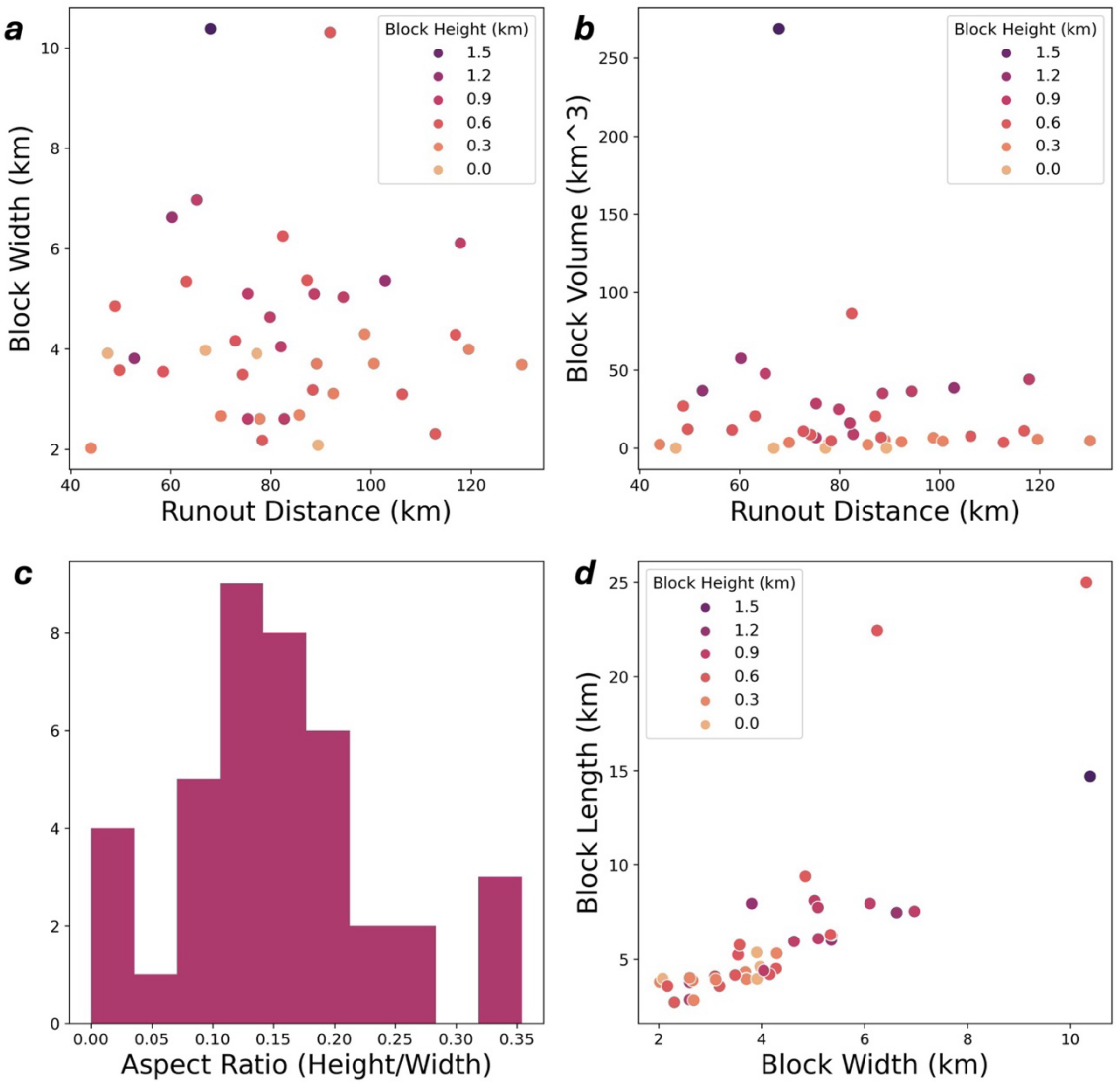

Figure 5. Size and distance parameters for 41 measured blocks on plateau in mapped area. Dataset includes the three long, more sinuous blocks mapped on p_{13}, which correspond to the three largest data points. Block width and length are geodesic measurements of the planform long and short axes. (a) Block size vs. runout distance from the nearest measurable mountain "summit," measured with block width representing the intermediate axis; (b) block size vs. runout distance, measured with calculated volume; (c) distribution of aspect ratios for all measured blocks using width as intermediate axis; (d) a linear relationship between block width and block length. Block height measurements have an error of 1 pixel, corresponding to 0.25 km.

The northern blocky deposit is a new feature type, now identifiable because of the resolution and low sun angle captured by JunoCam. Similar mountain-adjacent layered plains were inspected for similar features, and several potential isolated blocks were detected on the flanks of West Shamshu Mons; these blocks were not previously identified in close regional studies of the Shamshu region (e.g., Bunte et al., 2010), but we are now able to locate them by using the northern blocky deposit as a reference (Figure 6a). This example serves as the closest analog to the blocky deposit, because the two groups of blocks (yellow circle and black arrows) lie atop their respective plateaus of layered plains (which are interpreted to be an erosional deposit from the adjacent mottled mountain material), just as the Cocytus Montes blocks do. There are also several instances of layered plains apparently degrading into large blocks, both in the northern region and across Io (Figure 6b-g). It is not currently clear if the layered plains degradation blocks are formed by the same processes as the plateau-topping blocks, as discussed in Section 4, but they are included for completeness. These secondary examples all occur at the scarp boundary where layered plains or mottled material transitions to basal plains.

Interestingly, all of these alternate block locations are devoid of the halos of white diffuse deposits so common in the northern map region. Some of the plateau-topping blocks sit within a white diffuse halo zone, while some do not. Some of the scarp-adjacent blocks sit within white diffuse halos, while some do not (Figure 4). It is possible the release of SO2 gas from scarp walls, if that is indeed the source of the white diffuse deposits, could contribute to scarp failure in the form of large blocky debris, but these results are inconclusive.

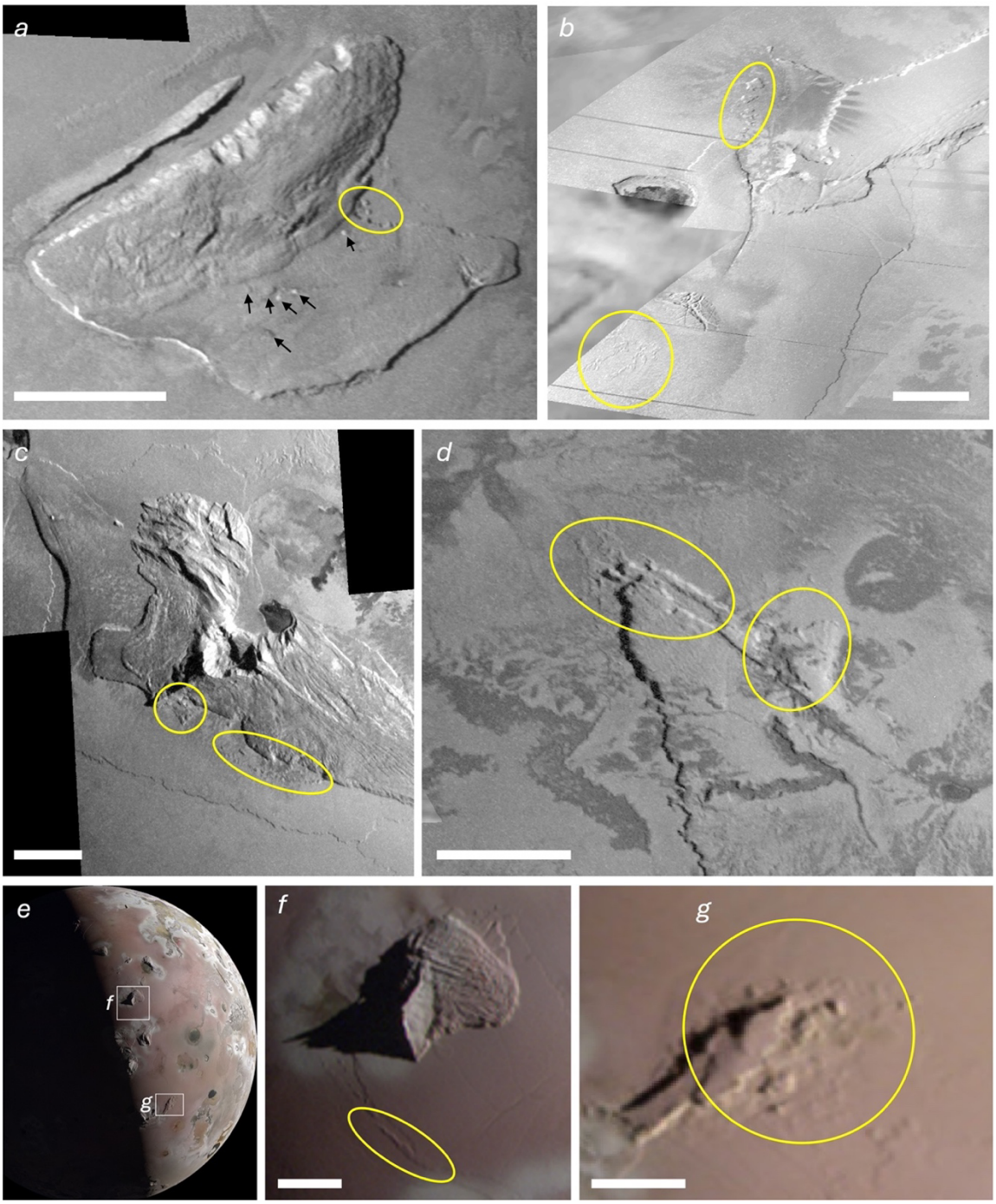

Figure 6. Detections of large blocky debris adjacent to mountains on Io and sitting atop layered plains or red-brown plains. Images captured by *Galileo* (a-d) and JunoCam PJ57 (e-g). Scale bar in all images is 50 km. Image centers are located at: (a) 11° S, 72° W; (b) 37° N, 84° W; (c) 28° S, 161° W; (d) 31° N, 162° W; (f) 43° N, 37° E; (g) 69° N, 37° E.

3.2.4 Diffuse deposits: constraints on scarp retreat

Elsewhere on Io, white diffuse deposits are interpreted to be the products of vaporization, condensation, and reaccumulation of SO_2 (and contaminants) around flow margins (Kieffer et al., 2000; Milazzo et al., 2001). The white diffuse deposits association with scarps—particularly bounding layered plains—and the lack of proximal vents or flows indicates these deposits might rather be the result of seepage from fractures (McCauley et al., 1979). Their relationship to the underlying units is not entirely clear in this locality. Diffuse deposits of the other colors visible on Io (Williams et al., 2011) are not present in the mapped region.

Across Io, diffuse deposits are ephemeral features that easily evolve or become overprinted (Carlson et al., 1997; Douté et al., 2001; Geissler et al, 1999). While cataloging the changes to diffuse deposits between the *Galileo*/*Voyager* and JunoCam datasets is outside the scope of this surface feature-focused study, we do note consistencies in the similarly scarp-adjacent white diffuse deposits in the Euboea Fluctus region (outside the regional map extent), suggesting that these jets are sustained over the 44 year time interval without producing measurable scarp retreat (Figure 7). Pixel sizes in this region are 848 m/pixel, and scarp retreat would need to occur over several pixels to cause a detectable change in the surface expression of the shape of the scarp. Therefore, we can place a bound on the rate of this erosional mechanism, where scarp retreat is happening slower than ~200 m/year. While this is an unreasonably fast rate on geologic timescales, it is nonetheless a useful constraint for erosional models on a highly active surface provided by the given datasets.

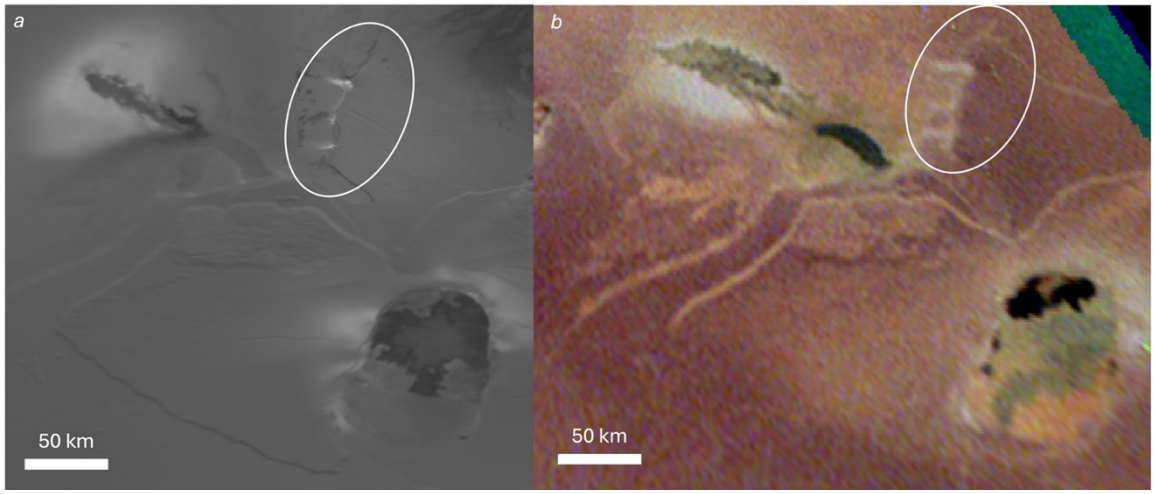

Figure 7. White diffuse deposits at scarp edge in Euboea Fluctus region does not appear to have changed in 44 year time interval between (a) *Voyager* 1 image and (b) JunoCam PJ58 Jupitershine image (JNCE_2024034_58C00025_V01). Images centered at 48° S, 14° E.

4 Discussion

The updated view of Io's surface, with favorable lighting geometry and resolution provided by Junocam imagery allows us to make more nuanced interpretations about the erosional processes acting on Io, informed by our terrestrial understanding of geomorphology and application to other worlds with higher resolution observations, like the Moon and Mars.

4.1 Contacts and Erosional Relationships from New Mapping Efforts

The new perspectives on Io's topography and geologic units afforded by the JunoCam imagery allow us to better constrain the relationships between mountain units, lava flows, and the surrounding plains. Though there have been many eruptions recorded on Io in the twenty years since Galileo captured imagery of Io's surface, there are no dramatic changes in shape to mountain slopes discernable in the JunoCam coverage. However, future imaging campaigns with a greater spatial overlap between high resolution datasets would be instrumental in better constraining the timing and dominant mechanisms of erosion on Io.

The favorable lighting conditions and northern polar region coverage by JunoCam does allow us to update previous classifications of some mountains and paterae, improving our understanding of global relationships between surface features.

Jupitershine imagery of the Shamshu region provides new perspectives on a fascinating mountain-patera system that contains multiple mountain morphologies and clues to the tectonic progression that created the modern landscape. The now complete images of North and South Shamshu Mons in particular invite speculation about the timing of mountain formation and degradation. South and West Shamshu Montes have morphologically similar aprons of layered plains material, but if these were once one consistent plateau (like that in the North polar region), then they had to form before the large-scale rifting that created the modern configuration. If the layered plains formed from slope failure later, it is possible they formed at similar geologic times in order to create plains of similar degradation states. Furthermore, the blocky deposits visible on West Shamshu Mons' flanks indicate yet another later episode of degradation.

In the northern region, the mapped contacts between geologic units include certain and approximate contacts (where shadows or resolution limitations require the geometry of the contact to be inferred), as well as gradational contacts where the boundary between two units is transitional. This convention follows Williams et al. (2011), which notes that the contacts between lineated mountains or mottled mountains can be gradational with layered plains. In the northern map presented here, gradational contacts occur instead between lineated and mottled mountains. Globally, Io's mountains are characterized as either lineated or mottled, with some implications for level of degradation increasing with the mottled morphotype (Williams et al., 2011). While other regional studies do subdivide mountains (e.g., Bunte et al., 2008, 2010; Williams et al., 2004), the northern mountains capture in new detail the transition between these two phases. For both the northeast and southwest mountains, there are clear lobes of hummocky debris released downslope from the smooth ridges above, mapped as mottled mountain material. These hummocky lobes may eventually smooth out

into layered plains material via diffusive processes, but we cannot be certain of this progression.

Ultimately, the superposition of the blocky deposit and mottled material atop layered plains, and the gradational transition between lineated and mottled mountain material, capture several stages of the depositional and erosional processes acting at different times across Io's surface.

4.2 Northern Block Formation

Because the blocky deposit of the northern mapping region is so distinctive, and contains such numerous blocks atop a >1 kilometer tall sloped plateau, it is worth exploring in more detail their possible formation mechanisms. Previous work detailing erosional processes on Io, particularly relating to mass wasting, do not entirely capture the morphology of the remaining material that is visible in the blocky deposit. For example, Schenk and Bulmer (1998) and Moore et al. (2001) discuss both large-scale landslides modifying mountainsides and smaller-scale basal debris cones from scarp retreat, but neither process results in the formation of kilometer-scale blocks. Here, we present several possible mechanisms to produce the observed feature morphology.

4.2.1 Erosional Remnant

In the mapped region, as well as elsewhere on Io, layered plains—consistent with their name—can occur as large slabs layered on top of each other, exposing multiple generations of material (see units p_{L1} vs. p_{L2}, Figure 4). Moore et al. (2001) and Schenk and Bulmer (1998) offer two possibilities for mountain-adjacent plateaus with lobate margins: they could be landslide deposits, or they could be formed from the uplift and lateral compression of a weak underlying surface layer. Given the height of the connected northern plateaus (>1km) and their outward sloping surfaces, the landslide interpretation may be more likely. However they formed, the margins of the layered plains units are eroding back, possibly via the debris

cone and scalloped headwall processes defined by Moore et al. (2001). The slab-shaped proportions of the individual mesas of the blocky unit, as well as the elongate shape of the three largest blocks (with the long axis oriented nearly parallel to the adjacent scarp) could be consistent with a 0.5-1 km thick layered plains unit that has eroded away, leaving some of these blocks behind, in a process akin to the allochthonous sandstone boulders perched atop a plateau in the tableland of the Stołowe Mountains, Poland (e.g., Migoń & Parzóch, 2021). The mountain unit directly adjacent to the blocky deposit is mapped as mottled due to the presence of hummocky material closest to the proximal lineated mountain, but it also appears to have a uniform thickness (as estimated by the consistently illuminated bounding scarp on the east) and areas of smooth surface similar to the layered plains unit below. There are two blocks on top of this unit—perhaps a remnant of yet another plains layer—but the majority of the blocky deposit could be sourced from this plains unit.

If these blocks are erosional remnants, two questions must be raised: why were these blocks left behind, and where did the eroded material go? Differential erosion to leave the blocks behind as a lag would require some heterogeneity within the layered plains. There is nothing in their size, shape, distribution, or albedo to inform what those heterogeneities may be, though compositional differences—including interlayered SO_2 frost—would be the most likely source of strength differences. To interrogate material transport on Io, we must consider the relationship between the blocks and the underlying gently sloping plains. The existing body of literature pertaining to the process of creep on Io is concerned with viscous creep or relaxation within Io's crust (e.g., McKinnon et al., 2001; Ojakangas & Stevenson, 1986). Here, however, we must explore the slow, steady downslope movement of regolith via creep, modeled after diffusive hillslope processes on Earth. Io's surface, composed of lava flows, crustal blocks, and a thin mantling of SO_2 frost, is generally modeled as a solid. It is likely that the combination of volcanically-induced seismicity, chemical (and physical) interactions between condensing and sublimating frost, and bombardment from micrometeorites and volcanic byproducts, could contribute to rock weathering into regolith material, as it has been shown to do on Earth, Mars, and the Moon (Fassett & Thomson, 2014; Gilbert, 1909; Mantovani et al., 2014; Perron et al., 2003; Rapp, 1960; Xiao et al.

(2013)) . If Io's plateaus are blanketed by even a thin layer of regolith (centimeters thick), and their surfaces are sloped >0 degrees, then they offer a mechanism to slowly translate plateau material downslope over geologic time to be eventually recycled by lava flows on the red-brown plains. Therefore, creep processes acting on Io's ~1.5 degree sloped plateau is a viable mechanism to erode the layered plains material away around the blocky deposit.

We also consider if regolith material could be transported away by wind. McDonald et al. (2022) propose a mechanism for aeolian sediment transport driven by sublimation vapor flows due to lava-SO_2 frost interactions, but the distance of the plateaus from the nearest lava flow would make it difficult for material up on the plateau to be affected by sustained winds under Io's sparse atmosphere.

4.2.2 Rockfall

The proximity of the blocky deposit to the lineated mountain material of West Cocytus Mons introduces the possibility that blocks are the product of rockfall, where large pieces of crust, triggered by gravity or seismic activity, broke up and tumbled down the more steeply sloping edifice to scatter across the gently sloping plateau surface. Dry rockfall is widely recognized as a mechanism for landscape evolution across the solar system, even on slopes below the angle of repose, from the Moon to Mars to Mercury (Beer et al., 2024; Cardenas et al., 2025; Conway et al., 2019; Fassett et al., 2017; Kokelaar et al., 2017). To investigate this possibility, we consider only the 41 blocks adjacent to the lineated mountain. Boulders and cobbles produced by rockfall on Earth are irregular, angular, and often characterized as polyhedral in shape, as they have had limited interactions for rounding (such as in fluvial transport) (e.g., Bonneau et al., 2019; Leine et al., 2014). Higher resolution coverage of this area would assist in characterizing the shape of Io's blocks; though they appear to have an angular shape in plan view, many blocks are only a few pixels in size, and therefore it is impossible to accurately determine the angularity (Figure 4). Terrestrial rockfall deposits can contain rocks with equant or cubic to elongate or platy shapes, determined by factors like rock type, fracture patterns, and weathering (e.g., Bonneau et al., 2019; Blott & Pye, 2008).

The aspect ratio of the blocks—consistently much wider than they are tall—would be more indicative of sliding than tumbling and bouncing from the source region above (e.g. Lamb et al., 2015). However, regolith redistribution via creep as outlined in Section 4.1.1 could partially bury the lower portions of the blocks, causing an apparent decrease in height over geologic time. In an alternative interpretation, block emplacement was concurrent with the mass wasting processes that formed the layered plains material, and the large blocks simply made their way to the top of the poorly sorted sediment mixture, due to kinetic sieving (e.g. Marc et al, 2021). If this were the case, we would expect a block size distribution increasing in frequency as size decreases, with a large population of blocks just at the limit of resolvability. The spatial and size distribution of the blocks—without such a large population of small blocks—does not support this single event landslide model.

If these blocks did tumble down from the nearest approximated "summit" onto the plateau below as in Figure 5, they might demonstrate a common terrestrial relationship: larger blocks tend to have longer runout distances due to greater momentum and resilience to breakage (e.g., Corominas et al., 2019). However, the blocky deposit has no significant relationship between block size and runout distance, and some of the largest blocks have the smallest runout distance (Figure 5). Moreover, there is no evidence for tracks or bounce and skip marks discernable at the JunoCam resolution, though these features are only visible for recent rockfall events on Earth, quickly erased by vegetation, fluvial erosion, and hillslope processes.

4.2.3 Outrunner Blocks

Io's blocks are 2-3 orders of magnitude larger and 2-3 orders of magnitude farther from the nearest source area as compared to terrestrial rockfall blocks, though Io's gravity is ~18% that of Earth's, negating some of this distance discrepancy. On Earth, large, lithified blocks associated with submarine landslides can detach from the debris toe and glide along the seafloor, lubricated by a thin layer of seawater (e.g., De Blasio et al., 2006; Mohrig et al., 1998). Outrunner blocks have been described across the world, from the Nigerian Sea

(Nissen et al., 1999) to the Faeroe basin (Kuijpers et al., 2001; Nielsen & Kuijpers, 2004) and the Taranaki basin, New Zealand (Rusconi, 2017). The megaclasts in these deposits can be up to 400 meters tall, 1.9 km long, and 1.2 km wide—a similar size and shape to the blocky deposits (Figure 5). Moreover, there are instances in the Faeroe basin of megaclasts traveling 25 km on a slope less than 1 degree (Nielsen & Kuijpers, 2004), which parallels the 40-120 km runout distances across a slope of a few degrees of the blocky deposit.

Water is not the only lubricant to move large volumes of rock over shallow slopes. Wyoming's Heart Mountain is an enigmatic block of 500-350 million-year-old limestone sitting on top of much younger ~55 million-year-old clastic sedimentary rock, detached from the closest rocks of this unit by ~50 km. The geologic history of the Heart Mountain block is debated, but several interpretations for its formation suggest that it is the product of the largest terrestrial landslide ever recorded, where it's massive size and runout distance over a shallow 2° slope was enabled by lubrication: one hypothesis calls for "hovercraft" floatation on volcanic gases associated with the active Absaroka volcanic province (Hughes, 1970; Beutner & Craver, 1996), while another model proposes basal frictional heating could reach high enough temperatures to calcine the carbonate rock, producing calcium and magnesium oxide powders that could become fluidized by the byproduct pressurized carbon dioxide gas in order to reduce friction for the block to slide (Anders et al., 2010). Yet another interpretation involves an acoustic fluidization process, where a 40-meter-long sound wave trapped just beneath the fault contributed to particle flow as a non-Newtonian fluid at the base of the translating slab (Melosh, 1983).

While both of these megaclast examples provide tidy morphological analogs to Io's blocky deposit, the lubrication mechanism is far less clear. There is no evidence for volcanism directly neighboring these features to provide a heating source, and frictional heating of SO_2 frost (of unknown thickness) to create a gaseous layer to glide on would be unlikely on such shallow slopes.

4.2.4 Cliff Collapse

While this study primarily focuses on the population of blocks adjacent to the West Cocytus Mons, there are six individual blocks mapped adjacent to and below the tall, >1 km high scarps of the layered plains. The simplest model for their association is that the blocks are derived from the layered plains, and large segments cleave off of the cliff, hinging down to the plains below in a cliff collapse process. This scarp erosion mechanism differs from the Type D (debris cone) or Type T (terraced) slopes defined by Moore et al. (2001), because it requires fracturing parallel to the scarp and reflects a greater degree of cohesion, as large blocks remain intact instead of producing smaller scale rockfall debris piles. If all blocks in the blocky deposit unit share a common origin, these marginal blocks may capture this erosional process in action. The population of blocks adjacent to West Cocytus Mons could be the remnant collapse blocks of a now-receded scarp, slowly eroding down into the plains. This variation on the Section 4.1.1 erosional remnant model does not require heterogeneities intrinsic in the crustal layers; the blocks reflect original fracturing size, not erosional resistance. Likewise, the size and aspect ratio of the blocks is consistent with flaking slabs of cliff material.

4.2.5 Endogenic Formation Mechanisms

For completeness, we also consider whether the blocky deposit could have formed in situ from endogenic processes. Though Io's volcanism is concentrated in its paterae, could these blocks be edifices resulting from another magmatic process?

Rhyolite domes form isolated or clustered edifices on Earth due to the slow extrusion of very viscous silicic lava. They generally do not have craters, and can grow as large as Lassen Peak (~3 km tall). There is no evidence for high silica content on Io, as all observed volcanism is hot and mafic, but could be present in local environments if magma ascent is stalled in the cold lithosphere and fractional crystallization is permitted to progress.

Rootless cones, such as those dotting the shore of Lake Mývatn, Iceland, are another smaller-scale, multiple-edifice volcanic construct. These pseudocraters form when lava flows over saturated ground, resulting in explosive phreatomagmatic eruptions as water vaporizes, so they are not connected by a magmatic "root" (e.g., Fagents & Thordarson, 2007). Similar features have been identified on Mars as the result of lava interactions with subsurface water ice (Fagents et al., 2002; Fagents & Thordarson, 2007). Though no central craters can be identified at the JunoCam resolution, their presence cannot be ruled out. The distribution of blocks is also perhaps more consistent with rootless cone clustering on Earth and Mars than the random distribution of an impact crater field (Bruno et al., 2004). While the phreatomagmatic process boasts some similarities to the sublimation of SO_2 frost at the toe of Io's lava flows, the absence of lava flows across the layered plains yield this formation mechanism unlikely.

4.2.6 A Ranking of Preferred Erosional Mechanisms

All mechanisms presented here are variably feasible, though some are included more for completeness than serious consideration. The endogenic formation mechanisms can be ruled out, since the morphologies of the blocks, as well as their distribution (at cliff edges as well as distributed across layered plains), at least at the current resolution, are inconsistent with the volcanic edifices we see on Earth.

Outrunner blocks, while a much better morphological match for the blocks, are an unlikely mechanism, due to the unknown processes necessary to raft the blocks across a shallow slope on Io. While this fun and complex processes could be a possibility, the simplest mechanism is often the more likely explanation.

An erosional remnant, while possible due to the viability of regolith generation and creep on Io, would need to develop over geologic time. Without any known sources for crustal heterogeneities necessary to produce something like the isolated blocks, we must invoke a process like rockfall with subsequent regolith generation and surface evolution. The

distribution of blocks across the plains, as measured from the nearest "summit" does not follow standard terrestrial relationships. Therefore, we consider the combined rockfall and subsequent partial burial of the blocks to be possible.

Ultimately, our preferred formation mechanism for the blocky deposit is cliff collapse. The multiple generations of layered plains preserved in the mapped region provide a likely source of material, and scarp edges deteriorating into large blocks at the margins of these plains demonstrate how such a process could easily produce blocks of the observed proportions. Heterogeneities in the block distribution depend more on the weathering processes driving scarp retreat, which is reasonable.

5 Conclusions

Juno's PJ57 and PJ58s flybys of Io produced spectacular imagery that provides a new perspective on the previously unresolved north polar region of the moon. The low solar incidence angle captured Io's dramatic topography in a new light, allowing us to identify 10 previously mapped features that should be reclassified now that their topographical relationship to the surrounding units is more evident. PJ58 Jupitershine coverage of the Shamshu Patera region further clarifies mountain-patera relationships, and allows us to expand on previously proposed tectonic reconstructions of that region to incorporate similar mountain morphologies separated by rifted plains.

Three polar mountains in particular, connected by several generations of layered plains material, exhibit a greater degree of morphological complexity than can normally be identified in Io's mountains. We present a regional geologic map of this trio that allows us to investigate the relationships between mountain units and degradation states more closely. While the mapped geologic units are consistent with the global paradigm defined by Williams et al. (2010), a new unit is required to describe a unique blocky deposit blanketing the inter-mountain plateau. While similar blocks do appear elsewhere on Io, their abundance in the JunoCam imagery, and relationship with the surrounding geologic units, allows us to

interrogate several possible formation mechanisms for these blocks: an erosional remnant, rockfall debris, outrunner blocks, cliff collapse slabs, or endogenic features like rhyolite domes or rootless cones. While there are consistencies and inconsistencies with all of these mechanisms, a combination of cliff collapse slabs with regolith creep is the most plausible.

Ultimately, the JunoCam images of the north polar mountains capture a new perspective on Io's surface evolution. Lineated mountains are collapsing into mottled mountain material in discrete lobes that extend out on to the layered plains. Layered plains themselves are built with multiple generations overlying each other, forming shallowly sloped plateaus. Blocky deposits sitting atop and at the collapsing margins of these sloped surfaces require even later modification and continual erosion. This new imagery captures an important intermediate stage in the formation and erosion of tectonic features on a volcanic world; what was once an unresolvable smear has become a portrait of Io's dynamic surface erosion in action.

Acknowledgments

We thank NASA, *Juno* mission PI Scott Bolton and the *Juno* team, and in particular the JunoCam instrument team including PI Candy Hansen and Mike Ravine, for acquiring the images of Io used in this study as part of *Juno's* extended mission. We also thank David Crown for the thorough review that improved the clarity of the paper, as well as thesis committee members Mike Lamb, John Grotzinger, and Bethany Ehlmann for their helpful Earth and planetary perspective on the proposed erosional mechanisms. This work was partially supported by NASA's New Frontiers Data Analysis Program and the NASA ROSES Solar System Workings program through task order 80NM0018F0612. Part of this work was performed at the Jet Propulsion Laboratory, California Institute of Technology, under contract to NASA.

Data Availability Statement

JunoCam data presented in this work are archived and freely available to the public in the NASA Planetary Data System (PDS) Imaging Node in PDS3 format. (Caplinger, 2014). NAIF SPICE kernels are used to navigate JIRAM and JunoCam observations and are available publicly in the PDS Navigation and Ancillary Information Facility (NAIF) (Semenov et al., 2017). An integrated ArcGIS database containing *Voyager* and *Galileo* coverage of Io can be downloaded from the Arizona State University Ronald Greeley Center for Planetary Studies (https://rgcps.asu.edu/gis_data/). Block measurements used in this study can be found in Supplementary Data Table S1.

References

Anders, M. H., Fouke, B. W., Zerkle, A. L., Tavarnelli, E., Alvarez, W., & Harlow, G. E. (2010). The role of calcining and basal fluidization in the long runout of carbonate slides: an example from the Heart Mountain slide block, Wyoming and Montana, USA. *The Journal of Geology*, *118*(6), 577-599. https://doi.org/10.1086/656383

Anderson, R. S., & Anderson, S. P. (2010). *Geomorphology: The mechanics and chemistry of landscapes*. Cambridge University Press.

Beer, A. R., Fischer, J. N., Ulizio, T. P., Ma, Z., Sun, Z., & Lamb, M. P. (2024). A mechanistic model and experiments on bedrock incision and channelization by rockfall. *Journal of Geophysical Research: Earth Surface*, *129*(3), e2023JF007504. https://doi.org/10.1029/2023JF007504

Beutner, E. C., & Craven, A. E. (1996). Volcanic fluidization and the Heart Mountain detachment, Wyoming. *Geology*, *24*(7), 595-598. https://doi.org/10.1130/0091-7613(1996)024<0595:VFATHM>2.3.CO;2

Blott, S. J., & Pye, K. (2008). Particle shape: a review and new methods of characterization and classification. *Sedimentology*, *55*(1), 31-63. https://doi.org/10.1111/j.1365-3091.2007.00892.x

Bonneau, D. A., Hutchinson, D. J., DiFrancesco, P. M., Coombs, M., & Sala, Z. (2019). Three-dimensional rockfall shape back analysis: Methods and implications. *Natural Hazards and Earth System Sciences*, *19*(12), 2745-2765. https://doi.org/10.5194/nhess-19-2745-2019

Bruno, B. C., Fagents, S. A., Thordarson, T., Baloga, S. M., & Pilger, E. (2004). Clustering within rootless cone groups on Iceland and Mars: Effect of nonrandom processes. *Journal of Geophysical Research: Planets*, *109*(E7). https://doi.org/10.1029/2004JE002273

Bunte, M. K., Williams, D. A., & Greeley, R. (2008). Geologic mapping of the Zal region of Io. *Icarus*, *197*(1), 354-367. https://doi.org/10.1016/j.icarus.2008.04.013

Bunte, M. K., Williams, D. A., Greeley, R., & Jaeger, W. L. (2010). Geologic mapping of the Hi'iaka and Shamshu regions of Io. *Icarus*, *207*(2), 868-886. doi:10.1016/j.icarus.2009.12.006

Caplinger, M. (2014). Juno JunoCam EDR V1.0 [Dataset]. *NASA Planetary Data System*. https://doi.org/10.17189/1520191

Cardenas, B. T., Beer, A. R., Donohoe, P. J., Kanine, O., Dickson, J. L., & Lamb, M. P. (2025). Crater-wall degradation and bedrock-chute formation from dry rockfall erosion. *Geology*, *53*(5), 456-460. https://doi.org/10.1130/G53096.1

Carlson, R. W., Smythe, W. D., Lopes-Gautier, R. M. C., Davies, A. G., Kamp, L. W., Mosher, J. A., ... & Fanale, F. P. (1997). The distribution of sulfur dioxide and other infrared absorbers on the surface of Io. *Geophysical Research Letters*, *24*(20), 2479-2482. https://doi.org/10.1029/97GL02609

Carr, M. H., McEwen, A. S., Howard, K. A., Chuang, F. C., Thomas, P., Schuster, P., ... & *Galileo* Imaging Team. (1998). Mountains and calderas on Io: Possible implications for lithosphere structure and magma generation. *Icarus*, 135(1), 146-165. Reclassified geologic units based on JunoCam imagery. https://doi.org/10.1006/icar.1998.5979

Conway, S. J., de Haas, T., & Harrison, T. N. (2019). Martian gullies: A comprehensive review of observations, mechanisms and insights from Earth analogues. *Martian Gullies and their Earth Analogues: Geological Society, London, Special Publication* 467, 7–66. https://doi.org/10.1144/SP467.14.

Corominas, J., Matas, G., & Ruiz-Carulla, R. (2019). Quantitative analysis of risk from fragmental rockfalls. *Landslides*, *16*(1), 5-21. https://doi.org/10.1007/s10346-018-1087-9

Crown, D.A., Greeley, R., Craddock, R.A., & Schaber, G.G. (1992). *Geologic map of Io*. US Department of the Interior, US Geological Survey.

Davies, A. G. (2007) Volcanism on Io: a Comparison with Earth. Cambridge University Press, Cambridge, UK. 372 pages.

Davies, A. G., Keszthelyi, L. P., & Harris, A. J. (2010). The thermal signature of volcanic eruptions on Io and Earth. *Journal of Volcanology and Geothermal Research*, *194*(4), 75-99. https://doi.org/10.1016/j.jvolgeores.2010.04.009

Davies, A. G., Keszthelyi, L. P., Williams, D. A., Phillips, C. B., McEwen, A. S., Lopes, R. M., ... & Carlson, R. W. (2001). Thermal signature, eruption style, and eruption evolution at Pele and Pillan on Io. *Journal of Geophysical Research: Planets*, *106*(E12), 33079-33103. https://doi.org/10.1029/2000JE001357

Davies, A. G., Perry, J. E., Williams, D. A., Veeder, G. J., & Nelson, D. M. (2024). New global map of Io's volcanic thermal emission and discovery of hemispherical dichotomies. *The Planetary Science Journal*, *5*(5), 121. https://doi.org/10.3847/PSJ/ad4346

Davies, A. G., Wilson, L., Matson, D., Leone, G., Keszthelyi, L., & Jaeger, W. (2006). The heartbeat of the volcano: The discovery of episodic activity at Prometheus on Io. *Icarus*, *184*(2), 460-477. doi:10.1016/j.icarus.2006.05.012.

De Blasio, F. V., Engvik, L. E., & Elverhøi, A. (2006). Sliding of outrunner blocks from submarine landslides. *Geophysical Research Letters*, *33*(6). https://doi.org/10.1029/2005GL025165

de Kleer, K., de Pater, I., Molter, E. M., Banks, E., Davies, A. G., Alvarez, C., ... & Tollefson, J. (2019a). Io's volcanic activity from time domain adaptive optics observations: 2013–2018. *The Astronomical Journal*, *158*(1), 29. https://doi.org/10.3847/1538-3881/ab2380

de Kleer, K., Nimmo, F., & Kite, E. (2019b). Variability in Io's volcanism on timescales of periodic orbital changes. *Geophysical Research Letters*, *46*(12), 6327-6332. https://doi.org/10.1029/2019GL082691

de Pater, I., de Kleer, K., Davies, A. G., & Ádámkovics, M. (2017). Three decades of Loki Patera observations. *Icarus*, *297*, 265-281. https://doi.org/10.1016/j.icarus.2017.03.016

de Pater, I., Keane, J. T., de Kleer, K., & Davies, A. G. (2021). A 2020 observational perspective of Io. *Annual Review of Earth and Planetary Sciences*, *49*(1), 643-678. https://doi.org/10.1146/annurev-earth-082420-095244

Douté, S., Schmitt, B., Lopes-Gautier, R., Carlson, R., Soderblom, L., Shirley, J., & Galileo NIMS Team. (2001). Mapping SO2 frost on Io by the modeling of NIMS hyperspectral images. *Icarus*, *149*(1), 107-132. https://doi.org/10.1006/icar.2000.6513

Fagents, S. A., & Thordarson, T. (2007). Rootless volcanic cones in Iceland and on Mars. *The Geology of Mars: Evidence from Earth-based Analogs*, 151-177.

Fagents, S. A., Lanagan, P., & Greeley, R. (2002). Rootless cones on Mars: A consequence of lava-ground ice interaction. *Geological Society, London, Special Publications*, *202*(1), 295-317. https://doi.org/10.1144/GSL.SP.2002.202.01.15

Fassett, C. I., Crowley, M. C., Leight, C., Dyar, M. D., Minton, D. A., Hirabayashi, M., ... & Watters, W. A. (2017). Evidence for rapid topographic evolution and crater degradation on Mercury from simple crater morphometry. *Geophysical Research Letters*, *44*(11), 5326-5335. https://doi.org/10.1002/2017GL073769

Fassett, C. I., & Thomson, B. J. (2014). Crater degradation on the lunar maria: Topographic diffusion and the rate of erosion on the Moon. *Journal of Geophysical Research: Planets*, *119*(10), 2255-2271. https://doi.org/10.1002/2014JE004698

Geissler, P. E., McEwen, A. S., Keszthelyi, L., Lopes-Gautier, R., Granahan, J., & Simonelli, D. P. (1999). Global color variations on Io. *Icarus*, *140*(2), 265-282. https://doi.org/10.1006/icar.1999.6128

Geissler, P., McEwen, A., Phillips, C., Keszthelyi, L., & Spencer, J. (2004). Surface changes on Io during the *Galileo* mission. *Icarus*, *169*(1), 29-64. https://doi.org/10.1016/j.icarus.2003.09.024

Gilbert, G. K. (1909). The convexity of hilltops. *The Journal of Geology*, *17*(4), 344-350. https://doi.org/10.1086/621620

Highland, L. M., & Bobrowsky, P. (2008). *The landslide handbook-A guide to understanding landslides* (No. 1325). US Geological Survey.

Hughes, C. J. (1970). The Heart Mountain detachment fault: A volcanic phenomenon? *The Journal of Geology*, *78*(1), 107-116. https://doi.org/10.1086/627491

Jaeger, W. L., Turtle, E. P., Keszthelyi, L. P., Radebaugh, J., McEwen, A. S., & Pappalardo, R. T. (2003). Orogenic tectonism on Io. *Journal of Geophysical Research: Planets*, *108*(E8). https://doi.org/10.1029/2002JE001946

Johnson, R. E. (1997). Polar "caps" on Ganymede and Io revisited. *Icarus*, *128*(2), 469-471. https://doi.org/10.1006/icar.1997.5746

Johnson, T. V., Cooke, I. I., Sagan, C., & Soderblom, L. A. (1979). Volcanic resurfacing rates and implications for volatiles on Io. *Nature (London);(United Kingdom)*, *280*(5725). https://doi.org/10.1038/280746a0

Keszthelyi, L., Jaeger, W., Milazzo, M., Radebaugh, J., Davies, A. G., & Mitchell, K. L. (2007). New estimates for Io eruption temperatures: Implications for the interior. *Icarus*, *192*(2), 491-502. https://doi.org/10.1016/j.icarus.2007.07.008

Keszthelyi, L., Jaeger, W. L., Turtle, E. P., Milazzo, M., & Radebaugh, J. (2004). A post-*Galileo* view of Io's interior. *Icarus*, *169*(1), 271-286. https://doi.org/10.1016/j.icarus.2004.01.005

Keszthelyi, L., McEwen, A. S., Phillips, C. B., Milazzo, M., Geissler, P., Turtle, E. P., ... & Denk, T. (2001). Imaging of volcanic activity on Jupiter's moon Io by *Galileo* during the Galileo Europa Mission and the Galileo Millennium Mission. *Journal of Geophysical Research: Planets*, *106*(E12), 33025-33052. https://doi.org/10.1029/2000JE001383

Kieffer, S. W., Lopes-Gautier, R., McEwen, A., Smythe, W., Keszthelyi, L., & Carlson, R. (2000). Prometheus: Io's wandering plume. *Science*, *288*(5469), 1204-1208. DOI: 10.1126/science.288.5469.1204

Kirchoff, M. R., & McKinnon, W. B. (2009). Formation of mountains on Io: Variable volcanism and thermal stresses. *Icarus*, *201*(2), 598-614. https://doi.org/10.1016/j.icarus.2009.02.006

Kokelaar, B. P., Bahia, R. S., Joy, K. H., Viroulet, S., & Gray, J. M. N. T. (2017). Granular avalanches on the Moon: Mass-wasting conditions, processes, and features. *Journal of Geophysical Research: Planets*, *122*(9), 1893-1925. https://doi.org/10.1002/2017JE005320

Kuijpers, A., Nielsen, T., Akhmetzhanov, A., De Haas, H., Kenyon, N., & van Weering, T. (2001). Late Quaternary slope instability on the Faeroe margin: mass flow features and timing of events. *Geo-Marine Letters*, *20*, 149-159. https://doi.org/10.1007/s003670000053

Lamb, M. P., Finnegan, N. J., Scheingross, J. S., & Sklar, L. S. (2015). New insights into the mechanics of fluvial bedrock erosion through flume experiments and theory. *Geomorphology*, *244*, 33-55. https://doi.org/10.1016/j.geomorph.2015.03.003

Leone, G., Davies, A. G., Wilson, L., Williams, D. A., Keszthelyi, L. P., Jaeger, W. L., & Turtle, E. P. (2009). Volcanic history, geologic analysis and map of the Prometheus Patera region on Io. *Journal of Volcanology and Geothermal Research*, *187*(1-2), 93-105. https://doi.org/10.1016/j.jvolgeores.2009.07.019

Leine, R. I., Schweizer, A., Christen, M., Glover, J., Bartelt, P., & Gerber, W. (2014). Simulation of rockfall trajectories with consideration of rock shape. *Multibody System Dynamics*, *32*, 241-271. https://doi.org/10.1007/s11044-013-9393-4

Lindsay, J. (1976). Energy at the lunar surfaces. In *Lunar stratigraphy and sedimentology* (Vol. 3, pp. 45-55). Amsterdam, The Netherlands: Elsevier.

Lopes, R. M., de Kleer, K., & Keane, J. T. (Eds.). (2023). *Io: A new view of Jupiter's Moon*. Springer. https://doi.org/10.1007/978-3-031-25670-7

Lopes, R. M., Kamp, L. W., Douté, S., Smythe, W. D., Carlson, R. W., McEwen, A. S., ... & Soderblom, L. A. (2001). Io in the near infrared: Near-Infrared Mapping Spectrometer (NIMS) results from the *Galileo* flybys in 1999 and 2000. *Journal of Geophysical Research: Planets*, *106*(E12), 33053-33078. https://doi.org/10.1029/2000JE001463

Mantovani, J. G., Swanger, A., Townsend III, I. I., Sibille, L., & Galloway, G. (2014). Characterizing the physical and thermal properties of planetary regolith at low temperatures. *Earth and Space 2014*, 43-51. https://doi.org/10.1061/9780784479179.006

Marc, O., Turowski, J. M., & Meunier, P. (2021). Controls on the grain size distribution of landslides in Taiwan: The influence of drop height, scar depth and bedrock strength. *Earth Surface Dynamics*, *9*(4), 995-1011. https://doi.org/10.5194/esurf-9-995-2021

McCauley, J. F., Smith, B. A., & Soderblom, L. A. (1979). Erosional scarps on Io. *Nature*, *280*(5725), 736-738. https://doi.org/10.1038/280736a0

McDonald, G. D., Méndez Harper, J., Ojha, L., Corlies, P., Dufek, J., Ewing, R. C., & Kerber, L. (2022). Aeolian sediment transport on Io from lava–frost interactions. *Nature Communications*, *13*(1), 2076. https://doi.org/10.1038/s41467-022-29682-x

McEwen, A. S. (1988). Global color and albedo variations on Io. *Icarus*, *73*(3), 385-426. https://doi.org/10.1016/0019-1035(88)90053-X

McEwen, A. S., Keszthelyi, L., Geissler, P., Simonelli, D. P., Carr, M. H., Johnson, T. V., ... & Schubert, G. (1998). Active volcanism on Io as seen by *Galileo* SSI. *Icarus*, *135*(1), 181-219. https://doi.org/10.1006/icar.1998.5972

McEwen, A. S., Keszthelyi, L. P., Lopes, R., Schenk, P. M., & Spencer, J. R. (2004). The lithosphere and surface of Io. *Jupiter: The Planet, Satellites and Magnetosphere*, 1, 307-328.

McEwen, A. S., & Soderblom, L. A. (1983). Two classes of volcanic plumes on Io. *Icarus*, *55*(2), 191-217. https://doi.org/10.1016/0019-1035(83)90075-1

McKinnon, W. B., Schenk, P. M., & Dombard, A. J. (2001). Chaos on Io: A model for formation of mountain blocks by crustal heating, melting, and tilting. *Geology*, *29*(2), 103-106. https://doi.org/10.1130/0091-7613(2001)029<0103:COIAMF>2.0.CO;2

Melosh, H. J. (1983). Acoustic fluidization: can sound waves explain why dry rock debris appears to flow like a fluid in some energetic geologic events?. *American Scientist*, *71*(2), 158-165. https://www.jstor.org/stable/27851899

Melosh, H. J. (2011). *Planetary surface processes* (Vol. 13). Cambridge University Press.

Migoń, P., & Parzóch, K. (2021). Enigmatic sandstone boulder clusters on the plateaus of the Stołowe Mts.–their geoheritage and geotourism value. *Geologos*, *27*, 141-155. DOI: 10.2478/logos-2021-0017

Milazzo, M. P., Keszthelyi, L. P., & McEwen, A. S. (2001). Observations and initial modeling of lava-SO2 interactions at Prometheus, Io. *Journal of Geophysical Research: Planets*, *106*(E12), 33121-33127. https://doi.org/10.1029/2000JE001410

Mohrig, D., Ellis, C., Parker, G., Whipple, K. X., & Hondzo, M. (1998). Hydroplaning of subaqueous debris flows. *Geological Society of America Bulletin*, *110*(3), 387-394. https://doi.org/10.1130/0016-7606(1998)110<0387:HOSDF>2.3.CO;2

Moore, J. M., Sullivan, R. J., Chuang, F. C., Head III, J. W., McEwen, A. S., Milazzo, M. P., ... & Turtle, E. P. (2001). Landform degradation and slope processes on Io: The *Galileo* view. *Journal of Geophysical Research: Planets*, *106*(E12), 33223-33240. https://doi.org/10.1029/2000JE001375

Nissen, S. E., Haskell, N. L., Steiner, C. T., & Coterill, K. L. (1999). Debris flow outrunner blocks, glide tracks, and pressure ridges identified on the Nigerian continental slope using 3-D seismic coherency. *The Leading Edge*, *18*(5), 595-599. https://doi.org/10.1190/1.1438343

Nielsen, T., & Kuijpers, A. (2004). Geohazard studies offshore the Faroe Islands: slope instability, bottom currents and sub-seabed sediment mobilisation. *GEUS Bulletin*, *4*, 57-60. https://doi.org/10.34194/geusb.v4.4785

Ojakangas, G. W., & Stevenson, D. J. (1986). Episodic volcanism of tidally heated satellites with application to Io. *Icarus*, *66*(2), 341-358. https://doi.org/10.1016/0019-1035(86)90163-6

O'Reilly, T. C., & Davies, G. F. (1981). Magma transport of heat on Io: A mechanism allowing a thick lithosphere. *Geophysical Research Letters*, *8*(4), 313-316. https://doi.org/10.1029/GL008i004p00313

Peale, S. J., Cassen, P., & Reynolds, R. T. (1979). Melting of Io by tidal dissipation. *Science*, *203*(4383), 892-894. DOI: 10.1126/science.203.4383.892

Park, R. S., Jacobson, R. A., Gomez Casajus, L., Nimmo, F., Ermakov, A. I., Keane, J. T., ... & Bolton, S. J. (2024). Io's tidal response precludes a shallow magma ocean. *Nature*, 1-3. https://doi.org/10.1038/s41586-024-08442-5

Perron, J. T., Dietrich, W. E., Howard, A. D., McKean, J. A., & Pettinga, J. R. (2003). Ice-driven creep on Martian debris slopes. *Geophysical Research Letters*, *30*(14). https://doi.org/10.1029/2003GL017603

Perry, J.E., Davies, A.G., Williams, D.A., & Nelson, D.M. (2024) Tonatiuh: A new eruptive volcanic center on Io as seen by Juno/JIRAM. *LPI Contributions*, 3040, 1617. https://www.hou.usra.edu/meetings/lpsc2024/pdf/1617.pdf

Perry, J.E., Heyd, R., Read, M., Tornabene, L.L., … & Berry, K. (2022). Geometric processing of TGO CaSSIS observations. *Planetary and Space Science*, 223, 105581. https://doi.org/10.1016/j.pss.2022.105581

Radebaugh, J., Keszthelyi, L. P., McEwen, A. S., Turtle, E. P., Jaeger, W., & Milazzo, M. (2001). Paterae on Io: A new type of volcanic caldera? *Journal of Geophysical Research: Planets*, *106*(E12), 33005-33020. https://doi.org/10.1029/2000JE001406

Radebaugh, J., McEwen, A. S., Milazzo, M. P., Keszthelyi, L. P., Davies, A. G., Turtle, E. P., & Dawson, D. D. (2004). Observations and temperatures of Io's Pele Patera from Cassini and *Galileo* spacecraft images. *Icarus*, *169*(1), 65-79. https://doi.org/10.1016/j.icarus.2003.10.019

Rapp, A. (1960). Recent development of mountain slopes in Kärkevagge and surroundings, northern Scandinavia. *Geografiska Annaler*, *42*(2-3), 65-200. https://doi.org/10.1080/20014422.1960.11880942

Rathbun, J. A., Spencer, J. R., Lopes, R. M., & Howell, R. R. (2014). Io's active volcanoes during the New Horizons era: Insights from New Horizons imaging. *Icarus*, 231, 261-272. https://doi.org/10.1016/j.icarus.2013.12.002

Ravine, M. A., Hansen, C. J., Caplinger, M. A., Schenk, P. M., Lipkaman Vittling, L., Krysak, D. J., ... & Bolton, S. J. (2024). JunoCam images of Io. *LPI Contributions*, *3040*, 1718. https://www.hou.usra.edu/meetings/lpsc2024/pdf/1718.pdf

Rodriguez, K. (2024). Integrated Software for Imagers and Spectrometers (ISIS) 8.3.0. U.S. Geological Survey. doi: 10.5066/p13tads5

Rusconi, F. J. (2017). *3D seismic interpretation of a Plio-Pleistocene mass transport deposit in the deepwater Taranaki basin of New Zealand*. University of Arkansas.

Schenk, P. M., & Bulmer, M. H. (1998). Origin of mountains on Io by thrust faulting and large-scale mass movements. *Science*, *279*(5356), 1514-1517. DOI: 10.1126/science.279.5356.1514

Schenk, P., Hargitai, H., Wilson, R., McEwen, A., & Thomas, P. (2001). The mountains of Io: Global and geological perspectives from *Voyager* and *Galileo*. *Journal of Geophysical Research: Planets*, *106*(E12), 33201-33222. https://doi.org/10.1029/2000JE001408

Semenov, B.V., Acton, C.H., Costa Sitja, M., Bailey, A.M. (2017). JUNO SPICE KERNELS V1.0 [Dataset]. *NASA Planetary Data System*. https://doi.org/10.17189/1520117

Spencer, D. C., Katz, R. F., & Hewitt, I. J. (2020). Magmatic intrusions control Io's crustal thickness. *Journal of Geophysical Research: Planets*, *125*(6), e2020JE006443. https://doi.org/10.1029/2020JE006443

Turtle, E. P., Jaeger, W. L., Keszthelyi, L. P., McEwen, A. S., Milazzo, M., Moore, J., ... & Schuster, P. (2001). Mountains on Io: High-resolution *Galileo* observations, initial interpretations, and formation models. *Journal of Geophysical Research: Planets*, *106*(E12), 33175-33199. https://doi.org/10.1029/2000JE001354

Turtle, E. P., Keszthelyi, L. P., McEwen, A. S., Radebaugh, J., Milazzo, M., Simonelli, D. P., ... & *Galileo* SSI Team. (2004). The final *Galileo* SSI observations of Io: orbits G28-I33. *Icarus*, *169*(1), 3-28. https://doi.org/10.1016/j.icarus.2003.10.014

Veeder, G. J., Matson, D. L., Johnson, T. V., Blaney, D. L., & Goguen, J. D. (1994). Io's heat flow from infrared radiometry: 1983–1993. *Journal of Geophysical Research: Planets*, *99*(E8), 17095-17162. https://doi.org/10.1029/94JE00637

Williams, D. A., Keszthelyi, L. P., Crown, D. A., Jaeger, W. L., & Schenk, P. M. (2007). Geologic mapping of the Amirani–Gish Bar region of Io: Implications for the global geologic mapping of Io. *Icarus*, *186*(1), 204-217. https://doi.org/10.1016/j.icarus.2006.08.023

Williams, D. A., Keszthelyi, L. P., Crown, D. A., Yff, J. A., Jaeger, W. L., Schenk, P. M., ... & Becker, T. L. (2011). *Geologic map of Io*. US Department of the Interior, US Geological Survey.

Williams, D. A., Keszthelyi, L. P., Crown, D. A., Yff, J. A., Jaeger, W. L., Schenk, P. M., ... & Becker, T. L. (2011). Volcanism on Io: New insights from global geologic mapping. *Icarus*, *214*(1), 91-112. https://doi.org/10.1016/j.icarus.2011.05.007

Williams, D. A., Keszthelyi, L. P., Schenk, P. M., Milazzo, M. P., Lopes, R. M., Rathbun, J. A., & Greeley, R. (2005). The Zamama–Thor region of Io: Insights from a synthesis of mapping, topography, and *Galileo* spacecraft data. *Icarus*, *177*(1), 69-88. https://doi.org/10.1016/j.icarus.2005.03.005

Williams, D. A., Perry, J. E., Nelson, D. M., & Davies, A. G. (2024). Updating Io's North Polar Geologic Map Using JunoCAM Images. *LPI Contributions*, *3044*, 7001. https://www.hou.usra.edu/meetings/pgm2024/pdf/7001.pdf

Williams, D. A., Radebaugh, J., Keszthelyi, L. P., McEwen, A. S., Lopes, R. M., Douté, S., & Greeley, R. (2002). Geologic mapping of the Chaac-Camaxtli region of Io from *Galileo* imaging data. *Journal of Geophysical Research: Planets*, *107*(E9), 6-1. https://doi.org/10.1029/2001JE001821

Williams, D. A., Schenk, P. M., Moore, J. M., Keszthelyi, L. P., Turtle, E. P., Jaeger, W. L., ... & Greeley, R. (2004). Mapping of the Culann–Tohil region of Io from *Galileo* imaging data. *Icarus*, *169*(1), 80-97. https://doi.org/10.1016/j.icarus.2003.08.024

Xiao, Z., Zeng, Z., Ding, N., & Molaro, J. (2013). Mass wasting features on the Moon–how active is the lunar surface? *Earth and Planetary Science Letters*, *376*, 1-11. https://doi.org/10.1016/j.epsl.2013.06.015

Supplementary Data for Chapter 3

This section contains three supplementary figures and one supplementary table. Two figures are presented to provide broader examples of geologic features discussed in the text. This includes regions where substantial geologic evolution was discovered or was expected but absent in the new *JunoCam* imagery (S1). It also includes a visual demonstration of the changes to geologic units that are described in Table 1 of the paper (S2).

One figure indicates where scarp height measurements were made based on shadow length (S3).

Table S1 includes measurements made of the individual block units within the blocky deposit geologic unit. Length and width measurements are geodesic and height measurements are calculated from shadow length. Longitudes are given in 0-180, East Positive regime.

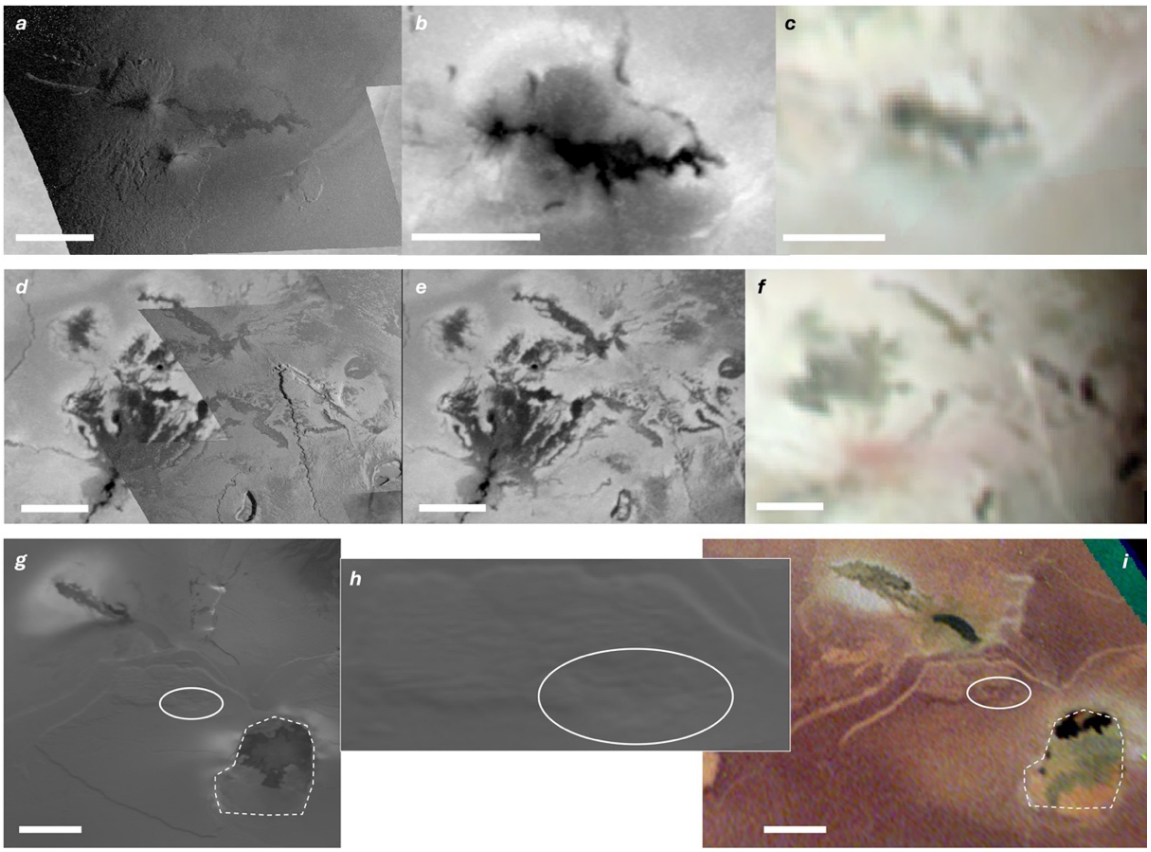

Figure S1. Summary of observations in active regions that did or did not experience measurable change between *Galileo* and JunoCam datasets. Scale bar in all images is 100 km, north is up, and projection is cylindrical. No measurable changes were seen in the Zamama volcanic flow field (18° N, 173° W) between *Galileo* high resolution (a), low resolution (b), and JunoCam (c). However, significant changes to another large flow field were observed at 32° N, 168° W, where dendritic flows fanning northward, visible in *Galileo* high resolution (d) and low resolution (e), became mantled in the southern portion by a new red diffuse deposit visible in the JunoCam image (f). Significant changes were observed in the internal structure of Creidne Patera (white dashed outline in (g) and (i); 52° S, 17° E) between *Galileo* low resolution imaging (g) and JunoCam PJ58 Jupitershine imaging (i), and some putative evolution of tectonic slumping, evidenced by the wrinkled texture on the flanks of Euboea Mons (h), is discernable in the JunoCam Jupitershine image (i), though at the given resolution it is difficult to be certain.

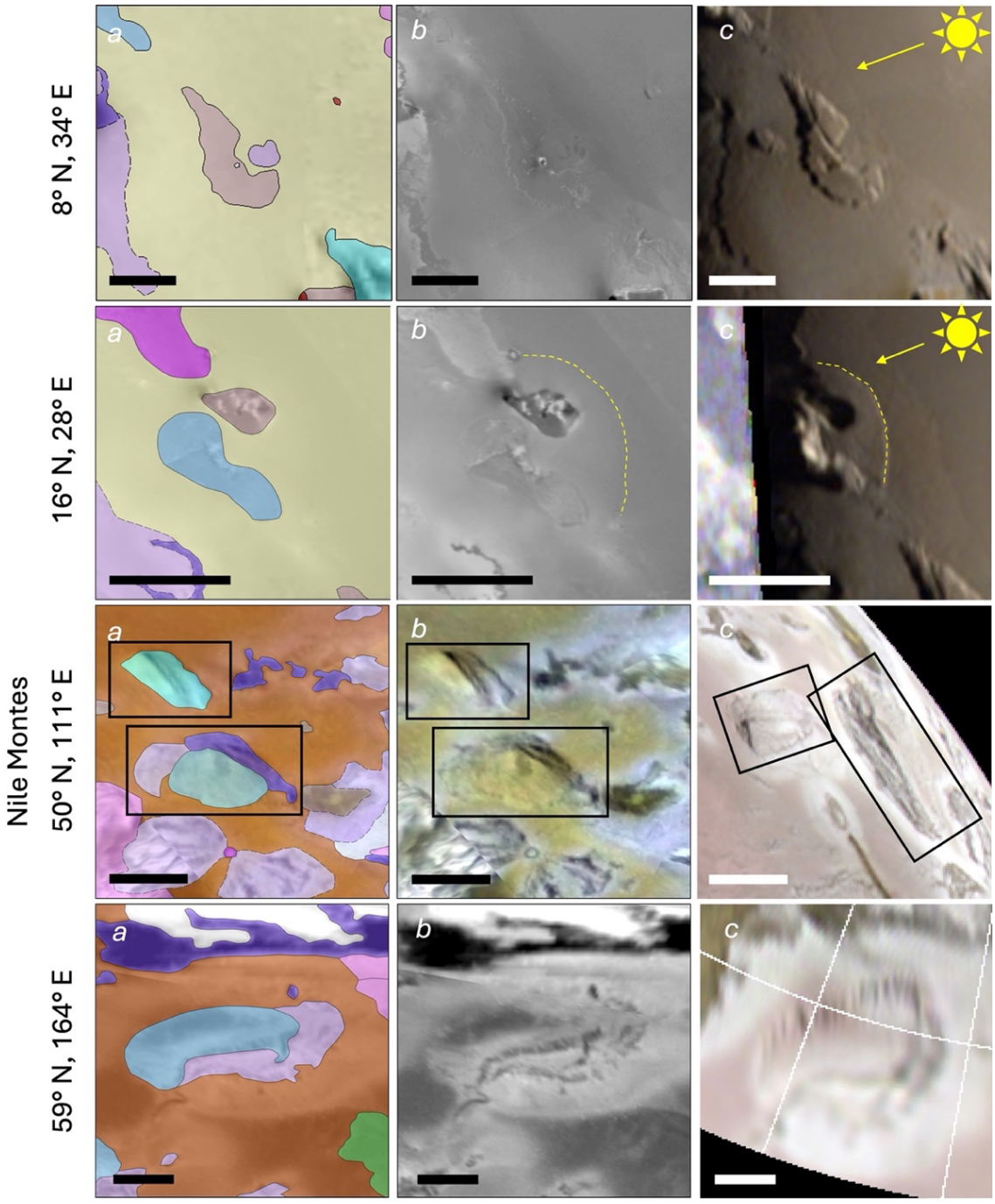
Nile Montes
8° N, 34° E
16° N, 28° E
50° N, 111° E
59° N, 164° E
a
b
c

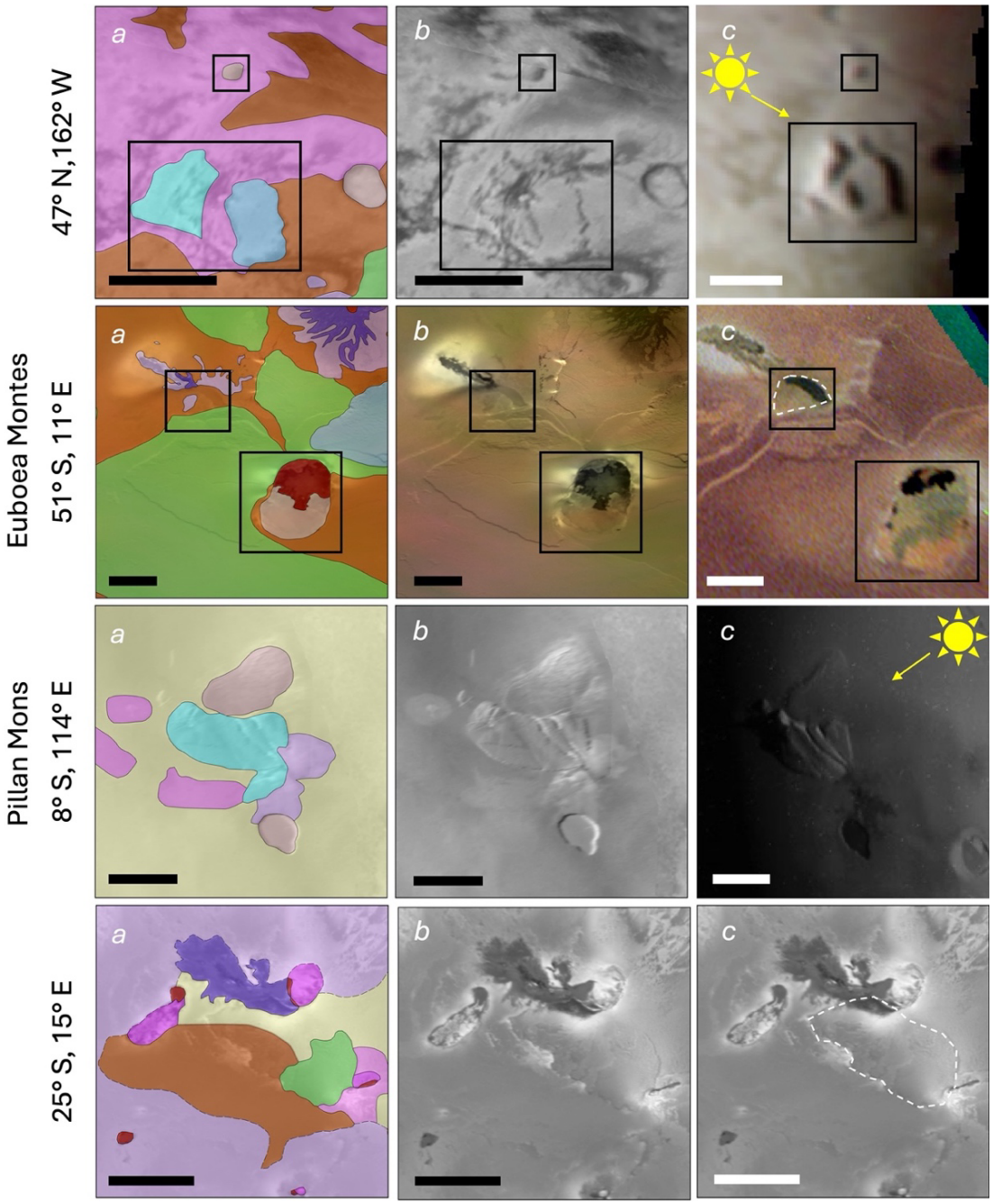

Figure S2. Reclassified geologic units based on JunoCam imagery, as outlined in Table 1. Each row represents a different region, where column *a* includes previous mapping (Williams et al., 2011), column *b* is the *Galileo* and *Voyager* basemap that mapping was based on, and column *c* is the new perspective given by JunoCam (or, in the last two examples, by other *Galileo* views examined as a result of the reclassification exercise). The scale bar in all images is 100 km and north is up. Image centers and feature names (where applicable) are given for each row.

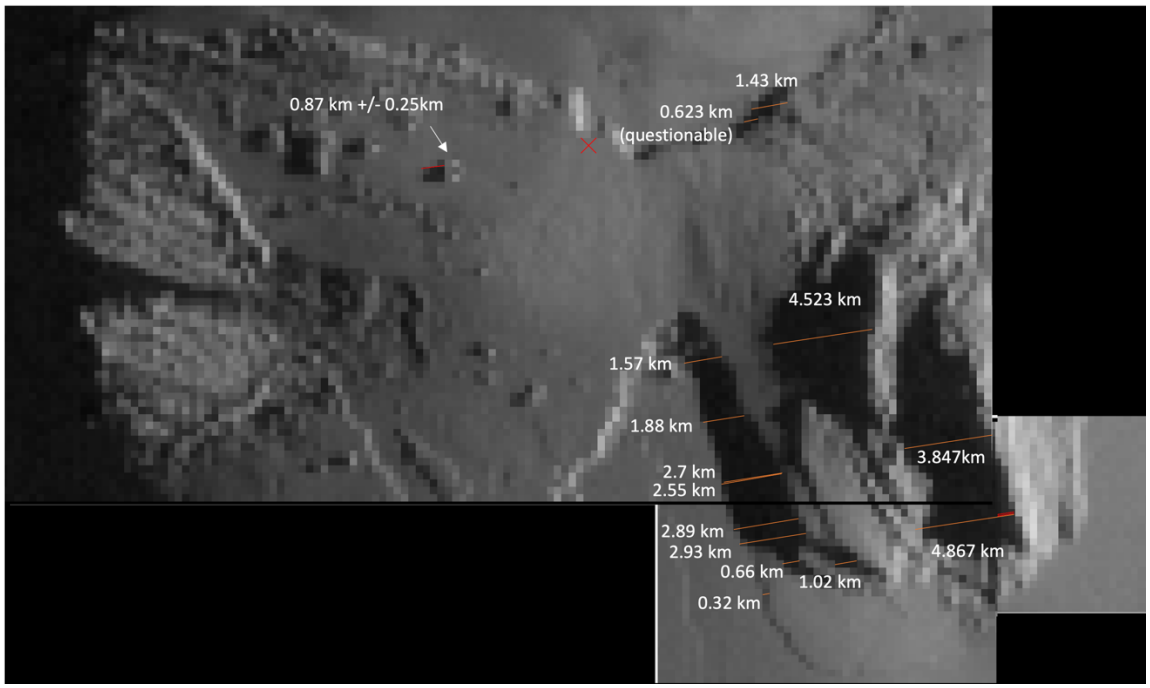

Figure S3. Height measurements of layered plains and East Cocytus Mons as calculated from shadow measurements made following solar azimuth angle across the surface at each location.

Table S1. Measured parameters for individual blocks within blocky deposit geologic unit. Blocks with height of 0 did not have sufficient shadow for measurement.

OBJECTID	Latitude	Longitude	Distance_from_summit_km	Shadow_Length_km	Sun_Azimuth	Block_Height_km	Block_Length_km	Block_Width_km	Length/Height	Block_Volume	Height/Width	Notes
2	60.82736	27.22542	91.78831	3.98967	171.205	0.61727704	25	10.31	0.02469108	159.103158	0.05987168	
3	61.34847	29.08219	117.8498	5.89295	171.256	0.90638004	7.963458	6.109391	0.11381739	44.0970916	0.14835849	
4	61.40018	29.91731	130.1045	1.9787	171.282	0.30341986	4.310261	3.681861	0.07039478	4.81520701	0.08240937	
5	61.71269	29.43829	119.5433	2.05026	171.322	0.31292824	4.553362	3.991073	0.06872466	5.68678231	0.07840704	
6	61.55223	28.3228	106.2353	4.03742	171.283	0.61903811	4.088776	3.097008	0.15139937	7.83886223	0.19988263	
7	61.79947	28.35242	102.8229	7.851	171.313	1.19954884	6.018405	5.354456	0.19931341	38.6558029	0.22402814	
8	62.44519	28.4458	98.72833	1.96581	171.415	0.29677441	5.30384	4.298704	0.05595463	6.76634923	0.06903811	
9	62.51799	27.73345	89.10432	2.399	171.41	0.36238637	3.964229	3.699314	0.09141409	5.31436995	0.09796042	
10	62.64931	27.68081	88.35094	4.05895	171.42	0.6124093	3.573106	3.182543	0.1713941	6.96405126	0.19242766	Questionable
11	62.77937	27.98107	92.40863	2.25284	171.455	0.3384983	3.911666	3.111817	0.08653558	4.12033294	0.10877835	Might be connected to 12
12	62.90679	27.69647	87.21747	4.05944	171.456	0.6098748	6.288322	5.3635	0.0969853	20.5695003	0.11370836	Might be connected to 11
14	63.32523	28.14186	94.41869	5.98567	171.515	0.89296239	8.113219	5.030621	0.11006265	36.4458402	0.1775054	
15	62.77551	28.57093	100.5964	2.06096	171.464	0.30933652	3.933472	3.702616	0.07864211	4.5052193	0.0835454	
16	63.03143	27.36022	82.67974	6.15437	171.466	0.92351074	3.769524	2.609415	0.24499399	9.08388479	0.35391486	
17	63.04311	26.79482	75.26822	6.12427	171.453	0.92041489	2.85502	2.60837	0.32238474	6.85428232	0.35286976	
18	63.13462	25.67455	58.51562	4.25178	171.426	0.64104788	5.228058	3.542861	0.12261683	11.8736701	0.18094074	
19	63.32553	26.338	69.94021	2.38752	171.471	0.35805277	3.869124	2.66742	0.09254104	3.69531183	0.13423187	
22	63.77364	27.51257	88.63478	5.99468	171.565	0.88895946	7.751596	5.094634	0.11468083	35.106382	0.17448937	
23	63.61807	26.65381	75.28506	6.1841	171.504	0.92377857	6.084951	5.099716	0.15181364	28.6662549	0.18114314	
24	63.47401	25.70115	60.26467	7.72544	171.46	1.16008916	7.476936	6.626255	0.15515569	57.4755554	0.17507463	Might be combined with 25
25	63.67261	25.85457	65.1756	6.06259	171.483	0.90789921	7.542783	6.969955	0.12036661	47.7308564	0.13025898	Might be combined with 24
27	63.87855	25.74367	66.88969			0	4.597477	3.971221	0	0	0	Can't see shadow, might be part of 24/25
28	63.895	26.30843	74.23896	4.11979	171.536	0.61306063	4.149945	3.486604	0.14772741	8.87050599	0.17583317	
29	64.02178	27.00985	85.65938	2.02886	171.583	0.30021111	2.82476	2.687983	0.10627845	2.27947498	0.11168639	
30	63.77296	29.5466	116.8811	4.00741	171.645	0.58854715	4.49497546	4.287637	0.13093445	11.3429652	0.13726609	
31	63.70176	24.88313	52.63183	8.09334	171.451	1.21663479	7.959268	3.807342	0.15285762	36.8684812	0.31954965	
32	63.70427	24.01612	44.03091	2.10627	171.432	0.31734022	3.785891	2.022348	0.08382181	2.42968021	0.15691672	
33	63.98037	24.11581	48.79938	3.9535	171.45	0.59438213	9.397274	4.852911	0.06325049	27.1062827	0.1224795	Uncertain about shadow shape
34	64.09924	25.04491	63.08957	4.11669	171.508	0.61465582	6.303148	5.337621	0.09751569	20.6793667	0.11515539	
35	64.07764	23.49324	47.33109			0	3.942632	3.910132	0	0	0	Can't see shadow
36	63.11675	24.99944	49.68889	3.97648	171.403	0.60117309	5.753286	3.571932	0.10449213	12.3543152	0.16830474	
37	61.73606	26.57073	79.83421	5.92367	171.286	0.90793026	5.942057	4.63493	0.1527973	25.0053239	0.19588867	
38	62.07546	27.48255	89.38851			0	3.961482	2.084171	0	0	0	Can't see shadow
39	62.04813	27.21843	82.41064	4.04491	171.345	0.61570735	22.470319	6.250268	0.02740092	86.4733357	0.09850895	Sinuous
40	62.26382	26.24914	67.91234	11.5847	171.349	1.76257018	14.69674	10.38188	0.11992933	268.932589	0.1697737	High uncertainty on shadow shape
41	62.26467	26.80796	77.7942	1.95438	171.356	0.29710755	4.007376	2.609314	0.07414017	3.10670576	0.11386424	High uncertainty, hard to see shadow
42	62.02707	26.64276	77.16136			0	5.350193	3.904117	0	0	0	Can't see shadow
43	61.69993	26.00226	72.79575	4.14899	171.28	0.63636695	4.187555	4.163275	0.15196623	11.0943851	0.15285249	High uncertainty
44	61.01479	25.69715	82.01346	5.92702	171.204	0.91712748	4.39102094	4.043665	0.20886429	16.2843483	0.226806	
45	60.95207	25.14128	78.31122	3.93392	171.2	0.60900299	3.57205982	2.178739	0.1704907	4.73961819	0.27952086	
48	63.11281	29.37173	112.7948	3.99783	171.539	0.59469796	2.71908349	2.314218	0.21871265	3.74216782	0.25697577	

C h a p t e r 4

DIAGENESIS OF THE CLAY-SULFATE STRATIGRAPHIC TRANSITION, MOUNT SHARP GROUP, GALE CRATER, MARS

Christina Seeger[1] & John Grotzinger[1]

Published as:

Seeger, C. H., & Grotzinger, J. P. (2024). Diagenesis of the Clay-Sulfate Stratigraphic Transition, Mount Sharp Group, Gale Crater, Mars. *Journal of Geophysical Research: Planets*, *129*(12), e2024JE008531. https://doi.org/10.1029/2024JE008531

"Consider the subtleness of the sea; how its most dreaded creatures glide under water, unapparent for the most part, and treacherously hidden beneath the loveliest tints of azure…Consider, once more, the universal cannibalism of the sea; all whose creatures prey upon each other, carrying on eternal war since the world began.

Consider all this; and then turn to the green, gentle, and most docile earth; consider them both, the sea and the land; and do you not find a strange analogy to something in yourself?"

Moby Dick, Chapter 58: Brit

Abstract

The diversity and abundance of diagenetic textures observed in sedimentary rocks of the clay-sulfate transition recorded in the stratigraphic record of Gale crater are distinctive within the rover's traverse. This study catalogs all textures observed by the MAHLI instrument, including their abundances, morphologies, and cross-cutting relationships in order to suggest a paragenetic sequence in which multiple episodes of diagenetic fluid flow were required to form co-occurring color variations, pits, and nodules; secondary nodule populations; and two

[1] Division of Geological and Planetary Sciences, California Institute of Technology, Pasadena, California, USA.

generations of Ca sulfate fracture-filling vein precipitation. Spatial heterogeneities in the abundance and diversity of these textures throughout the studied stratigraphic section loosely correlate with stratigraphic unit, suggesting that grain size and compaction controls on fluid pathways influenced their formation; these patterns are especially prevalent in the Pontours member, where primary stratigraphy is entirely overprinted by a nodular fabric, and the base of the stratigraphic section, where increased textural diversity may be influenced by the underlying less permeable clay-bearing rocks of the Glen Torridon region. Correlations between quantitative nodule abundance and subtle variations in measured bulk rock chemistry (especially MgO and SO_3 enrichment) by the APXS instrument suggest that an increase in Mg sulfate upsection is linked to precipitation of pore-filling diagenetic cements. Due to a lack of sedimentological evidence for widespread evaporite or near-surface crust formation of these Mg sulfates, we propose three alternative hypotheses for subsurface groundwater-related remobilization of pre-existing sulfates and reprecipitation at depth in pore spaces.

Plain Language Summary

The Curiosity rover on Mars has traversed a ~800 meter thick sequence of sedimentary rocks in Gale crater. Recently, the rover has traveled through a region broadly transitioning from wetter environments to drier environments, nominally marked by enrichment in magnesium sulfate, which is so soluble its presence in the rock record indicates aridification. The rocks in this region contain a wide variety of unique textures—such as color variation, nodules, and veins—created during diagenesis, a formation and modification phase where groundwater flowed through pore spaces in the rock after it solidified. This study catalogs all diagenetic textures observed up-close throughout this region in order to constrain the order in which they formed, and therefore how many episodes of post-formation fluid flow occurred to produce the record that we see. We also compared the nodule abundance in the rocks to their overall elemental chemistry to suggest that the increase in Mg sulfate detected could be concentrated in the nodules and cements. Ultimately, we use the distribution of nodules and other textures to propose three new hypotheses to explain how groundwater

could have redistributed these salts in the subsurface, with implications for the timing of Mars aridification.

1 Introduction

Sediments and sedimentary rocks on terrestrial bodies can experience multiple generations of transformation, as their constituent grains are transported into a depositional environment, become lithified, and then are subject to subsequent alteration over the course of geologic time—be it aqueous alteration, metamorphism, or weathering. The process of diagenesis, both in cementation and associated mineral authigenesis, and later stage alteration, records a valuable compositional history of the fluids that interacted with sediments. This record can come in the form of cements and authigenic mineral assemblages with specific trace element chemistries that reflect specific primary environments, or alteration products produced by later-stage fluid movement throughout the rocks (e.g., vein mineral precipitation, nodules, color variations, etc.).

On Earth, understanding diagenesis has helped to deconvolve significant pieces of geologic history. For example, bleaching patterns through the otherwise oxidized red-orange sediments of the Navajo sandstone provide constraints on the chemistry and prevalence of buoyant reducing groundwater fluids (likely hydrocarbons like petroleum or methane derived from underlying units) that flowed through heterogeneous pore spaces in these ancient aeolian deposits, moving more easily through the coarser grain flow laminae than the finer-grained, clay-rich wind ripple laminae (e.g., Beitler, 2003, 2005; Bowen et al., 2007; Chan et al., 2000; Parry et al., 2004; Seiler, 2008). These reducing fluids can saturate pore spaces, and when they subsequently come in contact with oxidizing groundwater, diffusion at the interface results in the precipitation of spherical concretions with a distribution determined by geochemical self-organization. The iron oxide concretions in the Navajo sandstone have been widely studied, particularly as analogs for Martian concretions (Beitler et al., 2005; Chan et al., 2005; Ortoleva, 1993; Potter et al., 2011).

Though water-rock interactions on Mars occur in mafic rather than dominantly felsic sediments, we can still use terrestrial examples and present-day alteration products observed by rovers to understand the chemistry and timing of groundwater fluid flow on Mars, perhaps even after liquid water ceased to exist on the surface. While far less common, there are terrestrial examples of diagenetic alteration of volcanic sediments, such as the mixed silicic and mafic sediments of the Ochoco basin in Oregon, which experienced diagenesis from the uniform heating of a perched geothermal aquifer under lava flows **(**Summer and Verosub, 1992). On Earth, diagenesis is often quantified with the water-rock ratio—that is, the mass exchanged between fluid and rock as the fluid passes through and interacts with pore spaces—which can be calculated using stable isotope exchange at equilibrium. Terrestrial equations for volumetric estimates of pore fluids can be modified for Mars with some reasonable assumptions about Martian brines to calculate the amount of diagenetic fluid necessary to produce certain diagenetic features, such as boxwork deposits (e.g., Banner and Hanson, 1990; Siebach and Grotzinger, 2014). Host rock composition can affect the chemical and mineralogical composition of many diagenetic textures, but their physical formation mechanisms are independent of host rock; therefore, terrestrial felsic diagenetic textures remain the most valuable analog for Mars. Previous studies have cataloged diagenetic features in Meridiani Planum, Gusev crater, and Gale crater, as investigated by the Mars Exploration Rover (MER) and Mars Science Laboratory (MSL) Curiosity rover missions (Caswell and Milliken; 2017; Frydenvang et al., 2017; Kah et al., 2018; Kronyak et al., 2019; Meyer et al., 2024; McLennan et al., 2005; Nachon et al., 2014, 2017; Siebach et al., 2014; Stack et al., 2014; Sun et al., 2019; Tosca et al., 2008; Wiens et al., 2017; Yen et al., 2017). These features provide constraints on the chemistry and timing of groundwater movement on Mars, perhaps after liquid water ceased to exist on the surface. In the Murray and Stimson formations in Gale alone, the size, distribution, and paragenetic sequence of the diagenetic textures record at least six post-depositional fluid flow events (Sun et al., 2019).

In this study, we investigate a new suite of diagenetic features exposed in the region of Curiosity's traverse explored from sols 2904-3627, from the Mary Anning drill target in the clay-bearing rocks of the Carolyn Shoemaker formation (Glen Torridon region) to the

Canaima drill target in the sulfate-bearing unit of the Mirador formation. Understanding the relationships among these features, and how they relate to host rock chemistry and mineralogy, can constrain the geologic history of groundwater in the subsurface of Gale crater. This has implications for subsurface habitability, and understanding water-rock ratios is an important constraint on limiting habitability as discussed in Knoll and Grotzinger (2006). The Curiosity mission has determined Gale crater to have once been a habitable surface environment (e.g., Grotzinger et al., 2014, 2015; McLennan et al., 2019). It is worth also considering the conditions for subsurface habitability on Mars. Subsurface rock-hosted life has been identified in the terrestrial rock record dating back hundreds of millions of years up to 3.45 Ga (Tice and Lowe, 2004), and modern microbial life is resilient to a wide variety of conditions: microbes have been found up to 5 km in the continental crust (Moser et al., 2005) and 2.5 km in submarine sediments (Inagaki et al., 2015), at temperatures from -54°C to 122°C, and at pH values from 3 to 13 (Magnabosco et al., 2018). The diversity of environments that support rock-hosted life, from deep groundwater to shallow aquifer and diagenetic fluids, coupled with the early evolution of subsurface life in Earth history and early Martian conditions, support the likely emergence and preservation of similar organisms in a habitable Martian subsurface (Onstott et al., 2019). Indeed, there is chemical evidence that diagenetic fluids precipitating cements in subsurface fractures that weathered into distinctive early vein filling cements in Gale crater's Sheepbed mudstone were potentially habitable, with a low salinity to brackish composition at near-neutral or slightly alkaline pH (Léveillé et al., 2014). By using diagenetic features to explore the ways subsurface fluids may have interacted with basaltic sediments—a process which, on Earth, is known to sustain life—we may be able to expand the time and conditions under which life could have existed on Mars.

2 Geologic Context

The Mars Science Laboratory team, using the Curiosity rover, has spent the last twelve years exploring Gale crater, a ~150 km diameter impact crater located along the Martian crustal dichotomy boundary that is interpreted to have formed ~3.6-3.8 Ga (Le Deit et al., 2013;

Thomson et al., 2011) (Figure 1). This landing site was selected based on the vast sedimentary record exposed along the crater's large, ~5 km tall central mound (Aeolis Mons or, informally, Mount Sharp), that contained distinctive spectral signatures detected from orbit as well as geomorphic signatures of past aqueous events (Anderson and Bell, 2010; Fraeman et al., 2012, Le Deit et al., 2013; Grotzinger et al., 2014; Milliken et al., 2010; Thompson et al., 2011). The rocks exposed along the lower slopes of Mount Sharp are broadly divisible into two units based on their spectral absorptions detected by the Compact Reconnaissance Imaging Spectrometer for Mars (CRISM) instrument: a lower unit that contains hydrated signatures consistent with clay-bearing minerals like nontronite, mixed sulfates and smectites, and Mg-bearing sulfates like kieserite; and an upper unit marked by anhydrous iron oxide spectra (Milliken et al., 2010; Thompson et al., 2011; Sheppard et al., 2020). These two units are separated by an erosional unconformity, which was first recognized by Malin and Edgett (2000) and provides the broadest subdivision of Mount Sharp stratigraphy into hydrated lower and anhydrous upper sediments. The lower unit is divisible into three members, where the transition between phyllosilicate-bearing strata into sulfate-bearing strata occurs within the middle member. This transition is broadly suggestive of a large environmental shift from a wet to dry environment, consistent with the global aridification of Mars (Milliken et al., 2010).

Orbital studies complement the *in situ* observations and measurements made by rovers on the ground. These two observational scales, taken together, give a more complete picture of geologic history than either can independently; rover data can provide textural and compositional details in specific locations which can then be related to spectral signatures and visual imagery that extend far beyond the rover's limited footprint on the ground. Over the past ten years, Curiosity has traveled 32 kilometers along the floor of Gale crater, and then up the side of Mount Sharp, gaining over 800 meters of elevation. Because the strata composing Mount Sharp are relatively flat lying, this ascent of Mount Sharp, despite some lateral variability, can be represented by a generalized stratigraphic column as seen by the rover's ascent through the ~800 meters of strata.

From the landing site near Yellowknife Bay, Curiosity traversed through the fluvio-deltaic sediments of the Bradbury group before reaching the lacustrine mudstones of the Murray formation at the foothills of Mount Sharp (Fraeman et al., 2020; Grotzinger et al., 2015; Hurowitz et al., 2017; Rampe et al., 2017; Williams et al., 2013). The 300-meter-thick package of lacustrine deposits was dominantly planar laminated very fine grained sandstone and mudstone and contained veins and nodules indicative of late stage diagenetic alteration (Fedo et al., 2022; Kronyak et al., 2019; Rivera-Hernández et al., 2020; Sun et al., 2019). The Murray formation gave way to the overlying lacustrine and fluvial strata of the clay-rich Carolyn Shoemaker formation, marking a major paleoenvironmental shift to a marginal lake environment (Caravaca et al., 2021; Cardenas et al., 2022a; Fedo et al., 2022), which was eventually succeeded by an aeolian environment marked by large-scale cross-stratified sandstones of the Mirador formation (Edgar et al., 2024; Meyer et al., 2024).

The Murray and Carolyn Shoemaker formations are consistent with the strata recognized from orbit to be clay-bearing, while the Mirador formation straddles the transition into the Mg sulfate-bearing unit. Therefore, this study focuses on rover observations from sols 2904-3627, which spans the transition of ~250 meters of stratigraphy from clays to Mg sulfates, from -4127 m to -3879 m (Figure 1). The need to circumnavigate a modern eolian sand deposit resulted in a long (1-1.5 km each way) lateral traverse through much of this section, which provided the opportunity to analyze along-strike spatial heterogeneities in this unit, particularly in terms of diagenetic feature diversity, which increased significantly throughout this unit. This lateral traverse through the Glasgow member of the Carolyn Shoemaker formation led Fedo et al. (2022) to characterize the gray mudstone with millimeter-scale lamination as lacustrine deposits, though Cardenas et al. (2022a) identified topographic benches at the eastern end of the traverse to be point-bar deposits or deltaic mouth bars. A ~7-meter-tall cliff feature named Mont Mercou contains strata with variable dip directions consistent with a downstream-migrating fluvial barform that, along with a neighboring ridge, is part of a partially exposed channel belt (Cardenas et al., 2022a). Though a wider regional rover exploration would be needed to determine if these barforms are simply the result of river avulsion, it is likely the fluvial progradation of the Glasgow and Mercou members over

the lacustrine Murray formation strata records the shrinking of the Gale lake system in a drying climate. Approximately 25 meters above Mont Mercou, at the Carolyn Shoemaker—Mirador formation boundary, these fluvial strata gave way to large scale cross bedded aeolian sandstones, with occasional wave ripple-laminated lenses, further solidifying this interpretation as an environmental shift (Edgar et al., 2024).

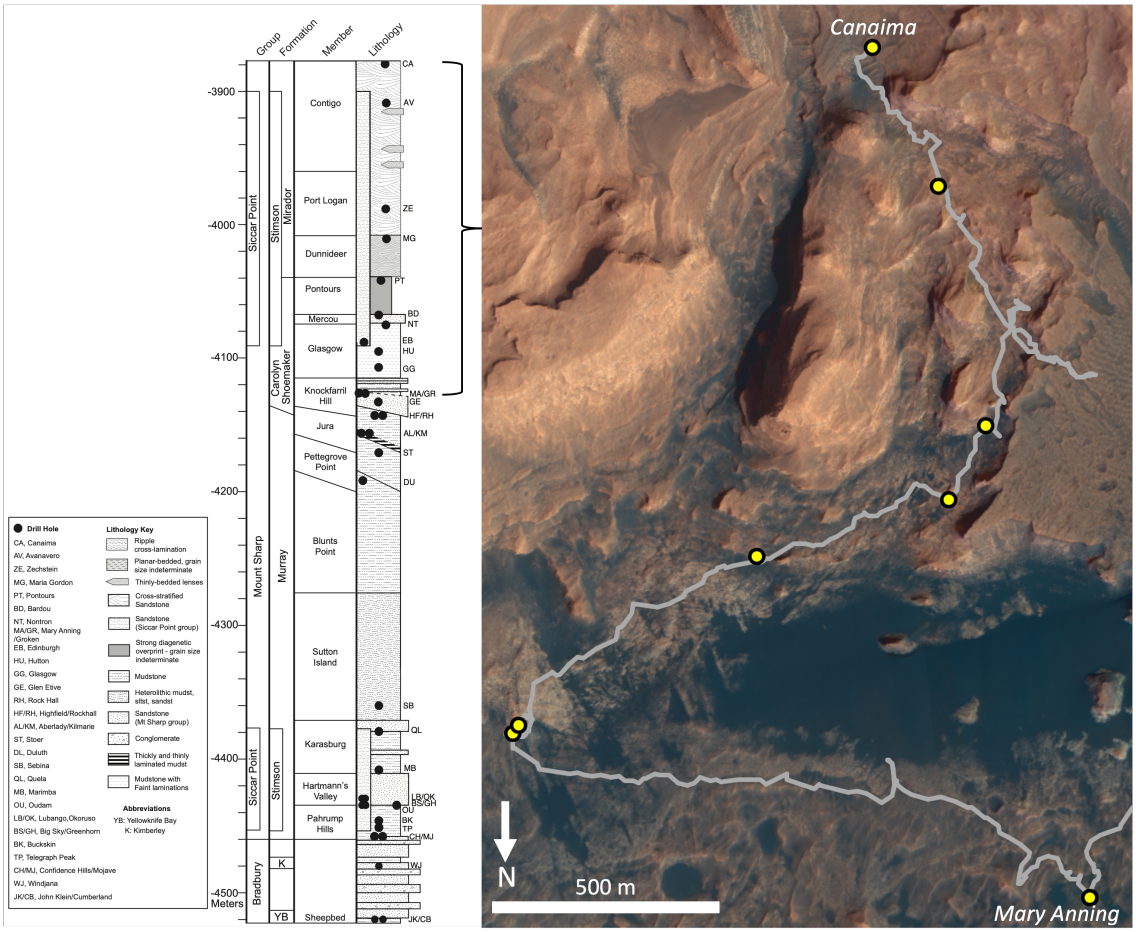

Figure 1. Stratigraphic and geographic context for Curiosity's traverse through study region in Gale crater, with drill targets mapped as yellow circles. This schematic stratigraphic column is a summary of the geology encountered along a lateral traverse through Gale crater condensed into a representative vertical section, with the formations and members referred to in this study outlined at the top.

3 Methods

This study utilized close-up image data collected by the Mars Hand Lens Imager (MAHLI) and contextualized by Mast Camera (Mastcam) imagery, and compositional data collected by the Alpha Particle X-Ray Spectrometer (APXS) that was supplemented by the ChemCam, CheMin, and SAM instruments. The Mastcam instrument consists of two cameras (focal lengths of 34 mm (M34) and 100 mm (M100)) that together capture stereo imagery of nearfield ("workspace" right in front of the rover) and more distant targets (Bell et al., 2017; Malin et al., 2017). Along the study area, Mastcam workspace and drive direction images were analyzed to understand the distribution of diagenetic features (particularly nodules) within the strata. With an M100 resolution of ~150 μm/pixel for targets 2 m away, these images were most useful in identifying large, cm-scale nodules, but were not sufficient for the pervasive smaller nodules along the traverse. However, this imagery was essential to document nodules occurring in patches or organized patterns, particularly when they appear at a distance from where the rover was parked.

Detailed documentation and analysis of the diagenetic features was performed and compiled into a database (Seeger and Grotzinger, 2024) using imagery from the up-close MAHLI imager located on the rover's arm (Edgett et al., 2012). These images were taken at a variety of standoff distances from the rock surface (25 cm, 5 cm, and occasional closer standoffs), with an average resolution of 100 microns/pixel for high standoff and 30 microns/pixel for closer standoff (Edgett et al., 2012). This study utilized 284 MAHLI targets, supplemented with Mastcam imagery during short periods when the MAHLI instrument was offline. Observations based on MAHLI imagery compose the bulk of the database of diagenetic features used for this study, as the high resolution, up-close imagery was necessary to resolve size and shape of many of the millimeter-scale nodules encountered (Seeger and Grotzinger, 2024). In a subset of MAHLI images, individual diagenetic nodules were traced in order to create a binary mask that could be analyzed via a Python script to quantify nodule abundance. This analysis was restricted to the circular area brushed by the Dust Removal Tool (DRT) within each MAHLI image for consistency with other instrument datasets. We therefore

determine the percentage of areal coverage by nodules (independent of their clustering or distribution across the outcrop) by calculating the number of pixels associated with a nodule divided by the total number of pixels in the field of view, including host rock (Figure 4). Abundance measurements are a lower limit, due to the nature of tracing nodules at such a small scale; shadows, image resolution, and dust distribution (particularly in brushed spots) can obscure the true size and shape of some nodules, so those that could not be definitively identified were omitted from measurements.

We relate diagenetic feature abundance to host rock chemistry using elemental abundances derived from the APXS instrument measurements within a 1.7 cm diameter sampled area (Campbell et al., 2012). APXS emits X-rays and alpha particles, and measures the resultant characteristic energy emitted by the constituent elements in the rock to determine the elemental composition. There were 218 APXS measurements on 131 targets collected within the study area, 85 of which were on 46 targets cleared of dust with the Dust Removal Tool (DRT) that had concurrent MAHLI imaging (Berger et al., 2023). Previous studies have linked populations of nodules to variations in elemental composition using ChemCam observations, which can discern individual nodules from host rock due to the instrument's ~200-400 μm diameter laser spot size used to detect elemental abundances via laser-induced breakdown spectroscopy (Wiens et al., 2012; Meyer et al., 2024). From this work, we derive the elements most closely associated with the nodular features to be Mg, S, and Fe. By correlating APXS bulk rock elemental composition, which is a mixture of nodule and host rock, with the quantitative abundances of the nodules as measured in MAHLI imagery, we provide new context for how these unique diagenetic features contribute to bulk rock chemistry. However, these correlations are only general, as there are limitations to this approach: the APXS instrument has radial sensitivity in which 50% of the spectrum comes from the innermost 16% of the field of view (VanBommel et al., 2016), so the elemental contribution from nodules is highly dependent on the location of a nodule in the center of the field of view. The calculated nodule abundances are representative of the rock as a whole, but a deconvolution using several APXS rasters for each point would be necessary to

precisely reflect the contribution from specific nodules to draw more precise conclusions (VanBommel et al., 2016 and 2017).

In addition to the elemental data distributed across the study area, ten drill holes were also analyzed for their mineralogic composition by the Chemistry and Mineralogy (CheMin) X-ray diffractometer, which uses the characteristic X-ray diffraction patterns and fluorescence emitted by specific atoms and crystal structures to identify the minerals within the sample (Blake et al., 2012; Downs et al., 2015). These drilled samples provide bulk rock composition which enables identification of major and minor minerals and phases in the host rock, and sometimes includes diagenetic features in the near-subsurface.

4 Facies descriptions of diagenetic features

A variety of diagenetic features has been documented in abundance throughout Curiosity's traverse (e.g., Gasda et al., 2022; Grotzinger et al., 2014; Meyer et al., 2024; Siebach et al., 2014; Stack et al., 2014; Sun et al., 2019). In the study area of the clay-sulfate transition region, a broad range of fabric elements became abundant in the rocks. Previous work has documented the fine-scale chemistry and variability of some of these textures—particularly nodules—using the ChemCam instrument (Meyer et al., 2024). This complementary study includes a detailed characterization of the breadth of features observed (including nodules and their morphology) from complementary perspective, using the high-resolution imagery of the MAHLI instrument and relationships to broader bulk rock chemistry to further illuminate the relationship between diagenetic textures, primary stratigraphy, and groundwater history in this region.

4.1 Pits and color variations

Pits are negative relief, circular features embedded within the mudstones of the Carolyn Shoemaker formation (Figure 2a). They are sub-millimeter in diameter, and often co-occur with color variations in the rock. The grain size of the enclosing matrix rock is below the resolution of MAHLI (therefore, finer than very fine sand), so these do not appear to be void

casts of sand grains that have weathered out. Zones of color variation appear as centimeter-scale irregularly bounded redder-tone splotches that are otherwise texturally indistinguishable from the rest of the rock (Figure 2a). In the Sol 3110 target Gourdon, the rover's wheels broke some rocks revealing color variations in three dimensions on a fresh face, indicating that this alteration pattern is consistent through several centimeters below the surface, at minimum (Figure 2b).

Terrestrial sandstones frequently exhibit zones of color variation independent of any changes in chemical composition; for example, the Navajo sandstone has both splotchy and layered zones of whiter sediments than their oxidized red counterparts due to fronts of reducing fluids interacting with the iron oxides that converted ferric iron to ferrous iron (e.g., Beitler, 2003). We infer that a similar diagenetic event or events contributed to the color variations observed in the Martian outcrops. It is possible that the pits are dissolution features created by undersaturated fluids moving through pore spaces—perhaps the same fluids that caused zones of color variation, as the two features often co-occur.

4.2 Pervasive concentric fabric

The upper Glasgow member of the Carolyn Shoemaker formation contains several occurrences of a pervasive concentric fabric in some outcrops, composed of millimeter- to centimeter-scale circles of white rock that sometimes have cores or concentric rings of different colors (Figure 2c). When developed, these features occur in such abundance that they dominate the entire surface of the rock. There is no relief difference associated with this fabric, and it otherwise has an identical texture to the surrounding rock.

4.3 Small dark subangular nodules

In two localities, there are highly abundant small, dark subangular nodules that approximately adhere to bedding planes and extend in patches up to ~10cm across (Figure 2d). These features, seen at targets Groken and Pezuls, have a distinctive elemental composition (high in manganese and phosphorous) and have been the subject of detailed

investigation (Treiman et al., 2023; VanBommel et al., 2023). These millimeter-scale dark features are very abundant on the individual bedding planes on which they are exposed. There are no examples of sediment draping over them to indicate syndepositional formation, so they likely precipitated from diagenetic fluids flowing along differently compacted bedding planes after lithification.

4.4 Veins and fins

Calcium-sulfate veins have been observed consistently across all stratigraphic units of Gale crater, from Yellowknife Bay to the mudstones of the Murray formation, and—to a much lesser extent—the unconformably overlying aeolian sandstones of the Stimson formation (Caswell et al., 2017; Kronyak et al., 2019; Nachon et al., 2017; Sun et al., 2019). They are present in every member of the stratigraphic section of this study, though they do vary in abundance; their occurrence is therefore only recorded in this survey for outcrops where they are a dominant feature occurring in abundance. Vein fills also appear as flat, high-relief, sometimes layered surfaces described as fins (Figure 2e, f). These veins are a result of mineral precipitation in structural rock fractures, and are invariably filled with calcium-sulfate precipitate, though local enrichments in iron and magnesium provide important metrics to understand the variability in groundwater redox chemistry and pH conditions (L'Haridon et al., 2018). Fins in this study area are compositionally similar to veins, and less similar to the dark-toned fin-like veins encountered in the Murray formation (Kronyak et al., 2019). Because these features are so pervasive as late-stage diagenetic features (cross-cutting bedding and some earlier generations of veins), they are an essential component of the regional diagenetic history.

4.5 Irregular raised and rounded nodules

Perhaps the most abundant diagenetic features are irregularly shaped, dark-toned, high relief nodules. They range from sub-millimeter scale to several centimeters in diameter, but exhibit similar morphologies across all scales, so are documented and described as a single group (Figure 3a-c). For a further subdivision of these nodules into classes based on color, size,

and composition, see Meyer et al. (2024). Thirteen percent of the examined outcrops containing these nodules have two size populations co-occurring within any given outcrop (Seeger and Grotzinger, 2024). While there are some notable shape-based populations, such as the spherical nodules just above the Zechstein drill hole (which are very round, but not as perfect or as chemically ferric as the hematite "blueberries" in Meridiani Planum (e.g., McLennon et al., 2005)), most can be described as rounded, isolated nodules that sometimes amalgamate into vermiform chains or larger popcorn-like features (Figure 3b). Indeed, MAHLI imagery of many of the large nodules visible in Mastcam imagery show that they may be composed of smaller nodules coalescing together. These nodules sometimes occur in centimeter- to decimeter-wide patches, and other times completely dominate an outcrop (Figure 3d). Where primary stratification is visible, the nodules cross-cut lamination and are not concentrated within certain bedding planes like the small dark subangular nodules. Though Meyer et al. (2024) define a class of lamination-enhancing mm-scale nodules based on ChemCam Remote Micro-Imager (RMI) images, we do not observe a similar distribution in the closer-up MAHLI images aside from rare cases; instead, the mm and sub-mm populations of nodules are distributed across the entire outcrop face. Data collection might influence this discrepancy; MAHLI images are most often taken on smooth, flat-topped rock surfaces due to engineering constraints with associated DRT brushes and APXS measurements, while ChemCam measurements can be taken on more vertically layered surfaces farther from the rover. In some instances, throughgoing lamination can be traced within some larger nodules (e.g., sol 3605 MAHLI target "Tapirapeco" and Meyer et al., 2024 Figure 9A & I). Nodule abundance often anticorrelates with visible primary stratification, and there are notable outcrops of palimpsest lamination (Edgar et al., 2024), as well as regions where the primary bedding is entirely overprinted by nodules (Figure 3d).

In some instances, clusters of nodules are arranged into distinctive patterns. In one locality (Sol 3170 Mastcam mosaic mcam00383), nodules are grouped at the edges of exposed bedding planes, with dendrite-like growth patterns visible in cross-section where it appears minerals could have precipitated to form structures with a growth direction perpendicular to bedding (Figure 3e). There are also multiple regions with nodules arranged in a chevron

pattern, where chains of amalgamated nodules stand in centimeter-scale relief above the bedrock, arranged into evenly spaced ~2 cm wide rows that zigzag across meter-scale regions of flay-lying bedrock (Figure 3f). These features may be related to a similar raised-ridge polygonal features encountered ~10 stratigraphic meters above the chevron pattern. The raised boundaries of the polygons have the same amalgamated nodular texture as the chevron pattern, and their spacing is slightly bigger at ~5 cm in diameter (Figure 3g). These polygonal features may be related to desiccation features (Rapin et al., 2023), or alternatively were the result of self-organized reaction fronts as the diagenetic fluids moved through pore spaces in these rocks (e.g., Ortoleva, 1993). All of these organized nodule patterns were observed within 25 vertical meters of the Pontours drill target, where diagenetic textures pervasively overprint and obscure primary stratification, and at the boundary of a major facies transition from the aqueously deposited Carolyn Shoemaker formation to the aeolian Mirador formation (Edgar et al., 2024). This spatial relationship indicates that a large volume of fluid moved through pore spaces unevenly; perhaps it was a larger volume of fluid than elsewhere, and this resulted in more reaction-front style movement.

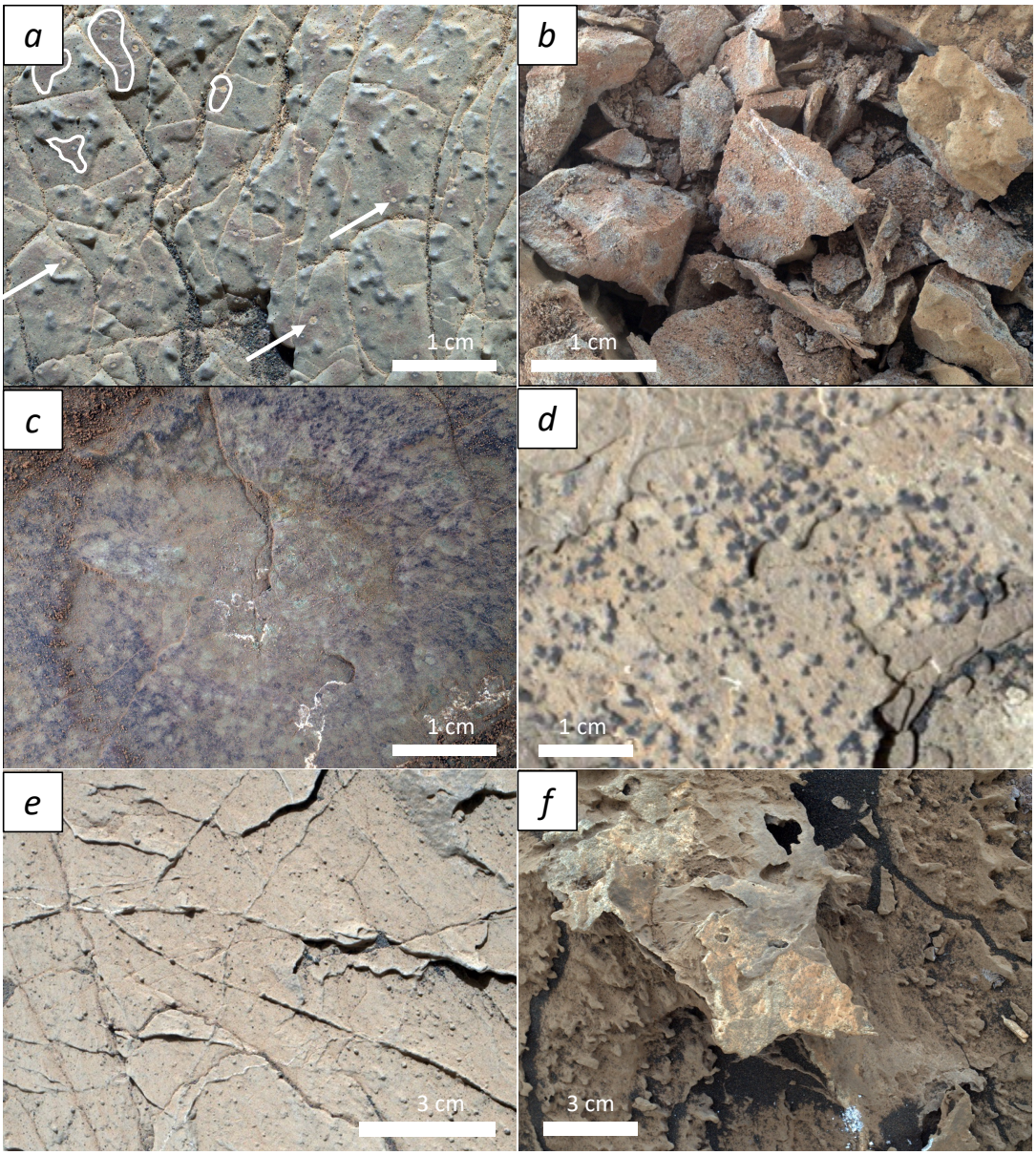

Figure 2. Type examples of the array of diagenetic features encountered throughout clay-sulfate transition region. (a) Color variations, pits, and raised nodules in Sol 3004 target Tomb of the Eagles from MAHLI image 3005MH0001930001100120R00. Example red color splotches are outlined in white and example dust-filled pits are highlighted by white arrows; (b) Fresh rock face broken by rover's wheels exhibiting color variations in three dimensions, Sol 3110 target Gourdon from MAHLI image 3110MH0001930001101741R00; (c) Pervasive concentric fabric in Sol 3024 target Coutures from MAHLI image 3025MH0001630001100520R00; (d) Small dark subangular features from Sol 2906 target Groken in MAHLI image 2906MH0004240011003481C00; (e) Light-toned Ca-sulfate veins from Sol 3054 target Nontron in MAHLI image 3054MH0001900011101097C00; (f) High relief fin-type veins from Sol 3112 target Pezuls in MAHLI image 3112MH0007060021101749C00.

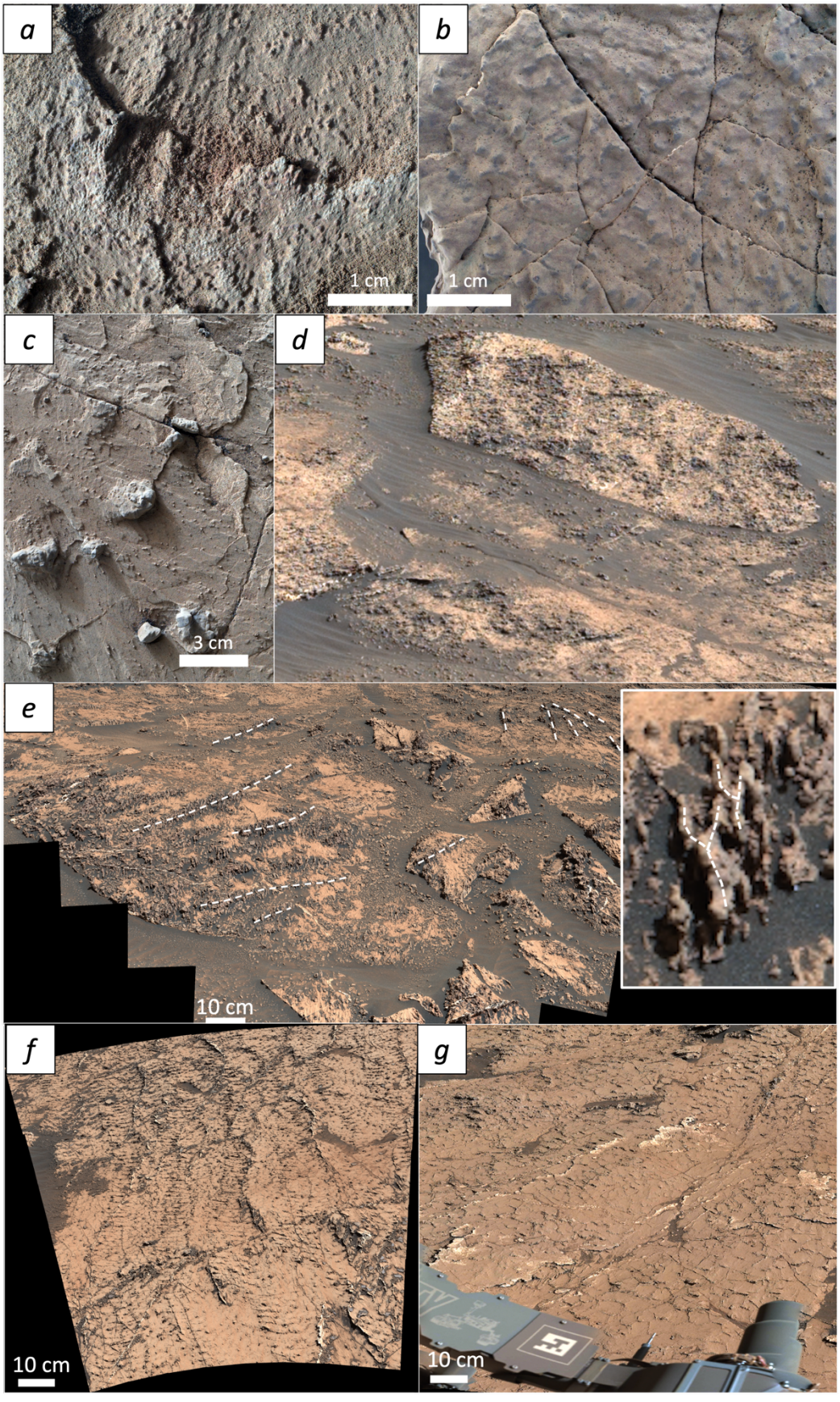
a
1 cm
b
1 cm
c
3 cm
d
e
10 cm
f
10 cm
g
10 cm

Figure 3. Type examples of nodular features encountered in bedrock, demonstrating the diversity of their expressions. (a) sub-millimeter scale nodules visible in DRT spot of Sol 3205 target Grimshader in MALHI image 3206MH0002270001102997R00; (b) ~5mm nodules, arranged independently and in some linear and some vermiform chains, Sol 3024 target Biron in MALHI image 3025MH0001630001100514R00; (c) large ~2 cm nodules in Sol 3051 target Peyrat in MALHI image 3051MH0007060021101063C00; (d) Example of high nodule abundance overprinting and erasing primary stratification, Sol 03202 Mastcam image mcam100573; (e) linearly organized nodules with dendritic growth pattern (inset), Sol 3170 Mastcam image mcam00383; (f) Chevron pattern in Sol 3139 workspace, Mastcam image mcam00178; (g) Polygonal pattern in Sol 3154 workspace, Mastcam image mcam00270.

5 Relationships between diagenetic features

5.1 Nodule spacing and size

Using pixel-by-pixel abundance calculations, we are able to quantify the abundance of nodules in any given bedrock target. Here, we focus on 22 representative nodular targets that were also analyzed by APXS in order to correlate variations in elemental composition with nodule abundance. By creating a binary mask over each MAHLI image demarcating nodules from host rock, we can calculate their abundance, size distribution, and spacing (Figure 4). The densest population of nodules measured corresponds to 25% by area (usually the size of the brushed spot), while the sparsest occurrences of nodules only populate 1.3% of the masked field of view (Figure 4). We have categorized nodular outcrops into three categories: sparse (1-9% nodules by area), moderate (10-19%), and dense (>20%), and used these classifications to better understand the subtle chemical variations in otherwise consistent bulk rock chemistry throughout the clay-sulfate transition (Figure 5, Figure 6).

Because nodule formation is limited by pore fluid saturation levels, we can use these abundances and spacing to understand the timing and number of events where fluids moved through the rock. Most occurrences of nodules have a dominant size, but there are 24 targets containing two populations of of tiny (mm-scale) and large (cm-scale) nodule sizes, with all but two examples occurring stratigraphically above the Pontours drill site, distributed throughout the Mirador formation (Seeger and Grotzinger, 2024). For example, in the sol

3194 target Bregout, ~1 mm nodules are pervasive and overprint some of the larger nodules. Their similarity in morphology to the larger, more amalgamated nodules suggests they may be the result of a remobilization of fluids with similar elemental composition, but under slightly different conditions, such as lower permeability, limiting fluid penetration and therefore causing precipitation of smaller features during any given fluid infiltration or reaction event. In localities where multiple populations of nodules co-occur, several explanations are possible: variations in porosity and proximity to fluid front may have allowed cementing crystals to grow larger in some areas than others, or multiple generations of cementation could have assisted some nodules in growing larger than others over time.

We also compared nodule distribution to the nearest-neighbor statistics computed for nodule analysis of the Burns formation at Meridiani Planum (McLennan et al., 2005). Though the Burns formation is composed of dominantly sulfate-cemented basaltic sand deposited in an aeolian environment, the diagenetic nodules found within are a well-studied analog to compare to the nodules of this study (Grotzinger et al., 2005; McLennan et al., 2005; Squyres et al., 2004). The spherical nodules at Meridiani do not follow a random distribution, and at small separation distances suggest that nucleation at one site precludes the nucleation of another nodule within a certain radius due to locally depleted solute. Rare "doublets" and "triplets" contradict this model, indicating that local heterogeneities in porosity and permeability create zones of enriched or depleted solute. The abundance of chain-linked and amalgamated nodule clusters in the Gale dataset therefore aligns more with the small-scale heterogeneity model than the radial exclusion zone of the dominantly singular Meridiani nodules. However, perhaps more likely than a radial exclusion zone is a lateral exclusion zone orthogonal to the direction of fluid propagation, creating the clustering and chain-like arrangement of nodules aligned in a given direction. While this phenomenon may be most obvious in the large-scale chevron and polygonal patterns created by nodule chains, it may also be observed in nodule-scale subtle alignment patterns such as the general upper left to lower right fabric visible in Figure 4b (though this could possibly be the result of incidence angle bias).

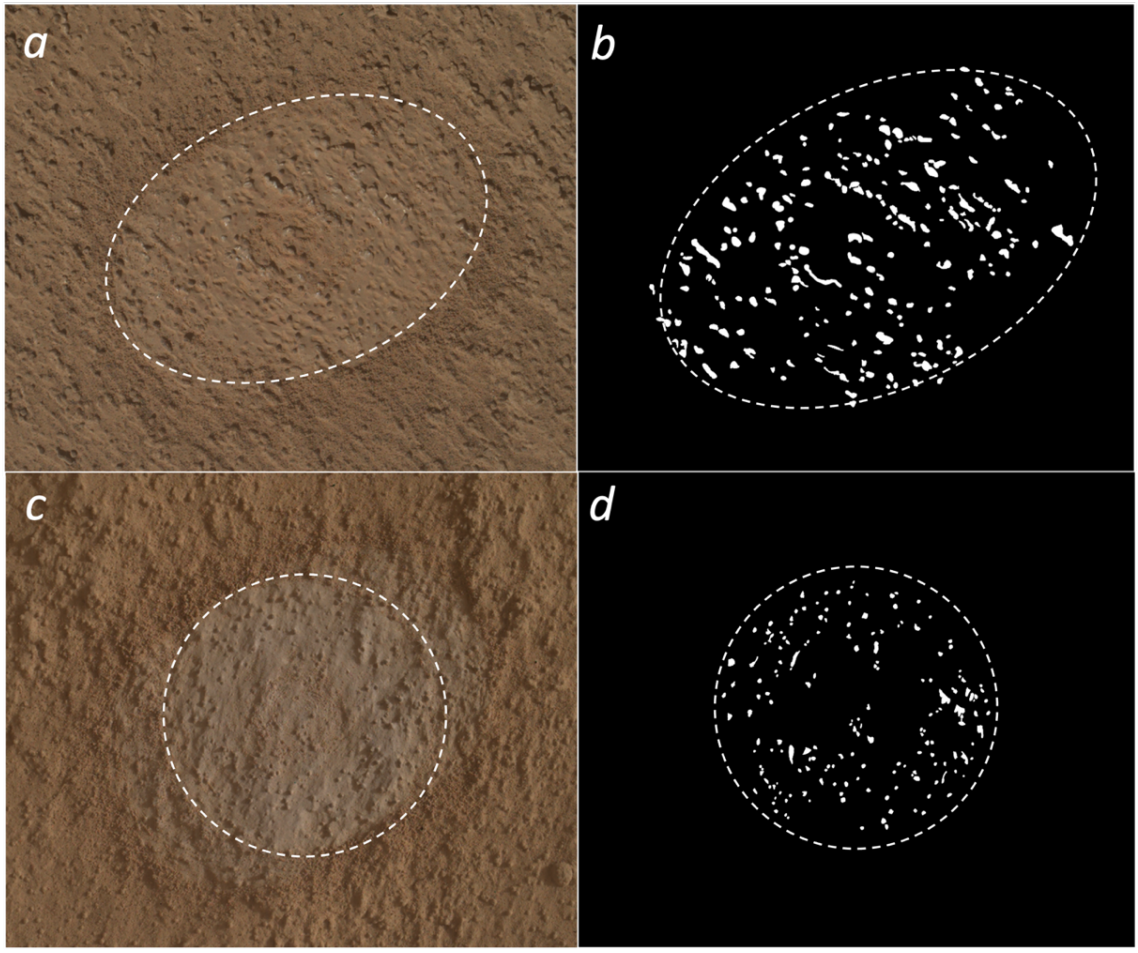

Figure 4. Image processing techniques were used to better quantify nodule abundance, especially in targets that were analyzed for elemental composition with APXS. (a) Outlined DRT spot in sol 3224 target Maria Gordon with (b) corresponding binary image mask distinguishing nodules (white) from bedrock (black). (c) Outlined DRT spot in sol 3388 target Loch Coriusk with (d) corresponding binary image mask distinguishing nodules (white) from bedrock (black). DRT spots are ~4.5 cm wide.

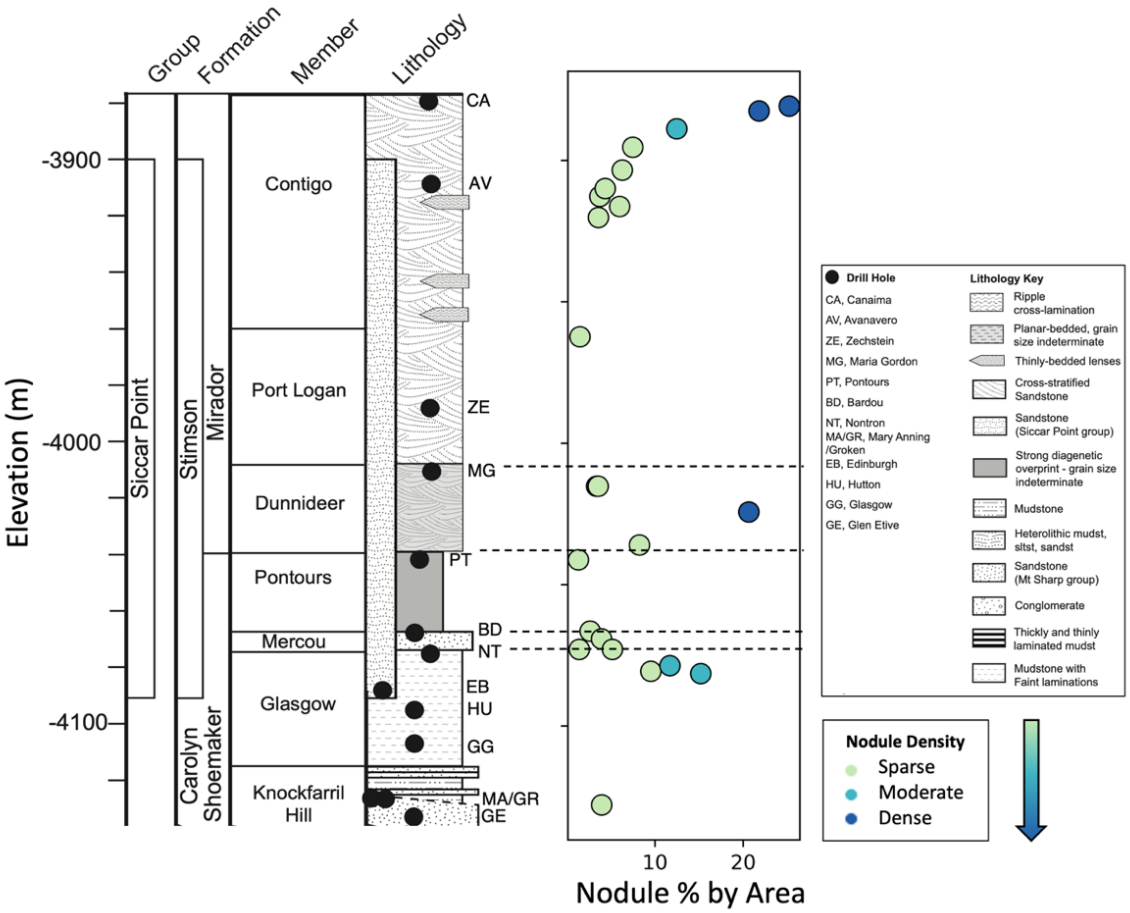

Figure 5. Distribution of nodules abundances (% by area) across clay-sulfate transition region for APXS targets where elemental data was collected; dot color corresponds to abundance characterizations of sparse (1-9% nodules by area), moderate (10-19%), and dense (>20%).

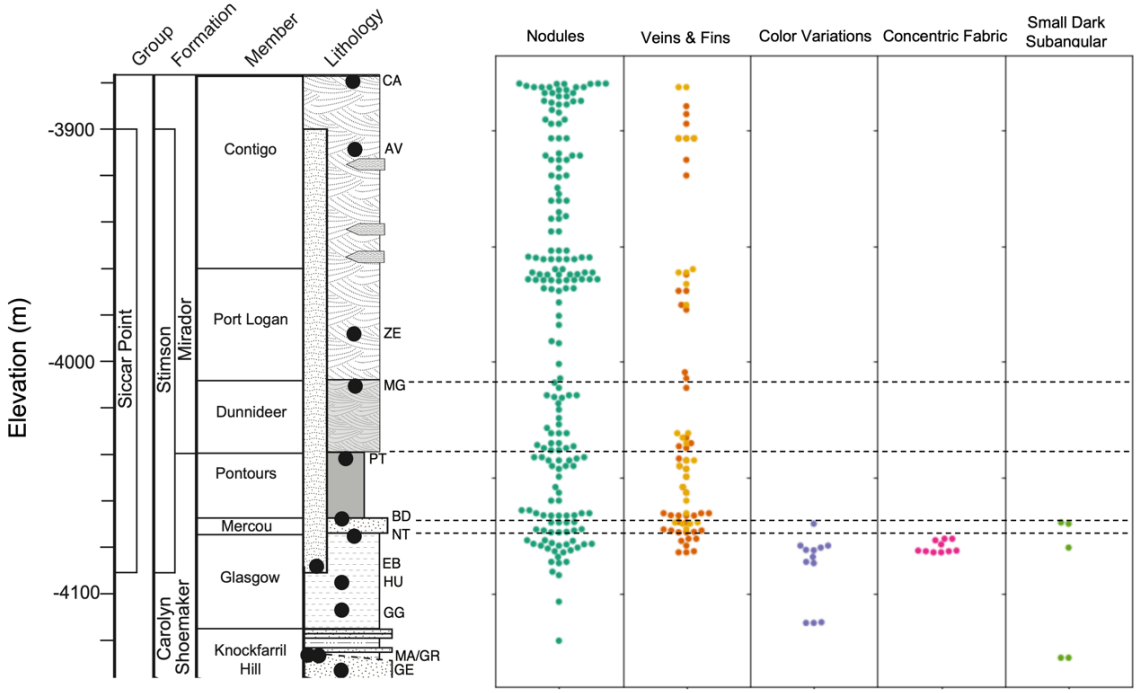

Figure 6. Schematic stratigraphic column corresponds to simplified representation of rock units encountered along lateral traverse condensed into a representative vertical section; locations where each diagenetic feature type was observed are marked by elevation to correspond with stratigraphic units. Note that veins are ubiquitous in Gale crater, but only recorded here in outcrops where they are an abundant, dominant feature.

5.2 Cross-cutting relationships

Determining the paragenetic sequence of diagenetic textures helps constrain the nature and timing of post-depositional subsurface fluid flow events. For every texture, there is at least one instance of co-occurrence with another texture type. For example, veins, which have been observed consistently throughout Gale crater, often bisect other textures. Though it is not common to observe veins cutting singular nodules, partly due to probability, they do obviously cross-cut high-standing large cluster-like nodules. This is particularly evident in areas of meter-scale surface expression of nodule organization into linear, polygon, or chevron shapes, where large veins intersect large swaths of the nodule pattern (Figure 3). However, the cross-cutting relationships are not uniformly obvious, and relationships can be obscured by irregular shapes, dust cover, and multiple generations of feature formation (for

example, high-angle fractures cut across low-angle fractures that often parallel and sometimes obscure bedding planes).

A subtle and poorly expressed, but very distinctive cm-scale vertical fabric is evident in several nodular outcrops, including the upper 2/3 of outcrop expressed at Mont Mercou. This fabric is defined by long, straight, parallel columns a few centimeters in width that are spaced approximately ten centimeters apart and can be traced vertically for one or more meters (Figure 7). The texture within the columns is subtle, but is slightly more resistant to erosion and slightly obscures the primary stratification. This fabric is cross-cut by the more defined fractures through the upper portion of the outcrop (Mondro et al., 2023), which further complicates our interpretation of the paragenetic sequence; perhaps this verticality is created by fluids exploiting zones of weakness that later develop into fractures.

The fractures, vein fills, and spaced vertical fabric are considered late-stage diagenesis, but it cannot be discounted that some nodule formation—particularly the subvertical chain pattern—could have also occurred later than some other nodule formation. The estimated paragenetic sequence for all diagenetic feature types observed in the study area is summarized in Figure 8, where color variation, pit, and nodule formation can not be disentangled, but form sometime after lithification. Because nodules and color variations do not overprint one another, they may have formed under the same conditions, where small heterogeneous variations in pore space (possibly due to compation) resulted in leaching from some areas and precipitation in others. Bimodal nodule size populations and the organization of some nodules into larger clusters or organized chains suggests at least two different diagenetic events. The latest stage of alteration includes at least two generations of fracturing followed by Ca sulfate vein precipitation, first in a subhorizontal orientation, and later forming high-angle fracture-filling veins.

Figure 7. Vertical exposure of Mont Mercou outcrop demonstrating subtle vertical fabric independent of fracturing; three regions with resistant columns have been traced as example, but fabric can be seen across entire outcrop and is particularly consistent in the lower portion of the image. Sol 3060 Mastcam mosaic mcam15984.

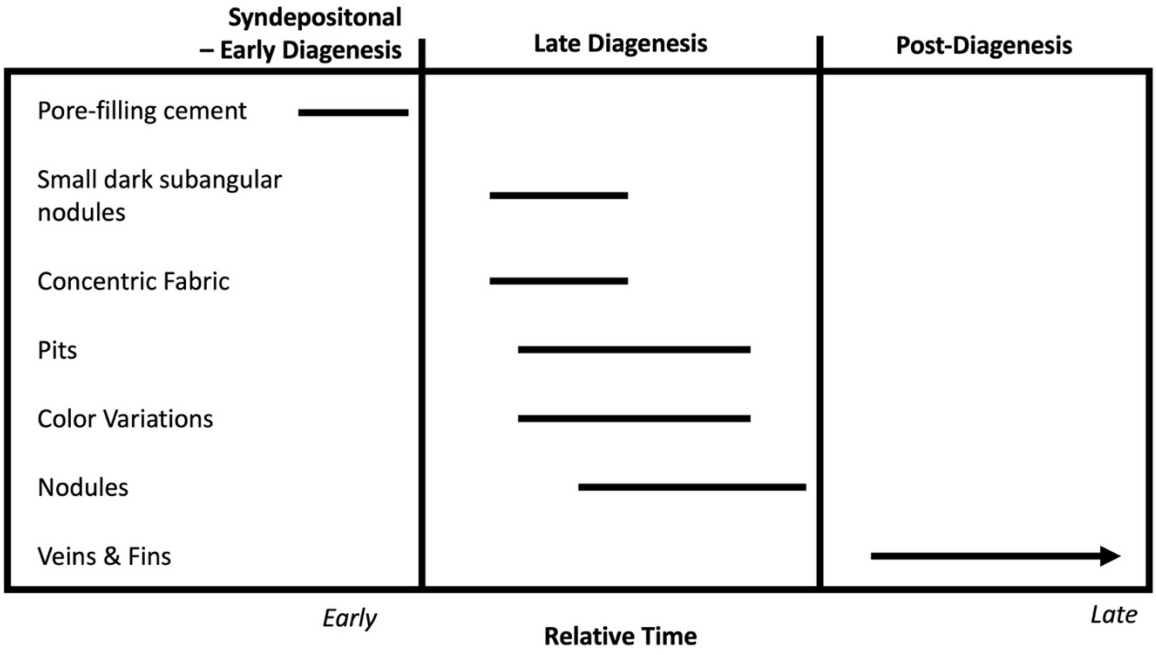

Figure 8. Schematic diagram showing relative paragenetic sequence of diagenetic feature formation in relative time.

5.3 Feature distribution along rover traverse

The diverse array of diagenetic textures encountered along Curiosity's traverse allow us to track fluid movement through different parts of the Gale sedimentary basin, recorded by its stratigraphic record. Figure 5 and Figure 6 summarize the distribution of these features. Due to the nature of the rover's route, a large lateral traverse—mostly along strike—of the ~40 m thick Glasgow member of the Carolyn Shoemaker formation was sampled. From the Mary Anning drill site to Mont Mercou, diagenetic textures increased dramatically in abundance and diversity, but did not overprint bedding; rather, unique textures (such as color variations and pervasive concentric fabric) were observed, but did not alter the host rock to a degree greater than that previously observed in the mission (Sun et al., 2019). The Mont Mercou locality marked a distinct shift in expression of diagenetic overprints; though the drill hole at the base of the cliff (Nontron) and on top of the cliff (Bardou) have very similar elemental compositions (Rampe et al.,2022), strong overprinting of primary stratification at the base becomes amplified in the upper third of the vertical outcrop, where primary stratification is completely destroyed (Figure 7). This overprint consists of low-angle fractures, nodules, veins, and the subtle, centimeter-scale vertical fabric described above. Cardenas et al. (2022a) interpret the erosion-resistant strata of Mont Mercou to be a downstream-migrating fluvial barform that is part of a larger channel belt, indicating that this outcrop not only marks a shift in diagenetic alteration, but also a shift in depositional environment during lake level in the gradual drying of the Gale lacustrine system. The change in grain size (and therefore porosity) in this barform could have increased pathways for a fluid front to move through the sediments and overprint primary strata to a significant extent uncommon in Gale crater, resulting in a total loss of primary stratification in some zones.

Moving up stratigraphically from Mont Mercou, nodules and veins dominate the strata, and pervasively overprint and erase primary stratification. At the Pontours drill site, just below a transition into low-angle cross-stratified sandstones, nodules are extremely abundant and primary stratification is completely overprinted. The examples of outcrop-scale nodule organization into chevrons and polygonal shapes also are concentrated in the ~25 meters of

stratigraphy below this drill hole. The presence of nodules remains strong from Pontours to Maria Gordon, though cross-stratification is interspersed with several-meter-scale patches of large, irregular and rounded centimeter-scale nodules (Edgar et al., 2024). Above Maria Gordon, nodules are smaller, sparser, and less obstructive of the primary large-scale cross-stratification (Edgar et al., 2024), though there are some notable variations: just above the Zechstein drill hole, highly spherical nodules are abundant. These have similar elemental composition and morphology to the raised and rounded nodules observed at lower stratigraphic levels, and therefore differ from the hematite "blueberries" in the Burns formation at Meridiani planum. Additionally, in the same area, there are centimeter-scale highly angular nodules that appear to be concentrated along bedding planes. Due to image resolution and the angles at which these features are exposed, we cannot conclusively determine if they are pseudomorphs after evaporite hopper crystals (e.g., halite), but the possibility of very late stage evaporite deposits in resurgent brines could be considered.

5.4 Chemical context

Previous work has demonstrated that Martian nodules can have similar or distinct chemical compositions as compared to their host rock (Sun et al., 2019; Gasda et al., 2022). Using ChemCam data, Meyer et al. (2024) demonstrate that the nodules in this region are enriched in sulfate (dominantly Mg, but some Fe as well), which may in part contribute to the orbital spectroscopic Mg sulfate signatures identified by Milliken et al. (2010) and Sheppard et al. (2021). CheMin drill data show that while the Nontron and Bardou drill holes bracketing Mont Mercou contain 18 wt.% and 12 wt.% nontronite respectively, Pontours and Maria Gordon only have a trace amount of phyllosilicate, and Zechstein does not contain any above the CheMin detection limit of 1 wt.% (Rampe et al., 2022). The disappearance of clay minerals throughout the clay-sulfate transition region is not accompanied by an increase in Mg sulfate observed by CheMin (which did not detect any crystalline Mg sulfate until the Canaima drill target, as reported by Chipera et al., 2023), though the SAM instrument did detect small amounts of Mg sulfate in the latter three drill targets, suggesting that the Mg sulfate in this region is X-ray amorphous (Clark et al., 2023; Rampe et al., 2022).

Observations by the MSL instrument suite therefore support the interpretation that the Mg sulfates of this region are amorphous products contained within the heterogeneously distributed diagenetic nodules. Thus, the "clay-sulfate transition" region is marked by a significant decline in clay minerals without a commensurate significant increase in the concentration of sulfate until the detection of crystalline Mg sulfate at the end of our study region.

Elemental composition may vary across specific parts of nodules, and also from nodule to nodule, as shown by ChemCam measurements of individual nodules (Meyer et al., 2024). It is therefore useful to accompany ChemCam measurements with APXS analyses, which can average intra- and inter-nodule heterogeneities within the instrument field of view. Elemental plots for nodular targets overlying all APXS targets within the study area demonstrate elemental enrichments in nodules in certain parts of the stratigraphy (Figure 9). Note these trends reflect the overall nodular abundances measured for each outcrop, and do not account for the presence or absence of nodules in the center of the APXS field of view; deconvolving the spectrum to isolate nodule composition could further illuminate these trends but is outside the scope of this work. Nodules are the only diagenetic fabric element isolated for this dataset because targets with most other feature types (veins, color variations, etc.) also contain nodules, making it impossible to compositionally isolate them with APXS. Given the abundance of certain elements in both terrestrial and Martian concretions (e.g., Sun et al., 2019; Gasda et al., 2022) we looked at Mn, Fe, Si, Na, and Cl to try and understand what the cementing phase was that created differential resistance to weathering.

Mn is not enriched above background within the nodular targets. However, plots of FeO vs. SiO2 display two distinct trends: bedrock targets (light grey points in Figure 9) have a population exhibiting a positive correlation, which may indicate the presence of detrital mafic minerals or clays like Fe/Mg smectites. In a second population FeO and SiO_2 are anticorrelated, possibly reflecting an iron oxide enrichment consistent with CheMin detections of Fe oxides within the study region. The subpopulation of highlighted nodular targets falls along the positive correlation line with a weak but significant relationship (r^2 =

0.1086), indicating that there may be a clay contribution to the nodule composition. Previous analyses of diagenetic fabrics earlier in the rover's traverse detected Mg-Fe phyllosilicates cementing raised ridges in the Sheepbed Mudstone (LeVeille et al., 2014), so while the expression of features is different, the composition may have precedent.

The set of nodular targets closest to Canaima (therefore at the top of the stratigraphic section) fall close to the MgSO4 addition line, while also showing significantly lower levels of CaO. Targets in the lower portion of the stratigraphic section also cluster around the MgSO4 addition line, even when they are lower in Mg. These measurements corroborate the increased Mg sulfate detected in individual nodules by ChemCam (Meyer et al., 2024).

We also consider how nodules can contribute to the bulk rock elemental signature as measured by APXS by correlating their quantitative abundance to subtle changes in Mg, S, and Fe measurements (Berger, 2024). Nodule density measurements presented in Section 5.1 were correlated with the APXS elemental abundances for those same targets (Figure 10). While outcrops with all nodule densities can be found throughout the stratigraphic section, the densely nodular targets in the upper Mirador formation also tend to have the higher concentrations of both MgO and SO3, and lower enrichment in CaO. We can therefore use these measurements in conjunction with the ChemCam detections of Mg sulfate within certain nodules to infer that in the upper stratigraphy of the clay-sulfate transition region, amorphous Mg sulfate is concentrated in nodules and cements at such abundance that they influence the bulk rock elemental composition as measured by APXS.

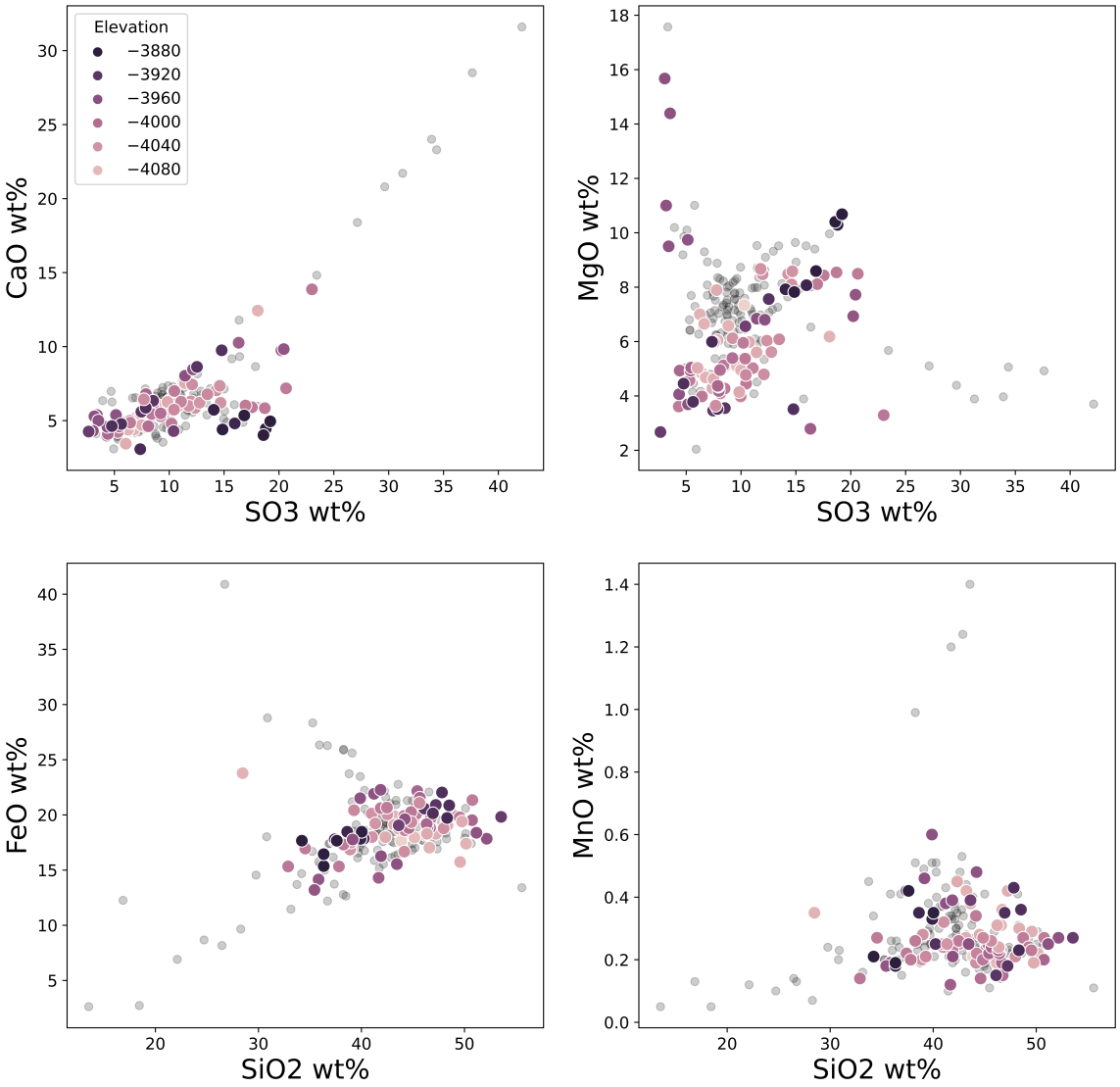

Figure 9. Elemental abundances for all APXS targets in study area (light gray), with nodule-rich DRT targets highlighted with hue corresponding to elevation (as a proxy for stratigraphic position).

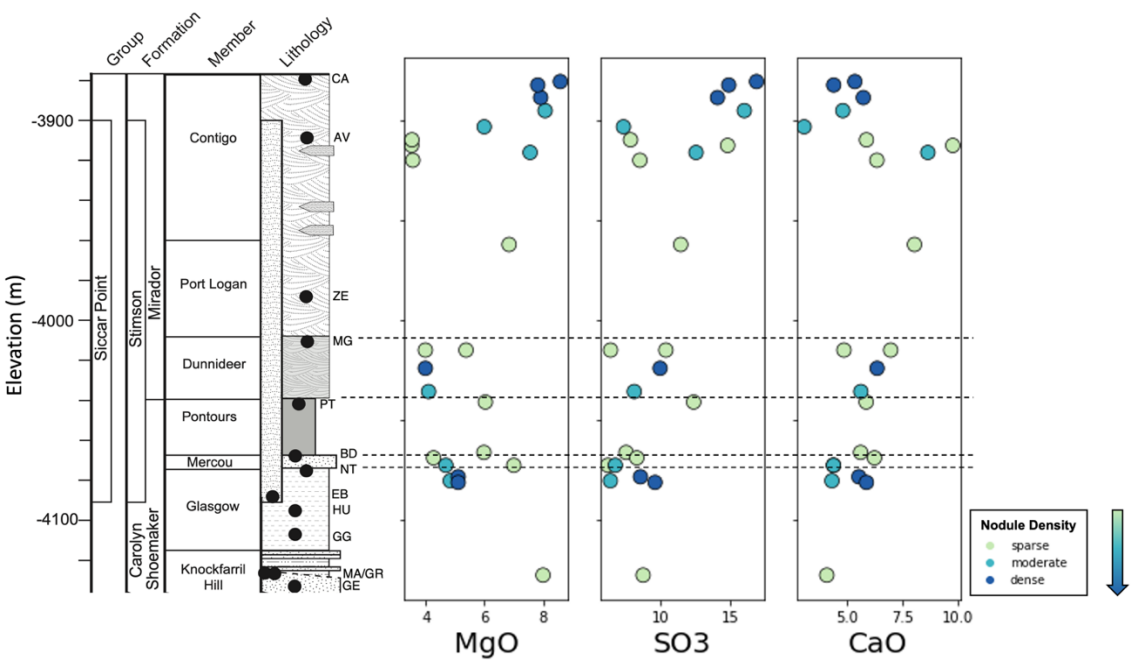

Figure 10. General correlations between quantitative nodule abundance classes and elemental enrichment in wt.% MgO, SO_3, and CaO in APXS targets across the clay-sulfate transition.

6 Discussion

The chemical and morphological diversity of diagenetic fabrics in the study area indicate a complex set of paleohydrologic and diagenetic reaction events. Here, we explore possible formation mechanisms for these fabrics and textures, including early formation in either evaporite horizons or efflorescence from near-surface brines, or later formation due to precipitation from briny groundwater.

6.1 Hypothesis 1: Evaporitic surface crusts & efflorescence

We first consider if nodule formation was dominantly the result of evaporitic concentration within shallow pools and near surface efflorescence to form salt-enriched sediments, perhaps associated with periods of wetting and drying. Such a process was first described in Gale crater by the Stein et al. (2018) analysis of desiccation cracks in the Old Soaker outcrop of the Murray formation. However, in that instance no associated enrichment of salt was

observed, demonstrating that not all dry environments on Mars became briny environments. The raised polygonal ridges described in Section 4.5 have been interpreted to be similar evidence of desiccation features by Rapin et al. (2023). However, the raised ridges bounding the polygons are morphologically consistent with the larger, amalgamated nodules across this entire area, and particularly similar to the other regularly spaced nodule patterns that are not necessarily indicative of desiccation processes (e.g., Figure 3*e*). The nodular texture of the fracture infill could indicate that deeply buried desiccation cracks created a zone of higher porosity and permeability that locally increased brine accumulation and subsequent nodule cementation. Therefore, these polygons could represent small, isolated pools with wetting and drying processes, but do not explain the breadth of diagenetic textures observed in this area, which also include isolated nodules and nodules grouped in linear formations and chevron patterns; here, we explore the spectrum of possible formation mechanisms that could complement the desiccation crack interpretation. It is perhaps likely that all of these organized textures—the polygons, the chevroned ridges, etc.—could reflect nucleation and reaction processes similar to Liesegang banding (Ortoleva, 1993) or diagenetic roll front mineralization (e.g., Granger and Warren, 1969), but precipitating sulfate cements. Nucleation and chemical precipitation on Earth may be biologically mediated, if not the direct replacement of bioclasts or encasing bioclasts (e.g., phosphate nodules in the Tégulines Clay, Lerouge et al., 2018). However, numerical and experimental models show that the complex patterns created by redox (and other) reactions can also be abiotic (e.g., Ortoleva, 1993) and with heterogeneity due to slight variations in pH or pore space permeability, it is not unreasonable for abiogenic nucleation on Mars to produce the patterns of nodules described here. Perhaps it is precisely because of the lack of microbial substrates to aid in nucleation that Mars produces the organized nodule patterns that may not have common terrestrial analogs.

Two different outcrops were also observed around Sol 3476 to have angular, square nodules reminiscent in shape of halite hopper crystals, which could be pseudomorphs preserving evidence for primary or early diagenetic evaporites. However, these angular nodules are not confined to individual bedding planes and are not concentrated as abundantly as they are

typically found in the terrestrial rock record (e.g., Gornitz and Schreiber, 1981). Should these be pseudomorphs after halite, we might expect to see NaCl enrichment in the surrounding rock; however, these outcrops do not correspond to the higher NaCl targets observed in the APXS dataset. It would then be required that another episode of later, fresher fluids leached out the salts.

These angular nodules are a unique morphology among the large database of nodules analyzed in this study area, and with the available data our characterization as hopper-like is suggestive but not definitive. Therefore, they are not representative of the nodule features as a whole, and the interpretation that they may be evidence of primary evaporites cannot be extrapolated.

We also consider the possibility that the nodules formed early via efflorescence from near-surface brines. Terrestrial occurrences of starkeyite are usually produced by efflorescence, so the detection of small amounts of crystalline starkeyite in the Canaima drill sample (Chipera et al., 2023) is the best indicator of this process of formation in near-surface layers during gradual drying. This is similar to the presence of starkeyite in Mesozoic sandstones along the Rio Puerco, NM (Szynkiewicz et al., 2014). However, terrestrial examples of efflorescence form crusts on the surface, rather than nodular horizons (and the nodules cataloged in this study are not confined to single beds but rather are distributed throughout the outcrops where they are observed). These crusts should produce draping layers over salt crusts or disruption to primary stratification, neither of which have been observed in the study area. Further, there are no sedimentary breccias or fracture networks reflecting surface layers collapsed over dissolved crust (e.g., Friedman, 1997). We would also expect to see accompanying features reflecting cyclical wetting and drying, like teepee structures, desiccation cracks, or prism cracks (Allen, 1987; Assereto and Kendall, 1977), none of which are observed in the Canaima vicinity. The sediments of Gale crater, including the dune/interdune strata of the Mirador formation (Edgar et al., 2024), formed under long-term aggradational conditions; if primary, bedded evaporites formed and then eroded away, we would still expect to see evidence of their disruption to primary bedding or subsequent

deposition (we do not). It is possible that there were lower evaporation rates on Mars—about 1 mm/yr modeled by Andrews-Hannah & Lewis (2011) as compared to 0.1 mm/day in the Chilean Altiplano (Johnson et al., 2010)—which could maintain an evaporating water table at a greater depth than on Earth, and the additional overburden pressure of a few meters of accumulating sediment would prevent these signature evaporitic sedimentary structures from forming. As there is no evidence to support the formation of salt crusts it seems that another process may be required to explain the presence of the Starkeyite.

6.2 Hypothesis 2: Top-down dense brines from younger or remobilized sulfates

In all observed nodular outcrops, the nodules cross-cut bedding planes and are found distributed throughout the rock. There are no examples of primary laminae truncated against nodules, bending under them, or draping on top of them. However, there are a small number of nodules with lamination preserved inside the nodule, indicating formation at a later time, postdating compaction (e.g., Meyer et al., 2024, white arrows in Figure 9A and 9I). Given the smaller value of g on Mars compaction would have taken place at greater depths in the crust of Mars as compared to Earth (Grotzinger et al., 2015) suggesting a deeper level for subsurface formation.

Late-stage concretions are abundant on Earth, and the iron oxide Moqui marbles eroding out of Jurassic Navajo sandstones serve as analogs for the spherical hematite-cemented "blueberries" discovered in Meridiani Planum (e.g., Chan et al., 2000; Chan et al., 2004). While these redox-driven concretions are not compositional analogs to the nodules in this study, they do provide good examples of late-stage fluid movement through porous rock, a process which was invoked by Sun et al. (2019) in their analysis of diagenetic concretions from lower in the Gale crater stratigraphy. It seems that late-stage concretion formation may be common on Mars, perhaps more so than early diagenetic concretions for which compelling analogs do not currently exist at any rover landing site.

Indeed, the concretions described here are nodules dominated by magnesium sulfate, not iron oxides. This complicates their understanding as late-stage diagenetic features formed during

deeper burial. On Earth, magnesium sulfate concretions formed at depth are not observed, but secondary calcium sulfate precipitates are (Warren, 2016). Indiana carbonate sequences described by Maliva (1987) provide evidence that as dense brines sink, dolomitization releases Ca ions to form secondary anhydrite at depths of 30-40 meters, and Machel (2013) found that more than 90% of anhydrite found in deeply buried (<1km) Devonian carbonates of the Alberta Basin, Canada are replacive and may even postdate dolomitization. Deep brines can also be remobilized by groundwater fluids and reprecipitated in laterally adjacent strata; Rivera & Calderhead (2022) model groundwater migration in the Canadian Rockies, with deep (~1-2km) brines transported hundreds of kilometers laterally towards the basin margin. Therefore, there is terrestrial precedent for the movement and precipitation of secondary, non-"evaporite" sulfates at depth.

In one scenario, we propose a "top-down" hypothesis in which bedded evaporites deposited in stratigraphically higher units would have formed dense brines that would penetrate strata at lower elevations in the basin via gravitational drive. In particular, the evaporite source for those dense brines would be represented by the "boxwork" Mg sulfates—possibly evaporites—that occur at ~ -3500m (Siebach and Grotzinger, 2014), though the "boxwork" composition cannot be known with certainty until the rover reaches the region (Figure 11a). Salinity increases during periods of drying to form the boxwork (or other, yet-unknown sulfate sources) could have produced dense brines that would have become gravitationally unstable, seeping downward through the underlying stratigraphy and precipitating in patches as concretions and cements within the study area. The distribution of nodules across the lower stratigraphy would then relate directly to permeability gradients across the mudstones and sandstones. An overall decrease in grain size moving downwards through the section from Canaima to Mary Anning, with a marked shift from sandstone to mudstone occurring within the Pontours member, is consistent with the greater concentration and diversity of nodules at these stratigraphic levels. Meyer et al. (2024) propose that a basal Mirador formation unconformity could provide the rapid grain size change and pathways needed to produce the observed zone of intense nodular overprinting in the Pontours member, with fluids concentrated in this member due to clay in the underlying stratigraphy. Indeed, the

higher clay content present in the Carolyn Shoemaker formation (Glen Torridon region) below our study area, which decreases at Mont Mercou and disappears in the upper parts of stratigraphy (except, perhaps, in in the form of Mg-Fe phyllosilicates in the nodules), could have formed an aquitard at the base of this section. Our results complement the Meyer et al. (2024) ChemCam-based nodule analysis, and we further suggest the diversity and abundance of diagenetic textures concentrated just below Mont Mercou captured in the MAHLI dataset are consistent with the porosity and permeability gradients in the stratigraphy. In this scenario the Mg sulfates in the Mirador formation at -4000m would be roughly the same age as the putative "boxwork" sulfates at -3500m since they derive from a fluid source that was generated during deposition of the Mt. Sharp group. This timing of diagenesis could also contribute to the abundance of x-ray amorphous material throughout the not-yet lithified Murray formation via destabilization of clay minerals by silica-poor brines, and is consistent with the "top down" model presented in both Bristow et al. (2021) and Meyer et al. (2024).

A variant on this scenario, also involving gravitational drive, is that the "boxwork" or other higher Mg sulfates could have been remobilized by post-Mt. Sharp group fluids, perhaps associated with incision of Gediz Vallis, to penetrate through older rocks via fracture and matrix porosity. Hurowitz et al., (2017) propose that the layered "boxwork" sulfates (~ -3500m) observed at higher elevations in Mt. Sharp group strata could have been remobilized during younger fluid flow, with gravity-driven penetration of dense brines to precipitate in topographically lower but stratigraphically younger rocks of the Stimson formation. In this scenario the Mg sulfates in the Mirador formation would be much younger than the Mt. Sharp group "boxwork" Mg sulfates. This age difference could be on the order of ~ billion years as Martin et al. (2021) showed by dating jarosite in the Mt. Sharp group that was markedly younger than the age of the Mt. Sharp group strata (Murray formation) that hosts these sulfate minerals.

6.3 Hypothesis 3: Bottom-up precipitation from deep groundwater brines

A third distinct hypothesis would involve remobilization of salts buried in the crater at a depth below Curiosity's landing elevation (Figure 11b). The depth of the infill beneath the

rover could reach 1.5 km based on estimates of the crater impact topography (Grotzinger et al., 2015) and it is possible that early fill included evaporites as well as detrital sediments derived from the crater wall and central peak. These brines could have formed in situ, or been transported laterally, perhaps several hundreds of kilometers, from the large recharge area to the south of Gale crater, which serves as a regional low point (e.g., Andrews-Hanna et al., 2012; Zolotov and Mironenko, 2016). The presence of these deep brines could indicate regional or even global fluctuations in early Mars climate history, to first emplace and then later circulate the sulfate. The strong hydraulic gradient coming down from the crater rim, where meteoric waters enter the crater, and the weaker gradient coming from the taller but spatially restricted central peak, would meet and mix in the subsurface. Residual heat generated from the crater-forming impact or the ambient geothermal gradient could have provided the necessary heat input to drive the mixed fluids upwards through the stratigraphy; Schwenzer et al. (2012) demonstrate that an impact-driven hydrothermal system could have persisted in the bottom of Gale crater for several hundred thousand years, and the geothermal gradient could contribute to fluid movement for the millions of years timescales of Mount Sharp deposition. The resulting upwelling of groundwater through a buried evaporite deposit would dissolve Mg sulfate and carry the ions upwards in solution due to thermal buoyancy. Mg sulfate solubility increases with temperature, and even the slight decrease in temperature from a mostly-cooled hydrothermal system to colder strata above would decrease the solubility of Mg sulfate (Krumgalz, 2018). The decrease in pressure ascending through several km of vertical strata (perhaps on the order of ~50 bar/km) would also contribute to reduced solubility, though to a lesser degree than temperature, following well-studied solubility-pressure relationships in Ca sulfates on Earth (e.g., Blount and Dickson, 1973). Gradual evaporation of near-surface water would slowly increase the concentration of Mg sulfate until a threshold is reached and precipitation is triggered by the changing physical-chemical conditions; in a deeper groundwater scenario where a fluid was supersaturated at depth and cooled as it rose, pore spaces could serve as nucleation points for rapid crystallization. Slight local variations in porosity and permeability of the sediments could result in a heterogeneous distribution of Mg sulfate cements, as reflected in the spatial heterogeneity of nodules documented in this study. This model would require the movement

of deep waters through low-porosity, impermeable layers, such as Glen Torridon, but the heavily fractured outcrops observed in Glen Torridon could be evidence of fracture-conduits allowing the upward passage of Mg-rich fluids. These proposed mechanisms incorporate elements of processes observed on Earth, but the terrestrial record lacks a direct analog; the Martian stratigraphic history may record a unique process in large-scale Mg sulfate remobilization and sedimentation.

6.4 Hypothesis 4: Top-down precipitation due to desiccation of Mars

A final hypothesis centers around the well-established observation that Mars has lost a lot of its atmosphere and water to space (e.g., Jakosky and Phillips, 2001). This process was well underway by the time that Gale crater began to fill with sediments (Mahaffy et al., 2015). The inevitable consequence is that surface water would evaporate and after that groundwater would evaporate. In that latter case, evaporation would be controlled by the aridity of the atmosphere and the permeability (diffusivity) of the sediments (or fractured bedrock). As time passed, the groundwater would diffuse through the sediments and into the atmosphere, the water table would be lowered, and any soluble salts would be concentrated to the point where they might precipitate as pore-filling cements (Figure 11c).

In a sedimentary basin like Gale crater the groundwater would equilibrate with buried sediments so that solute composition would reflect sediment composition. Given the overwhelming concentration of basaltic sediments, it would be natural to expect these fluids to record that composition; elements such as magnesium and sulfur would be readily available, along with a host of other salts that could be concentrated to the point of precipitation (Tosca et al., 2005). Therefore, the observation of Mg sulfates in the strata of the Mirador formation could record this long-term desiccation of Mars.

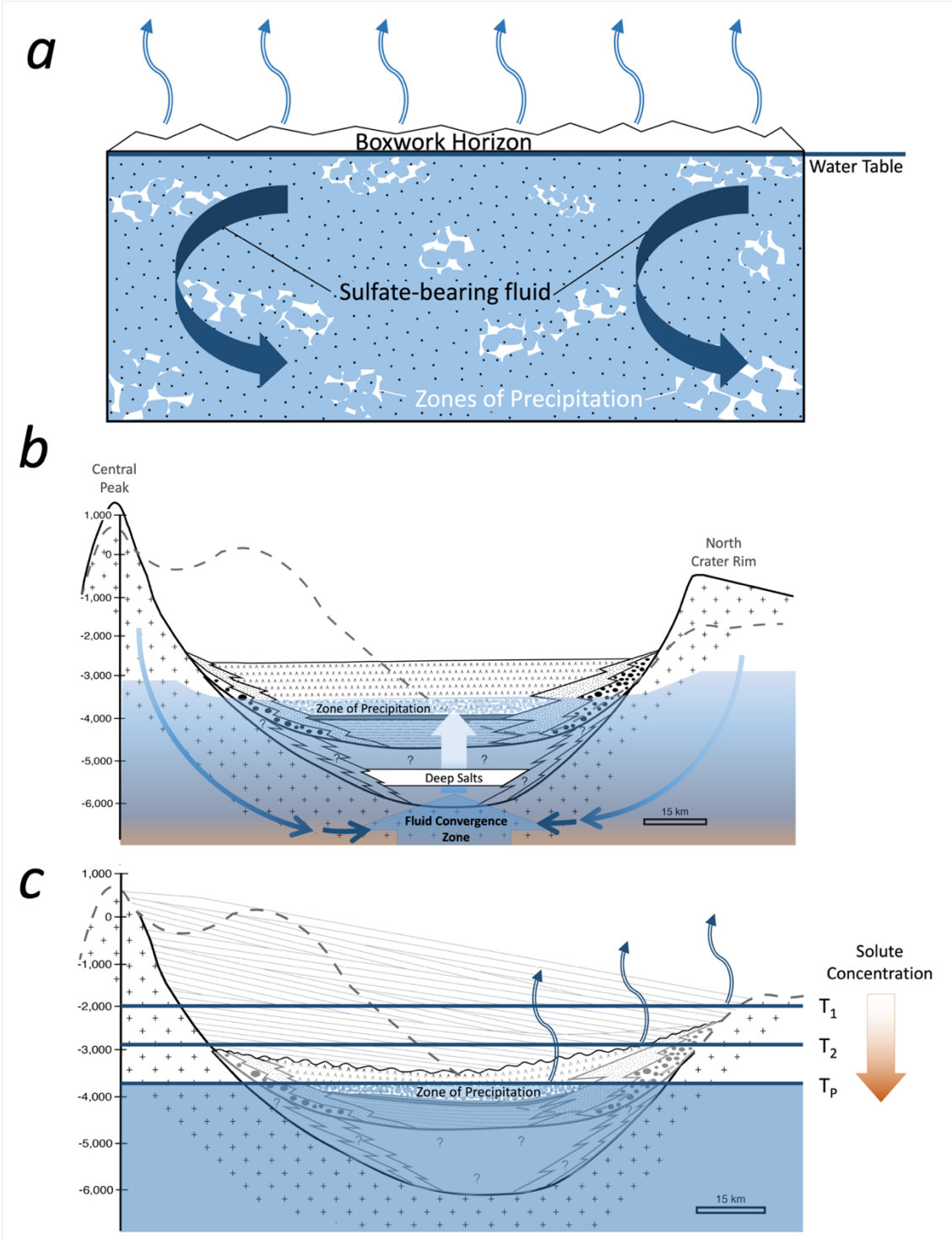

Figure 11. Schematic illustration of hypothesized processes for Mg sulfate precipitation in nodular bedrock, modified from Grotzinger et al. (2015) Figure 8. (a) Hypothesis 2: Top-down fluid migration and diagenesis. Fluids originate as evaporative brines, here represented as boxwork formation at -3500m MOLA elevation (though they could come

from other yet-unknown evaporite sources). These fluids are dense and descend via gravitational drive into the subsurface to the stratigraphic level of the Mirador formation (-4000m MOLA elevation) circulating and precipitating in the pore spaces within local patches above less permeable clay-bearing and finer-grained Glen Torridon sediments. This schematic represents one phase of a process that may have occurred several times as the groundwater system varied with sedimentation and aridity. (b) Hypothesis 3: Bottom-up fluid migration and diagenesis. Meteoric precipitation above crater highlands infiltrates and is driven gravitationally to substantial depths in the buried crater sediments. This groundwater mixes with warmer fluids originating at depth as connate or hydrothermal fluids, and rises up due to thermal warming, encountering sulfate evaporites from an early time in Gale's infilling. These remobilized sulfates may be leached to create brines that precipitate out at the top of the groundwater table to form patches of Mg-sulfate bearing strata in the Mirador formation. (c) Hypothesis 4: As Mars steadily desiccates due to loss of the atmosphere, connate fluids in equilibrium with basaltic sediments evaporate in the subsurface. These fluids draw down to progressively greater depths and steadily increase their salt content to a level where Mg-sulfate precipitates in pore space.

7 Conclusions

There is a wide range of diversity and abundance in the expression of the diagenetic textures that have been observed along Curiosity's traverse to date, but they exhibit particularly diagnostic behavior throughout the clay-sulfate transition region. By cataloging all diagenetic textures observed in MAHLI images, including their abundances, morphologies and relationships to each other, we find that changing abundance and diversity of textures parallels changes in stratigraphy, reflecting underlying fluid pathways. By analyzing cross-cutting relationships between the different feature types, we suggest a paragenetic sequence in which there are multiple phases of diagenetic fluid flow: at least two events are required to form co-occurring color variations, pits, and nodules, and to differentiate co-occurring populations of small and large, clustered nodules; two additional later stage events precipitated Ca sulfate veins, first in low-angle fractures nearly parallel to bedding, and later in high angle fractures (consistent with other examples of late-stage fracture-filling veins previously identified in the rover mission).

The Pontours member records strong overprinting diagenesis followed by an upward transition to pockets of nodules coincident with the transition between a fluvial-lacustrine to

an aeolian depositional environment. Porosity and permeability differences controlled by aeolian sediment sorting processes may have focused subsurface flow along these better sorted sediments; perhaps the underlying sediments were less permeable due to their higher clay content, forcing fluids to migrate preferentially within the parts of the aquifer marked by the basal aeolian sediments of the Mirador formation. The phyllosilicate-rich sediments of the underlying Glen Torridon region may therefore have acted as an aquiclude, resulting in a twofold representation in the diagenetic record: the diversity of textures is extremely high within the laminated mudstones of the upper Glasgow member, perhaps due to increased circulation aided by interspersed coarser grained fluvial barforms like Mont Mercou just above the less permeable clay-rich lower Glasgow member, and the destruction of primary stratigraphy throughout the Pontours member, which may therefore be a zone of high porosity and permeability like the sandstones overlying it. The distinct outcrop-scale patterns (linear, polygonal, and chevroned ridges) formed by diagenetic nodules in the Pontours member may also reflect the movement of reaction fronts through the subsurface within the parts of the aquifer with higher hydraulic conductivity.

Correlating the quantitative abundance of nodules with subtle variations in APXS bulk rock chemistry—that is, densely nodular targets in the upper Contigo member correlate with MgO and SO3 enrichments and CaO reduction—expands previous observations of Mg and Fe sulfate enrichment in individual nodules as well as bedrock, particularly in the upper part of the stratigraphic section. The apparent upward increase in nodule and cement contribution to bulk rock elemental composition through the section supports the hypothesis that these Mg sulfates were formed from small amounts of groundwater either dissolving salts in an overlying sulfate unit and transporting them downwards in dense brines, or upwelling through deeply buried salts below. Though there is some evidence for localized evaporite features, the lack of salt crystals, clear pseudomorphs, or disruption to primary lamination from draping or drying structures anywhere in the study region the requires alternative precipitation mechanisms, such as the movement of Mg sulfate from an over- or underlying unit, to explain the presence of these sulfates in the stratigraphy. The proposed hypotheses have implications for global Mars climate, with the bottom-up model allowing for more

longstanding circulation of recharged groundwater and the top-down models relating to the terminal aridification of Mars.

Overall, morphology, and diversity of diagenetic overprints in this key stratigraphic section of Gale crater, as lacustrine sediments give way to aeolian and surface water begins to dry, record at least four distinct episodes of diagenetic alteration. The distribution of these textures reflects the ease of fluid circulation through sediments overlying the less permeable clay-rich Glen Torridon region, and the Mg sulfate rich composition of nodules in the upper portions of the stratigraphic section record the late-stage movement of dense brines saturated with Mg sulfate sourced from elsewhere in the stratigraphy.

Acknowledgments

We would like to thank the scientists and engineers of the MSL team, especially the Mastcam, MAHLI, and APXS payload uplink and downlink leads, for their work in obtaining the observations necessary for this study and diligent contributions towards mission success.

Data Availability Statement

Data presented in this work are archived and freely available to the public in the NASA Planetary Data System (PDS): all APXS data (Berger, 2024; Gellert, 2013), Mastcam images (Malin, 2013), and MAHLI images (Edgett, 2013a, 2013b) used in this work are available in the PDS Geoscience Node and PDS Imaging Node. A list of all MAHLI observations used in this study with their accompanying characterization (presence/absence of all diagenetic textures as well as nodule classification) is available at the CaltechDATA site (Seeger & Grotzinger, 2024).

References

Allen, J. R. L. (1987). Desiccation of mud in the temperate intertidal zone: studies from the Severn Estuary and eastern England. *Philosophical Transactions of the Royal Society of London. B, Biological Sciences*, 315(1171), 127-156. https://doi.org/10.1098/rstb.1987.0005

Anderson, R., & Bell III, J. F. (2010). Geologic mapping and characterization of Gale Crater and implications for its potential as a Mars Science Laboratory landing site. *Mars J*. 5, 76–128.

Andrews-Hanna, J. C., & Lewis, K. W. (2011). Early Mars hydrology: 2. Hydrological evolution in the Noachian and Hesperian epochs. *Journal of Geophysical Research: Planets*, *116*(E2). https://doi.org/10.1029/2010JE003709

Andrews-Hanna, J. C., Soto, A., & Richardson, M. I. (2012). The hydrologic and climatic context of the Gale crater sedimentary mound. *Third Conference on Early Mars: Hydrologic, and Climatic Evolution and the Implications for Life*, *1680*, 7038.

Assereto, R., & Kendall, C. (1977). Nature, origin and classification of peritidal tepee structures and related breccias. *Sedimentology*, *24*(2), 153-210. https://doi.org/10.1111/j.1365-3091.1977.tb00254.x

Beitler, B., Chan, M. A., & Parry, W. T. (2003). Bleaching of Jurassic Navajo Sandstone on Colorado Plateau Laramide highs: Evidence of exhumed hydrocarbon supergiants? *Geology*, 31(12), 1041-1044. https://doi.org/10.1130/G19794.1

Beitler, B., Parry, W. T., & Chan, M. A. (2005). Fingerprints of fluid flow: chemical diagenetic history of the Jurassic Navajo Sandstone, southern Utah, USA. *Journal of Sedimentary Research*, 75(4), 547-561. https://doi.org/10.2110/jsr.2005.045

Bell III, J. F., Godber, A., McNair, S., Caplinger, M. A., Maki, J. N., Lemmon, M. T., ... & Deen, R. G. (2017). The Mars Science Laboratory Curiosity rover Mastcam instruments: Preflight and in-flight calibration, validation, and data archiving. *Earth and Space Science*, *4*(7), 396-452. https://doi.org/10.1002/2016EA000219

Berger, J. A., Gellert, R., McCraig, M. A., O'Connell-Cooper, C. D., Spray, J. G., Thompson, L. M., ... & Clark, J. V. (2023). Isochemical Characteristics of the Clay-Sulfate Transition in Gale Crater, Mars: APXS Results From Mont Mercou to the Marker Band Valley. In *Paper presented at the 54th lunar and planetary science conference (LPSC)*. Retrieved from https://www.hou.usra.edu/meetings/lpsc2023/pdf/1662.pdf

Blake, D., Vaniman, D., Achilles, C., Anderson, R., Bish, D., Bristow, T., ... & Yen, A. (2012). Characterization and calibration of the CheMin mineralogical instrument on Mars Science Laboratory. *Space Science Reviews*, *170*, 341-399. https://doi.org/10.1007/s11214-012-9905-1

Blount, C. W., & Dickson, F. W. (1973). Gypsum-anhydrite equilibria in systems CaSO4-H2O and CaCO4-NaCl-H2O. *American Mineralogist: Journal of Earth and Planetary Materials*, *58*(3-4_Part_1), 323-331.

Bowen, B., Martini, B.A., Chan, M.A., Parry, W.T., 2007. Reflectance spectroscopic mapping of diagenetic heterogeneities and fluid-flow pathways in the Jurassic Navajo Sandstone. *AAPG Bulletin,* 91, 173–190. DOI:10.1306/08220605175

Campbell, J. L., Perrett, G. M., Gellert, R., Andrushenko, S. M., Boyd, N. I., Maxwell, J. A., … Schofield, C. D. M. (2012). Calibration of the Mars Science Laboratory Alpha Particle X-ray Spectrometer. *Space Science Reviews*, 170(1), 319–340. https://doi.org/10.1007/s11214-012-9873-5

Caravaca, G., Mangold, N., Dehouck, E., Schieber, J., Zaugg, L., Bryk, A. B., ... & Lanza, N. L. (2022). From lake to river: Documenting an environmental transition across the Jura/Knockfarril Hill members boundary in the Glen Torridon region of Gale crater (Mars). *Journal of Geophysical Research: Planets*, 127(9), e2021JE007093. https://doi.org/10.1029/2021JE007093

Cardenas, B. T., Grotzinger, J. P., Lamb, M. P., Lewis, K. W., Fedo, C. M., Bryk, A. B., ... & Caravaca, G. (2022a). Barform deposits of the Carolyn Shoemaker formation, Gale crater, Mars. *Journal of Sedimentary Research*, *92*(12), 1071-1092. https://doi.org/10.2110/jsr.2022.032

Cardenas, B. T., Lamb, M. P., & Grotzinger, J. P. (2022b). Martian landscapes of fluvial ridges carved from ancient sedimentary basin fill. *Nature Geoscience*, 15(11), 871-877. https://doi.org/10.1038/s41561-022-01058-2

Caswell, T. E., & Milliken, R. E. (2017). Evidence for hydraulic fracturing at Gale crater, Mars: Implications for burial depth of the Yellowknife Bay formation. *Earth and Planetary Science Letters*, 468, 72-84. https://doi.org/10.1016/j.epsl.2017.03.033

Chan, M. A., Beitler, B., Parry, W. T., Ormö, J., & Komatsu, G. (2004). A possible terrestrial analogue for haematite concretions on Mars. *Nature*, 429(6993), 731-734. https://doi.org/10.1038/nature02600

Chan, M. A., Bowen, B. B., Parry, W., Ormö, J., & Komatsu, G. (2005). Red rock and red planet diagenesis. *GSA Today*, *15*, 4-10.

Chan, M. A., Parry, W. T., & Bowman, J. R. (2000). Diagenetic hematite and manganese oxides and fault-related fluid flow in Jurassic sandstones, southeastern Utah. *AAPG Bulletin*, 84(9), 1281-1310. https://doi.org/10.1306/A9673E82-1738-11D7-8645000102C1865D

Chipera, S. J., Vaniman, D. T., Rampe, E. B., Bristow, T. F., Martínez, G., Tu, V. M., ... & Grotzinger, J. P. (2023). Mineralogical investigation of Mg-Sulfate at the Canaima drill site, Gale crater, Mars. *Journal of Geophysical Research: Planets*, *128*(11), e2023JE008041. https://doi.org/10.1029/2023JE008041

Clark, J. V., Sutter, B., Lewis, J., Mcadam, A. C., Archer, P. D., Franz, H., ... & Ming, D. W. (2023, March). Mineralogical and chemical changes in the clay-sulfate transition region as detected by the Sample Analysis at Mars-Evolved Gas Analyzer (SAM-EGA) in Gale crater, Mars. In *54th Lunar and Planetary Science Conference*.

Downs, R. T., & MSL Science Team. (2015). Determining mineralogy on Mars with the CheMin X-ray diffractometer. *Elements*, *11*(1), 45-50. https://doi.org/10.2113/gselements.11.1.45

Edgar, L., Grotzinger, J., Fedo, C. M., Meyer, M., Rapin, W., Dietrich, W. E., ... & Fraeman, A. (2024, March). Wet to dry depositional environments recorded in the clay-sulfate transition region in Gale crater, Mars: Overview and stratigraphic context for Curiosity's exploration campaign. In *55th Lunar and Planetary Science Conference* (p. 1016).

Edgett, K. S. (2013a). MSL MARS HAND LENS IMAGER 2 EDR IMAGE V1.0 [Data set]. NASA Planetary Data System. https://doi.org/10.17189/1520187

Edgett, K. S. (2013b). MSL MARS HAND LENS IMAGER 2 EDR ZSTACK V1.0 [Data set]. NASA Planetary Data System. https://doi.org/10.17189/1520396

Edgett, K. S., Yingst, R. A., Ravine, M. A., Caplinger, M. A., Maki, J. N., Ghaemi, F. T., ... & Goetz, W. (2012). Curiosity's Mars hand lens imager (MAHLI) investigation. *Space Science Reviews*, *170*, 259-317.

Fedo, C. M., Bryk, A. B., Edgar, L. A., Bennett, K. A., Fox, V. K., Dietrich, W. E., ... & Sutter, B. (2022). Geology and stratigraphic correlation of the Murray and Carolyn Shoemaker formations across the Glen Torridon region, Gale crater, Mars. *Journal of Geophysical Research: Planets*, *127*(9), e2022JE007408. https://doi.org/10.1029/2022JE007408

Fraeman, A. A., Arvidson, R. E., Catalano, J. G., Grotzinger, J. P., Morris, R. V., Murchie, S. L., ... & Viviano, C. E. (2013). A hematite-bearing layer in Gale Crater, Mars: Mapping and implications for past aqueous conditions. *Geology*, *41*(10), 1103-1106. https://doi.org/10.1130/G34613.1

Fraeman, A. A., Edgar, L. A., Rampe, E. B., Thompson, L. M., Frydenvang, J., Fedo, C. M., ... & Wong, G. M. (2020). Evidence for a diagenetic origin of Vera Rubin ridge, Gale crater, Mars: Summary and synthesis of Curiosity's exploration campaign. *Journal of Geophysical Research: Planets*, *125*(12), e2020JE006527. https://doi.org/10.1029/2020JE006527

Friedman, G. M. (1997). Dissolution-collapse breccias and paleokarst resulting from dissolution of evaporite rocks, especially sulfates. *Carbonates and Evaporites*, *12*, 53-63. https://doi.org/10.1007/BF03175802

Frydenvang, J., Gasda, P. J., Hurowitz, J. A., Grotzinger, J. P., Wiens, R. C., Newsom, H. E., ... & Vasavada, A. R. (2017). Diagenetic silica enrichment and late-stage groundwater activity in Gale crater, Mars. *Geophysical Research Letters*, *44*(10), 4716-4724. https://doi.org/10.1002/ 2017GL073323.

Gasda, P. J., Comellas, J., Essunfeld, A., Das, D., Bryk, A. B., Dehouck, E., ... & Reyes-Newell, A. (2022). Overview of the morphology and chemistry of diagenetic features in the clay-rich Glen Torridon unit of Gale crater, Mars. *Journal of Geophysical Research: Planets*, *127*(12), e2021JE007097. https://doi.org/10.1029/2021JE007097

Gellert, R. (2013). MSL Mars alpha particle X-ray spectrometer 4/5 RDR V1.0. [Dataset] *NASA Planetary Data System*. https://doi.org/10.17189/1518757

Gornitz, V. M., & Schreiber, B. C. (1981). Displacive halite hoppers from the Dead Sea; some implications for ancient evaporite deposits. *Journal of Sedimentary Research*, *51*(3), 787-794. https://doi.org/10.1306/212F7DAB-2B24-11D7-8648000102C1865D

Granger, H. C., & Warren, C. G. (1969). Unstable sulfur compounds and the origin of roll-type uranium deposits. *Economic Geology*, *64*(2), 160-171. https://doi.org/10.2113/gsecongeo.64.2.160

Grotzinger, J. P., Arvidson, R. E., Bell Iii, J. F., Calvin, W., Clark, B. C., Fike, D. A., ... & Watters, W. A. (2005). Stratigraphy and sedimentology of a dry to wet eolian depositional system, Burns formation, Meridiani Planum, Mars. *Earth and Planetary Science Letters*, *240*(1), 11-72. https://doi.org/10.1016/j.epsl.2005.09.039

Grotzinger, J. P., Sumner, D. Y., Kah, L. C., Stack, K., Gupta, S., Edgar, L., et al. (2014). A habitable fluvio-lacustrine environment at Yellowknife Bay, Gale crater, Mars. *Science*, *343*(6169), 1242777. https://doi.org/10.1126/science.1242777

Grotzinger, J. P., Gupta, S., Malin, M. C., Rubin, D. M., Schieber, J., Siebach, K., ... & Wilson, S. A. (2015). Deposition, exhumation, and paleoclimate of an ancient lake deposit, Gale crater, Mars. *Science*, *350*(6257), aac7575. https://doi.org/10.1126/science.aac7575

Hurowitz, J. A., Grotzinger, J. P., Fischer, W. W., McLennan, S. M., Milliken, R. E., Stein, N., ... & Wiens, R. C. (2017). Redox stratification of an ancient lake in Gale crater, Mars. *Science*, *356*(6341), eaah6849. DOI: 10.1126/science.aah6849

Inagaki, F., Hinrichs, K. U., Kubo, Y., Bowles, M. W., Heuer, V. B., Hong, W. L., ... & Yamada, Y. (2015). Exploring deep microbial life in coal-bearing sediment down to~ 2.5 km below the ocean floor. *Science*, *349*(6246), 420-424.

Jakosky, B. M., & Phillips, R. J. (2001). Mars' volatile and climate history. *Nature*, *412*(6843), 237-244. https://doi.org/10.1038/35084184

Johnson, E., Yáñez, J., Ortiz, C., & Muñoz, J. (2010). Evaporation from shallow groundwater in closed basins in the Chilean Altiplano. *Hydrological Sciences Journal–Journal des Sciences Hydrologiques*, *55*(4), 624-635. https://doi.org/10.1080/02626661003780458

Kah, L. C., Stack, K. M., Eigenbrode, J. L., Yingst, R. A., & Edgett, K. S. (2018). Syndepositional precipitation of calcium sulfate in Gale Crater, Mars. *Terra Nova*, *30*(6), 431-439. https:// doi.org/10.1111/ter.12359.

Knoll, A. H., & Grotzinger, J. (2006). Water on Mars and the prospect of Martian life. *Elements*, 2(3), 169-173. https://doi.org/10.2113/gselements.2.3.169

Kronyak, R. E., Kah, L. C., Edgett, K. S., VanBommel, S. J., Thompson, L. M., Wiens, R. C., ... & Nachon, M. (2019). Mineral-filled fractures as indicators of multigenerational fluid flow in the Pahrump Hills member of the Murray formation, Gale crater, Mars. *Earth and Space Science*, *6*(2), 238-265. https://doi.org/10.1029/2018EA000482

Krumgalz, B. S. (2018). Temperature dependence of mineral solubility in water. Part 3. Alkaline and alkaline earth sulfates. *Journal of Physical and Chemical Reference Data*, *47*(2).

Le Deit, L., Hauber, E., Fueten, F., Pondrelli, M., Rossi, A. P., & Jaumann, R. (2013). Sequence of infilling events in Gale Crater, Mars: Results from morphology, stratigraphy, and mineralogy. *Journal of Geophysical Research: Planets*, *118*(12), 2439-2473. https://doi.org/10.1002/2012JE004322

Lerouge, C., Robinet, J. C., Debure, M., Tournassat, C., Bouchet, A., Fernández, A. M., ... & Claret, F. (2018). A deep alteration and oxidation profile in a shallow clay aquitard: Example of the Tégulines Clay, East Paris Basin, France. *Geofluids*, *2018*, 1-20. https://doi.org/10.1155/2018/1606753

L'Haridon, J., Mangold, N., Meslin, P. Y., Johnson, J. R., Rapin, W., Forni, O., ... & Wiens, R. C. (2018). Chemical variability in mineralized veins observed by ChemCam on the lower slopes of Mount Sharp in Gale crater, Mars. *Icarus*, *311*, 69-86. https://doi.org/10.1016/j.icarus.2018.01.028

Léveillé, R. J., Bridges, J., Wiens, R. C., Mangold, N., Cousin, A., Lanza, N., ... & Newsom, H. (2014). Chemistry of fracture-filling raised ridges in Yellowknife Bay, Gale Crater: Window into past aqueous activity and habitability on Mars. *Journal of Geophysical Research: Planets*, *119*(11), 2398-2415. doi:10.1002/ 2014JE004620.

Magnabosco, C., Lin, L.-H., Dong, H., Bomberg, M., Ghiorse, W., Stan-Lotter, H., Pedersen, K., Kieft, T.L., van Heerden, E., and Onstott, T.C. (2018) The biomass and biodiversity of the continental subsurface. *Nature Geoscience,* 11:707–717. https://doi.org/10.1038/s41561-018-0221-6

Mahaffy, P. R., Webster, C. R., Stern, J. C., Brunner, A. E., Atreya, S. K., Conrad, P. G., ... & MSL Science Team. (2015). The imprint of atmospheric evolution in the D/H of Hesperian clay minerals on Mars. *Science*, *347*(6220), 412-414. DOI: 10.1126/science.1260291

Malin, M. C. (2013). MSL MARS MAST CAMERA 2 EDR IMAGE V1.0 [Data set] NASA Planetary Data System. https://doi.org/10.17189/1520190

Malin, M. C., & Edgett, K. S. (2000). Sedimentary rocks of early Mars. *Science*, *290*(5498), 1927-1937. DOI: 10.1126/science.290.5498.1927

Malin, M. C., Ravine, M. A., Caplinger, M. A., Tony Ghaemi, F., Schaffner, J. A., Maki, J. N., ... & Jensen, E. H. (2017). The Mars Science Laboratory (MSL) mast cameras and descent imager: Investigation and instrument descriptions. *Earth and Space Science*, *4*(8), 506-539. https://doi.org/10.1002/2016EA000252

Martin, P. E., Farley, K. A., Malespin, C. A., Mahaffy, P. R., Edgett, K. S., Gupta, S., ... & Vasconcelos, P. M. (2021). Billion-year exposure ages in Gale crater (Mars) indicate Mount Sharp formed before the Amazonian period. *Earth and Planetary Science Letters*, *554*, 116667. https://doi.org/10.1016/j.epsl.2020.116667

McLennan, S. M., Bell iii, J. F., Calvin, W. M., Christensen, P. R., Clark, B. D., De Souza, P. A., ... & Yen, A. (2005). Provenance and diagenesis of the evaporite-bearing Burns formation, Meridiani Planum, Mars. *Earth and Planetary Science Letters*, *240*(1), 95-121. https://doi.org/10.1016/j.epsl.2005.09.041

McLennan, S. M., Grotzinger, J. P., Hurowitz, J. A., & Tosca, N. J. (2019). The sedimentary cycle on early Mars. *Annual Review of Earth and Planetary Sciences*, *47*, 91-118. doi:10.1146/annurev-earth-053018-060332

Meyer, M. J., Milliken, R. E., Stack, K. M., Edgar, L.A., Rampe, E. B., Turner, M. L., et al. (2024). The Geological Context and Significance of the Clay-Sulfate Transition Region in Mount Sharp, Gale Crater, Mars: An Integrated Assessment Based on Orbiter and Rover Data. *GSA Bulletin, 137(1-2), 82-115.*

Milliken, R. E., Grotzinger, J. P., & Thomson, B. J. (2010). Paleoclimate of Mars as captured by the stratigraphic record in Gale Crater. *Geophysical Research Letters*, *37*(4). https://doi.org/10.1029/2009GL041870

Mondro, C. A., Grotzinger, J. P., Fedo, C. M., Paar, G. (2023). Fracture patterns in Mont Mercou record changing stress fields during burial and exhumation of Mount Sharp, Gale Crater, Mars. *Geological Society of America Abstracts with Programs*. Vol. 55, No. 6. doi: 10.1130/abs/2023AM-391634

Moser, D.P., Gihring, T., Fredrickson, J.K., Brockman, F.J., Balkwill, D., Dollhopf, M.E., Sherwood Lollar, B., Pratt, L.M., Boice, E., Southam, G., Wanger, G., Welty, A.T., Baker, B.J., and Onstott, T.C. (2005) Desulfotomaculum spp. and Methanobacterium spp. dominate 4–5 km deep fault. *Applied Environmental Microbiology,* 71:8773–8783. https://doi.org/10.1128/AEM.71.12.8773-8783.2005

Nachon, M., Clegg, S.M., Mangold, N., Schröder, S., Kah, L.C., Dromart, G., et al., 2014. Calcium sulfate veins characterized by ChemCam/Curiosity at Gale crater, Mars. *Journal of Geophysical. Research,* 119 (9), 1991–2016. https://doi.org/10.1002/2013JE004588.

Nachon, M., Mangold, N., Forni, O., Kah, L. C., Cousin, A., Wiens, R. C., ... & Sumner, D. (2017). Chemistry of diagenetic features analyzed by ChemCam at Pahrump Hills, Gale crater, Mars. *Icarus*, *281*, 121-136. https://doi.org/10.1016/j.icarus.2016.08.026

Onstott, T. C., Ehlmann, B. L., Sapers, H., Coleman, M., Ivarsson, M., Marlow, J. J., ... & Niles, P. (2019). Paleo-rock-hosted life on Earth and the search on Mars: a review and strategy for exploration. *Astrobiology*, *19*(10), 1230-1262. https://doi.org/10.1089/ast.2018.1960

Ortoleva, P. (1993). Geochemical self-organization. *Oxford Monographs on Geology and Geophysics*.

Parry, W. T., Chan, M. A., & Beitler, B. (2004). Chemical bleaching indicates episodes of fluid flow in deformation bands in sandstone. *AAPG bulletin*, *88*(2), 175-191. https://doi.org/10.1306/09090303034

Potter, S. L., Chan, M. A., Petersen, E. U., Dyar, M. D., & Sklute, E. (2011). Characterization of Navajo Sandstone concretions: Mars comparison and criteria for distinguishing diagenetic origins. *Earth and Planetary Science Letters*, *301*(3-4), 444-456. https://doi.org/10.1016/j.epsl.2010.11.027

Rampe, E. B., Bristow, T. F., Blake, D. F., Vaniman, D. T., Chipera, S. J., Downs, R. T., ... & Wilson, M. (2022, March). Mineralogical trends over the clay-sulfate transition in Gale Crater from the Mars Science Laboratory CheMin instrument. In *53rd Lunar and Planetary Science Conference*.

Rampe, E. B., Ming, D. W., Blake, D. F., Bristow, T. F., Chipera, S. J., Grotzinger, J. P., ... & Thompson, L. M. (2017). Mineralogy of an ancient lacustrine mudstone succession from the Murray formation, Gale crater, Mars. *Earth and Planetary Science Letters*, *471*, 172-185. https://doi.org/10.1016/j.epsl.2017.04.021

Rapin, W., Dromart, G., Clark, B. C., Schieber, J., Kite, E. S., Kah, L. C., ... & Lanza, N. L. (2023). Sustained wet–dry cycling on early Mars. *Nature*, 620(7973), 299-302. https://doi.org/10.1038/s41586-023-06220-3

Rivera-Hernández, F., Sumner, D. Y., Mangold, N., Banham, S. G., Edgett, K. S., Fedo, C. M., ... & Wiens, R. C. (2020). Grain size variations in the Murray formation: Stratigraphic evidence for changing depositional environments in Gale crater, Mars. *Journal of Geophysical Research: Planets*, *125*(2), e2019JE006230. https://doi.org/10.1029/2019JE006230

Schwenzer, S. P., Abramov, O., Allen, C. C., Bridges, J. C., Clifford, S. M., Filiberto, J., ... & Wittmann, A. (2012). Gale Crater: Formation and post-impact hydrous environments. *Planetary and Space Science*, *70*(1), 84-95.

Seeger, C., & Grotzinger, J. P. (2024). Diagenesis of the Clay-Sulfate Stratigraphic Transition, Mount Sharp Group, Gale Crater, Mars [Dataset]. CaltechDATA. https://doi.org/10.22002/krdbt-e4j31

Seiler, W.M., 2008. Jurassic Navajo Sandstone of Coyote Buttes, Utah/Arizona: Coloration and Diagenetic History, Preservation of a Dinosaur Trample Surface, and a Terrestrial Analog to Mars. *Doctoral dissertation, the University of Utah*.

Siebach, K. L., & Grotzinger, J. P. (2014). Volumetric estimates of ancient water on Mount Sharp based on boxwork deposits, Gale Crater, Mars. *Journal of Geophysical Research: Planets*, *119*(1), 189-198. https://doi.org/10.1002/2013JE004508

Siebach, K.L., Grotzinger, J.P., Kah, L.C., Stack, K.M., Malin, M., Léveillé, R., Sumner, D.Y., 2014. Subaqueous shrinkage cracks in the Sheepbed mudstone: implications for early fluid diagenesis, Gale crater, Mars. *Journal of Geophysical Research,* 119 (7), 1597–1613. https://doi.org/10.1002/2014JE004623.

Sheppard, R. Y., Milliken, R. E., Parente, M., & Itoh, Y. (2021). Updated perspectives and hypotheses on the mineralogy of lower Mt. Sharp, Mars, as seen from orbit. *Journal of Geophysical Research: Planets*, *126*(2), e2020JE006372. https://doi.org/10.1029/2020JE006372

Squyres, S. W., Grotzinger, J. P., Arvidson, R. E., Bell III, J. F., Calvin, W., Christensen, P. R., ... & Soderblom, L. A. (2004). In situ evidence for an ancient aqueous environment at Meridiani Planum, Mars. *Science*, *306*(5702), 1709-1714. DOI: 10.1126/science.1104559

Stack, K.M., Grotzinger, J.P., Kah, L.C., Schmidt, M.E., Mangold, N., Edgett, K.S., et al., 2014. Diagenetic origin of nodules in the Sheepbed member, Yellowknife Bay formation, Gale crater, Mars. *Journal of Geophysical Research,* 119 (7), 1637–1664. https://doi.org/10. 1002/2014JE004617.

Stein, N., Grotzinger, J. P., Schieber, J., Mangold, N., Hallet, B., Newsom, H., ... & Dehouck, E. (2018). Desiccation cracks provide evidence of lake drying on Mars, Sutton Island member, Murray formation, Gale Crater. *Geology*, *46*(6), 515-518. https://doi.org/10.1130/G40005.1

Summer, N. S., & Verosub, K. L. (1992). Diagenesis and organic maturation of sedimentary rocks under volcanic strata, Oregon. *AAPG Bulletin*, *76*(8), 1190-1199.

Sun, V. Z., Stack, K. M., Kah, L. C., Thompson, L., Fischer, W., Williams, A. J., ... & VanBommel, S. (2019). Late-stage diagenetic concretions in the Murray formation, Gale crater, Mars. *Icarus*, 321, 866-890. https://doi.org/10.1016/j.icarus.2018.12.030

Tice, M.M. and Lowe, D.R. (2004) Photosynthetic microbial mats in the 3,416-Myr-old ocean. *Nature* 431:549–552. https://doi.org/10.1038/nature02888

Thomson, B. J., Bridges, N. T., Milliken, R., Baldridge, A., Hook, S. J., Crowley, J. K., ... & Weitz, C. M. (2011). Constraints on the origin and evolution of the layered mound in Gale Crater, Mars using Mars Reconnaissance Orbiter data. *Icarus*, *214*(2), 413-432. https://doi.org/10.1016/j.icarus.2011.05.002

Tosca, N. J., A. H. Knoll, and S. M. McLennan (2008), Water activity and the challenge for life on early Mars, *Science*, 320(5880), 1204–1207. DOI: 10.1126/science.1155432

Tosca, N. J., McLennan, S. M., Clark, B. C., Grotzinger, J. P., Hurowitz, J. A., Knoll, A. H., ... & Squyres, S. W. (2005). Geochemical modeling of evaporation processes on Mars: Insight from the sedimentary record at Meridiani Planum. *Earth and Planetary Science Letters*, *240*(1), 122-148. https://doi.org/10.1016/j.epsl.2005.09.042

Treiman, A. H., Lanza, N. L., VanBommel, S., Berger, J., Wiens, R., Bristow, T., ... & Anderson, R. (2023). Manganese-Iron Phosphate Nodules at the Groken Site, Gale Crater, Mars. *Minerals*, *13*(9), 1122. https://doi.org/10.3390/min13091122

VanBommel, S. J., Berger, J. A., Gellert, R., O'Connell-Cooper, C. D., McCraig, M. A., Thompson, L. M., ... & Boyd, N. I. (2023). Elemental composition of manganese- and phosphorus-rich nodules in the Knockfarril Hill member, Gale crater, Mars. *Icarus*, *392*, 115372. https://doi.org/10.1016/j.icarus.2022.115372

VanBommel, S. J., Gellert, R., Berger, J. A., Campbell, J. L., Thompson, L. M., Edgett, K. S., et al. (2016). Deconvolution of distinct lithology chemistry through oversampling with the Mars Science Laboratory Alpha Particle X-Ray Spectrometer. *X-Ray Spectrometry*, 45(3), 155–161. https://doi.org/10.1002/xrs.2681

VanBommel, S. J., Gellert, R., Berger, J. A., Thompson, L. M., Edgett, K. S., McBride, M. J., et al. (2017). Modeling and mitigation of sample relief effects applied to chemistry measurements by the Mars Science Laboratory Alpha Particle X-ray Spectrometer. *X-Ray Spectrometry*, 46(4), 229–236. https://doi.org/10.1002/xrs.2755

Warren, J. K. (2016). *Evaporites: A geological compendium*. Springer.

Wiens, R. C., Maurice, S., Barraclough, B., Saccoccio, M., Barkley, W. C., Bell, J. F., III, et al. (2012). The ChemCam Instrument Suite on the Mars Science Laboratory (MSL) Rover: Body Unit and Combined System Tests. *Space Science Reviews*, 170(1–4), 167–227. https://doi.org/10.1007/s11214-012-9902-4

Wiens, R. C., Rubin, D. M., Goetz, W., Fairen, A. G., Schwenzer, S. P., Johnson, J. R., ... & Grotzinger, J. P. (2017). Centimeter to decimeter hollow concretions and voids in Gale Crater sediments, Mars. *Icarus*, *289*, 144-156. https://doi.org/10.1016/j.icarus.2017.02.003.

Williams, R. M., Grotzinger, J. P., Dietrich, W. E., Gupta, S., Sumner, D. Y., Wiens, R. C., ... & Fabre, C. (2013). Martian fluvial conglomerates at Gale crater. *Science*, *340*(6136), 1068-1072. DOI: 10.1126/science.1237317

Yen, A. S., Ming, D. W., Vaniman, D. T., Gellert, R., Blake, D. F., Morris, R. V., ... & MSL Science Team. (2017). Multiple stages of aqueous alteration along fractures in mudstone and sandstone strata in Gale Crater, Mars. *Earth and Planetary Science Letters*, *471*, 186-198. https://doi.org/10. 1016/j.epsl.2017.04.033.

Zolotov, M. Y., & Mironenko, M. V. (2016). Chemical models for Martian weathering profiles: Insights into formation of layered phyllosilicate and sulfate deposits. *Icarus*, *275*, 203-220. https://doi.org/10.1016/j.icarus.2016.04.011